Engineering and dynamical control of interfacial properties in ultra-thin films to tune magnetic spin textures

Titiksha Srivastava

Communauté UNIVERSITÉ Grenoble Alpes

THÈSE

Pour obtenir le grade de

DOCTEUR DE LA COMMUNAUTÉ UNIVERSITÉ GRENOBLE ALPES

Spécialité : Physique de la Matière Condensée et du Rayonnement

Arrêté ministériel : 25 mai 2016

Présentée par

Titiksha SRIVASTAVA

Thèse dirigée par **Claire BARADUC**, CEA
et codirigée par **Hélène BEA**, UGA
préparée au sein du **Laboratoire Spintronique et Technologie des Composants**
dans **l'École Doctorale Physique**

Ingénierie et contrôle dynamique des propriétés interfaciales dans les films ultra-minces pour ajuster les textures de spin magnétique

Engineering and dynamical control of interfacial properties in ultra-thin films to tune magnetic spin textures

Thèse soutenue publiquement le **29 janvier 2019**,
devant le jury composé de :

Monsieur ANDRE THIAVILLE
DIRECTEUR DE RECHERCHE, CNRS ILE-DE FRANCE GIF-SUR-YVETTE, Rapporteur
Monsieur JOO-VON KIM
CHARGE DE RECHERCHE, CNRS ILE-DE FRANCE GIF-SUR-YVETTE, Rapporteur
Monsieur DAFINE RAVELOSONA
DIRECTEUR DE RECHERCHE, CNRS ILE-DE FRANCE GIF-SUR-YVETTE, Président
Monsieur STEPHANE MANGIN
PROFESSEUR, UNIVERSITE DE LORRAINE, Examinateur
Madame CLAUDINE LACROIX
DIRECTRICE DE RECHERCHE EMERITE, CNRS DELEGATION ALPES, Examinateur

To my family

Acknowledgement

My PhD journey was filled with moments of joy, motivation, exasperation, excitement, panic, self-doubt, relief, contentment and so on and I have been very lucky to have had so many people around me that made each of these moments monumentally memorable.

I would start by thanking first and foremost my supervisors Hélène Béa and Claire Baraduc for being my pillars of strength. Thank you Hélène for being a constant support and answering my endless queries from the very moment I started my internship at Spintec until the end of the PhD. Your humbleness and optimism is inspiring. Thank you also for being such a warm hearted person and guiding me even through the difficult stages of the PhD. Thank you Claire for your invaluable remarks and guidance throughout this phase. I adore your organizational skills and clarity of thought. Thank you for motivating me at each and every crucial point of this PhD. I thoroughly enjoyed working with both of you.

I would now like to extend my sincere gratitude to André Thiaville, Joo-Von Kim, Dafiné Ravelosona, Stéphane Mangin and Claudine Lacroix for accepting to be members of the jury, their careful evaluation of the manuscript and their kind remarks about the thesis.

For my experiments, I have had a lot of help from many people. I would like to thank Stéphane Auffret for depositing the samples for me and also for his ever smiling 'Salut' every morning at Spintec, Laurent Villa, for the e-beam lithography and also for being such a cool scientist, Isabelle Joumard for helping me using NanoMOKE, PPMS, etc and practically every machine. I would also like to thank people from Insitute Néel: Marine Schott, Anne Bernand-Mantel, Stéphania Pizzini, Viola Krizakova, Jan Vogel and Laurent Ranno for their immense help with Kerr Microscopy and also the discussions and remarks related to the experiments I performed. A big thank you to Mohamed Belmeguenai and Yves Roussigné at LSPM, Université Paris 13, for helping with the Brillouin Light Spectroscopy measurements. Again from Spintec, I would like to thank Mairbek Chshiev for helping me understand a lot of fundamental concepts related to the subject of my PhD. I am also very grateful to Olivier Boulle, Gilles Gaudin, Mihai Miron, Bernard Dieny, Olivier Fruchart, Lucian Prejbeanu and Liliana Prejbeanu with whom I had scientific discussions time and again which helped me to both understand and direct the course of my experiments.

I also came across a wonderful bunch of fellow PhD students, post-docs and internship students at Spintec. The intensive conversations punctuated with jokes during lunch or 'soirées' were always so delightful. I start by thanking my officemates: Paulo Coelho, Mathieu Fabre and Jyotirmoy Chatterjee. I cannot imagine my life at Spintec without you guys. I will always cherish each and every discussion we had on scientific/nonscientific/absurd topics. I would like to thank Cécile, Dali and Jay with whom I embarked on this PhD endeavor. Professionally also to Dali and Jay for helping me with MOKE measurements. A big thank you also to Chandrajee for sharing his expertise on many subjects and for being an amazing person. Thank you Marco, Arnaud, Daniel, Willy, Caroline, Eva, Svetlana, Haozhe, Michael, Luis, Gaurav, Pankaj, Aurélien, Steven, Antoine, Pyunghwa, Raj, Safeer, Claire, Anike, Dai, Léa, Alex, Alexu, Lamprini, Mélissa, Jude and all the others for being a part of this incredible journey. Special thanks to Guillaume

who taught me the clean room fabrication techniques. Special thanks also to Soong-Geun Je for helping so much with the measurements of current-induced skyrmion motion. My sincere thanks to the administrative staff as well: Rachel, Catherine, Léa and Sabrina for their patience and ever smiling faces. Of course without them the amazing conferences I attended would not have been possible.

I thank my friends who never let me feel homesick during these years. Thank you Rahul (for being so happy-go lucky), Dhruv (for being so supportive and encouraging), Amit (for your kindness and patience). Thank you Yashpreet, Preeti, Siddharth, Vikas, Shweta, Abhinav, and Mahendra and all the other people who were a part of this adventure.

Coming now to the people who inculcated the 'french' habits in me, spoiling me with cheese, wine etc and also for being the loveliest flatmates. Thank you Romy, Pape and Luca.

I would now like to specially thank the person who has not only helped me academically but also emotionally, putting up with all my ups and downs. Thank you Roméo for your unconditional love, support, care, patience and of course also for carrying out micromagnetic simulations.

In the end I would like to thank my family : Maa, Papa and Bhai without whom this journey would have been impossible. I owe you everything that I am and hope to become. A big thank you to my grandparents too who have been so enthusiastic about my work and have always been so proud of me.

Abstract

Control of interfacial magnetism has emerged to be of paramount importance for spintronics applications specially involving chiral magnetic structures called skyrmions. Skyrmions are envisaged to be the future information carriers owing to their solitonic properties. In heavy metal/ ferromagnet/ insulator heterostructures, skyrmions are stabilized by interfacial Dzyaloshinskii-Moriya interaction which is an antisymmetric exchange and competes with other interactions like symmetric exchange, dipolar and magnetic anisotropy. In order to tune skyrmions, the interfacial magnetic properties need to be modulated. One of the energy efficient tools to maneuver interfacial magnetism is electric field effect. Voltage gating has been shown, in a number of studies since 2009, to locally and dynamically tune magnetic properties like interface anisotropy and saturation magnetization. However, its effect on interfacial Dzyaloshinskii-Moriya Interaction (DMI), which is crucial for the stability of magnetic skyrmions, has been challenging to achieve and has not been reported yet for ultrathin films. This was one of the major motivations of this thesis.

In order to achieve the aforementioned goals, we first carry out an optimization of trilayer systems consisting of a heavy metal/ ferromagnet/ metal-oxide in which skyrmions can be stabilized. In particular, we focus on the Ta/FeCoB/TaOx system to nucleate skyrmions in the presence of very small out-of-plane magnetic fields. Further, we study and compare skyrmion nucleation in two different transition zones: out-of-plane anisotropy to paramagnetic and out-of-plane to in-plane anisotropy which is a function of the FeCoB thickness and TaOx oxidation state. Finally, we show electric field induced modulation of interfacial DMI which forms the most important result of this thesis. We demonstrate 130% variation of DMI with electric field in Ta/FeCoB/TaOx trilayers through Brillouin Light Spectroscopy (BLS). Using polar Magneto-Optical-Kerr-Effect microscopy, we further reveal a monotonic variation of DMI and skyrmionic bubble size with electric field, with an unprecedented efficiency. Since the electric field acts mainly on the FeCoB/TaOx interface, the voltage induced DMI variation points at the existence of the Rashba DMI explaining its high sensitivity to an applied voltage. We anticipate through our observations that a sign reversal of DMI with electric field is possible, leading to a chirality switch. This dynamic manipulation of DMI establishes an additional degree of control to engineer programmable skyrmion based memory, logic or neuromorphic devices.

Résumé

Le contrôle du magnétisme aux interfaces s'est avéré essentiel pour la spintronique et ses applications, en particulier celles basées sur des structures chirales de l'aimantation appelées skyrmions magnétiques. Ces skyrmions, décrits comme des solitons magnétiques, potentiels porteurs d'information, sont des candidats prometteurs pour le développement de nouvelles mémoires denses et non-volatiles. Dans des empilements ultraminces du type métal lourd / ferromagnétique / isolant, les skyrmions sont stabilisés par une interaction d'échange anti-symétrique d'interface appelée interaction de Dzyaloshinskii-Moriya (DMI); celle-ci entre en compétition avec d'autres interactions telles que l'interaction d'échange symétrique, l'anisotropie magnétique et l'interaction dipolaire. Afin de contrôler ces skyrmions, les propriétés magnétiques aux interfaces doivent être ajustées finement et modulées par une excitation extérieure. Le champ électrique s'est avéré être un outil efficace pour manipuler ces propriétés d'interface. Il a notamment été montré dans un certain nombre d'études depuis 2009 qu'une différence de potentiel permet de modifier localement et de manière dynamique des propriétés telles que l'anisotropie magnéto-cristalline ou l'aimantation à saturation. Cependant cet effet sur le DMI, qu'il est crucial d'intégrer pour les systèmes avec skyrmions, n'a jusqu'alors jamais été rapporté dans des films ultraminces et constitue une des principales motivations de cette thèse.

Afin d'atteindre les objectifs donnés ci-dessus, une optimisation des systèmes tricouches de type métal lourd/ferromagnétique/oxide dans lesquels peuvent exister des skyrmions est d'abord réalisée. En particulier, l'étude se concentre sur le système Ta/FeCoB/TaOx, dans lequel la nucléation de skyrmions par de faibles champs magnétiques est observée. Une étude approfondie en fonction de l'épaisseur de FeCoB et de l'état d'oxidation du TaOx a notamment été menée, permettant ainsi d'identifier les différentes zones de transition présentant des skyrmions: une zone de transition entre anisotropie perpendiculaire et état paramagnétique et une zone de transition entre anisotropie perpendiculaire et anisotropie planaire. D'autre part, le résultat majeur de cette thèse est la démonstration de la modulation de la DMI par un champ électrique dans une tricouche Ta/FeCoB/TaOx. Des mesures de spectroscopie Brillouin sous champ électrique ont révélé une très grande variation allant jusqu'à 130%. Puis, des observations complémentaires en microscopie à effet Kerr magnéto-optique ont permis de mesurer simultanément une variation monotone de la DMI et de la taille des skyrmions en fonction du champ électrique avec une efficacité sans précédent. Puisque le champ électrique agit principalement sur l'interface entre le matériau ferromagnétique et l'oxyde (FeCoB/TaOx), cette étude indique l'existence d'une DMI de type Rashba, expliquant la forte sensibilité au champ électrique. Ces observations montrent également qu'un renversement du signe de la DMI est possible, qui conduirait à une inversion de la chiralité des skyrmions. Cette manipulation dynamique de la DMI permettrait de conférer un degré de contrôle supplémentaire pour le développement de mémoires ou de dispositifs logiques ou neuromorphiques à base de skyrmions.

Contents

1

Introduction

Spintronics is emerging to complement the traditional semiconductor electronics by transcending some of its limitations and rendering novel ideas. We know that the term 'electronics' refers to the engineering and applications related to the emission, flow and control of electrons in vacuum and media. In analogy, 'spintronics' deals with the control of the spin of the electron in terms of its storage and transport hence adding another degree of freedom in addition to its 'charge'. Spin of an electron is a purely quantum mechanical concept which manifests in the form of its intrinsic magnetic moment. Spintronics hence amalgamates electric and magnetic degrees of freedom to produce a dense network of ideas that can be channelized to address the issues of high energy consumption and miniaturization limitation of the conventional electronics.

The advancement in nanotechnology in the 1980s and specially the control over metallic depositions made it possible to create materials with layers of superior quality whose thicknesses are in the order of few nanometers boosting the exploitation of electron spin. There has been a spectacular evolution in the field of spintronics over the past twenty years. The first breakthrough was the discovery of Giant Magneto-Resistance (GMR) effect by Albert Fert[1] and Peter Grunberg[2] in 1980's which also earned them the Nobel Prize in Physics in 2007. GMR is basically the change in the electric resistance when the relative orientation of magnetization in two ferromagnetic layers separated by a metallic spacer, changes in response to an applied magnetic field. It therefore evidenced the existence of spin-dependent transport across such structures. In fact it led to the employment of GMR sensors as read heads in magnetic Hard Disk Drives (HDD) to determine magnetization orientation of small domains (acting as bits) improving the storage density by 3 orders of magnitude.

Also, instead of metallic spacers, the use of insulators such as MgO[3, 4] further improved magneto-resistance signals drastically. When two ferromagnetic films are separated by an ultrathin insulating film (typically 1 nm), spin-dependent tunneling occurs across the insulator. The tunneling being dependent on the relative magnetization orientation in two ferromagnetic layers, produces a difference in the electrical resistance known as Tunnel Magneto-Resistance (TMR)[5, 6]. The resistance difference is maximum between the two limiting states *i.e.* where the magnetization in the two ferromagnetic layers are parallel and the one where they are antiparallel. These two states can then be channelized for storing information as bits: 0 for the low resistance state (parallel) and 1 for the high resistance state (antiparallel). This eventually led to the concept of Magnetic Random Access Memories (MRAM).

The conventional Random Access Memory (RAM) based on semiconductor technology is the part of a computer's main memory which enables fast read and write operations (access time in the order of ns) unlike other kinds of storage for example HDD (access time in the order of ms). However the RAM is volatile, *i.e.* the data is lost when the power is switched off. MRAM therefore has gathered a lot of attention as it offers non-volatility along with quick data read and

write facility. Moreover, MRAM can operate at higher temperatures, it is radiation resistant and consumes lesser energy, making it even more useful. In spite of these advantages, MRAM is still struggling in terms of providing high storage density. This has led scientists to push the frontiers of conventional spintronics based on MRAM. One of the alternatives that came up was the use of magnetic domains as information carriers in so-called domain wall racetrack memories. The idea was originally proposed by Stuart Parkin[7], to construct 3D devices consisting of nanowires of magnetic material arranged perpendicularly on the surface of a silicon substrate. It works like a shift register in which the data bits (magnetic domains) are moved to and fro by an electrical current along the racetrack with integrated reading and writing elements. This is challenging in terms of getting controlled and reliable motion of domain walls and requires high current densities for their motion. Another approach to overcome these problems was to focus on chiral magnetic textures such as skyrmions.

Magnetic skyrmions[8] are quasiparticle magnetic spin configurations with a non trivial topology. They are like knots in the magnetic medium that could not be unwound owing to their chirality. A chiral object possesses the property of being non superimposible on its mirror image. In the context of magnetic systems, chirality refers to the energy difference arising due to the sense of rotation of magnetic moments in a specific pattern (clockwise or anticlockwise). Skyrmions are hence small (typically between $10\text{nm} \sim 3\mu\text{m}$) circular magnetic domains enclosed by homochiral domain walls which can have either a clockwise (right-handed) or anticlockwise (left-handed) configuration. This chirality appears due to an antisymmetric exchange interaction called Dzyaloshinskii-Moriya Interaction (DMI). The DMI favors non collinear spin configuration, which exits both in bulk systems (bulk-DMI) and ultra-thin multilayer systems composed of heavy metal (HM)/ferromagnet (FM)/metal oxide (MOx) (interfacial DMI). Skyrmions are therefore largely dependent on the DMI, the sign of which determines their chirality. In ulta-thin HM/FM/MOx system, the interfacial DMI is also in competition with other interactions like exchange, magnetic anisotropy and dipolar interactions. Skyrmions are now envisioned to be one of the potential candidates for memory and logic applications due to their solitonic nature, small size and tunability[9]. However they face many challenges before their implementation in spintronic devices. The current research therefore aims towards optimizing the skyrmions in thin film trilayer systems, in terms of their nucleation, size, chirality, stability and motion by tuning the aforementioned magnetic properties.

Several methods have been proposed to tune the magnetic properties in HM/FM/MOx systems. This includes optimization of thicknesses of FM and MOx layers to achieve desired magnetic anisotropy and stacking appropriate HM/FM or FM/MOx interfaces to enhance the interfacial DMI. These are the static ways to maneuver the magnetic properties. One of the dynamic ways to address the interfacial magnetic properties is the use of applied voltage. When a voltage is applied across such a system, a re-distribution of electrons occurs in the orbitals at the interface between FM and MOx which is known to change the magnetic properties like anisotropy. Electric field effect was initially proposed for MRAMs to reduce the power consumption in writing operation. Recently electric field induced manipulation of skyrmions was demonstrated which was attributed to the variation of magnetic anisotropy and saturation magnetization. However, the influence of voltage on DMI in the case of ultra-thin film systems had not been addressed until the beginning of my thesis. A theoretical prediction of voltage induced DMI modification exists in the literature. An important thing to note is that as the

electric field acts mainly on the ferromagnet/metal oxide interface due to the screening effect, the DMI emerging from this interface will be the one affected (Rashba type) than the one from heavy metal/ferromagnet interface (Fert-Levy type).

The above mentioned challenges and techniques have inspired the work of my thesis. I have studied and optimized ultra-thin HM/FM/MOx systems particularly Ta/FeCoB/TaOx, to have access to skyrmions in different thickness ranges of the FM and MOx layers. Then most importantly I have studied the skyrmions under applied electric field and quantified the change in the different magnetic properties. In particular, I exhibit electric field modulation of DMI in ultra-thin film trilayer (HM/FM/MOx) system in order to tune skyrmions in terms of their size and chirality which has not been done before in literature. Moreover this study makes the existence of Rashba-DMI contribution from the FM/MOx plausible which until now had only been theoretically discussed.

The thesis is organized as following:

Outline of the thesis

The thesis is divided into three broad parts namely: Theoretical Background and the State of the Art, Methods and Characterization techniques and finally Results and Discussion. Each part is further divided into several chapters with their brief summary given below:

Part I: Theoretical Background and State of the Art

Chapter 2 : Interfacial magnetism. This chapter introduces the basics of understanding magnetism at the interfaces. Further, the intricate phenomena associated with the spin orbit coupling and broken inversion symmetry in ultra-thin multilayer structures are described. The different types of interfacial DMI contributions are also explained.

Chapter 3 : Magnetic spin textures. This chapter highlights the intricacies of magnetic phenomena at the interfaces in HM/FM/MOx systems and how it steers the formation of chiral magnetic structures, in particular skyrmions and skyrmionic bubbles, leading to a new paradigm of spin-based application, more specifically for memory and logic operations

Chapter 4 : Manipulation of interfacial magnetic properties. This chapter focuses on the manipulation of interfacial magnetic properties as a means to tune skyrmions. The interfacial magnetic properties like magnetic anisotropy and DMI can be tuned by several methods which involves appropriate choice of materials, their respective thicknesses, interface quality, temperature dependence and applied voltages.

Part II: Methods and Characterization Techniques

Chapter 5 In this chapter, the sample fabrication patterning and characterization techniques are explained.The various steps involved in preparing the samples for experiments under applied voltage are described. It includes deposition of insulator (oxides) followed by transparent

electrode and its patterning. Further characterization techniques, namely: Magneto-Optic Kerr Effect (MOKE) magnetometery and microscopy, Brillouin Light Spectroscopy (BLS) and Vibrating Sample Magnetometer (VSM) are detailed.

Part III: Results and Discussion

Chapter 6 : Study of different Heavy Metal/Ferromagnet/Metal Oxide systems This chapter presents the material development I have done of ultra-thin ferromagnetic (FM) layer and heavy metals or/and oxides to optimize magnetic anisotropy and find the parameters which stabilize skyrmions and skyrmionic bubbles. The adjustment of magnetic properties has been done by varying the ferromagnetic layer thickness and the oxidation state of the ferromagnetic/oxide interface by using gradients of thicknesses. A phenomenological model is constructed to better interpret the variation of magnetic properties as a function of the thickness gradients and the interface oxidation state. This enables us in the end to better understand the optimum conditions for magnetic anisotropy and dead layers.

Chapter 7 : Observation of magnetic skyrmions This chapter focuses on the energy landscape for skyrmion phase depending on the magnetic properties which vary as a function of ferromagnetic and insulator layer thickness and its oxidation in Ta/FeCoB/TaOx system. The experimental observation of skyrmion bubbles in different transition zones using Polar Magneto-Optic Kerr Effect Microscopy (p-MOKE) is presented. The difference between the different skyrmionic zones is highlighted.

Chapter 8 : Electric field effect on Ta/FeCoB/TaOx systems This chapter constitutes the most important result of my PhD which is electric field inuced modification of interfacial DMI. For this study we chose Ta/FeCoB/TaOx system, hosting magnetic skyrmions for the optimized deposition parameters. We performed Brillouin Light Spectroscopy measurements to directly determine the changes in the interfacial DMI of this system as a function of applied electric field. We further performed MOKE measurements on the same sample to highlight the time scale effects of the electric field on DMI and other magnetic properties simultaneously. Micromagnetic simulations were then performed using the experimentally obtained parameters to give a deeper insight into the internal structure of skyrmions expected at different voltages as a result of the change in its magnetic properties.

Chapter 9 : Conclusion This chapter summarizes the important results of the thesis.

Chapter 10 : Perspectives and Offshoots In this chapter some immediate perspectives of my work are presented along with the other studies in which I took part during my PhD. The first part deals with the generation of skyrmion bubbles and skyrmion bubble lattices from a ferromagnetic state at room temperature in Ta/FeCoB/TaOx sample by a controlled by single ultrafast (35-fs) laser pulse. The skyrmion bubble density is seen to increase with the laser fluence, and later attains saturation, forming disordered hexagonal lattices which enhances their topological stability. This study is promising for skyrmion based synaptic devices. In the

second part another study which was conducted on our sample consisting of Ta/FeCoB/TaOx by collaborators from Osaka University is briefly described. It is related to the study of the response of the skyrmions to thermal agitation hence their brownian motion.

Part I

Theoretical Background and State of the Art

2

Interfacial Magnetism

2.A Introduction

This chapter first introduces some basic ideas to provide the framework of understanding interfacial magnetism and then goes into the intricate phenomena associated with the interfaces in ultra thin film multilayer structures.

2.B Magnetic order and associated energies

Magnetism finds its origin in the motion of the electric charges. On an atomic scale it pertains to the spinning of electrons and their orbital motion around the nuclei. These motions constituting small current loops are referred to as magnetic dipoles with their associated magnetic moments. For materials with their electronic orbits full *i.e.* all the electrons being paired, the resultant magnetic moment is zero. These materials are hence diamagnetic. However when the outermost orbit has unpaired electrons, a net magnetic moment exists leading either to paramagnetism or ferromagnetism. In the case of paramagnets, an overall cancellation of the magnetic moment occurs due their randomization at room temperature in the absence of any applied magnetic field. However in case of ferromagnets, a net magnetic polarization/magnetization exists due to exchange interaction between neighboring moments, denoted by M and is equal to magnetic moments per unit volume.

Magnetism may also be induced in some materials by applying an external magnetic field. The magnetic susceptibility as the name suggests pertains to the sensitivity of a material to an applied magnetic field H and is denoted by χ=M/H. The response of different types of magnetic materials leads to their classification into the following groups in the localized picture.

2.B.1 Types of magnetic behavior

Diamagnetism : Diamagnetic substances are composed of atoms which have no net magnetic moments (*i.e.* all the orbital shells are filled and there are no unpaired electrons). However, when exposed to a magnetic field, a negative magnetization is produced and thus the susceptibility is negative. The behavior is similar to the Lenz's law in electromagnetism: when the flux through an electrical circuit is changed, an induced (diamagnetic) current is set up in such a direction as to oppose the flux change. Diamagnetism is intrinsically present in all materials but is weaker ($\chi \sim -10^{-6}$) as compared to paramagnetism and is therefore prominent in materials with even number of electrons where the other phenomena are dormant.

Paramagnetism : Paramagnetism springs from a net magnetic moment due to unpaired electrons in partially filled orbitals. When a magnetic field is applied, it causes partial alignment of the atomic magnetic moments in the direction of the field, resulting in a net magnetization and positive susceptibility. However, the interaction of the individual magnetic moments is smaller than the thermal energy, and the magnetization is zero when the field is removed. Thus this phenomena is opposed by thermal energy resulting in randomization. The susceptibility is positive hence is a function of temperature and scales as $\chi \sim 1/T$ known as Curie's Law. Usually at room temperature the paramagnetic susceptibility is small ($\chi \sim 10^{-2}$) but larger than diamagnetic susceptibility.

Ferromagnetism : Ferromagnetism is the property of acquiring a spontaneous net magnetization in the absence of magnetic field below the ordering temperature. It is ascribed to the collective interaction (exchange interaction) between the neighboring magnetic moments in a material leading to their preferential alignment in the same direction. Despite that, the overall magnetization of a ferromagnetic material can be low in the absence of magnetic field due to its fragmentation in separate ordered regions called domains which are individually ordered but collectively assembled with moments pointing in different directions. The ferromagnetic susceptibility defined in this case as $\chi = \frac{\partial M}{\partial H}$ is positive and huge ($\chi \sim 10^4 - 10^6$) ; *i.e.* in the presence of a magnetic field all the respective domains align along its direction. The Curie temperature T_C which is the ordering temperature (Curie-Weiss law: $\chi = \frac{C}{T-T_C}$, where C is the Curie constant) is also quite high being in the order of 1000K for transition metals like Fe, Ni, and Co.

Antiferromagnetism : Antiferromagnetism results in zero net magnetization in a material due to complete cancellation of magnetic moments oriented opposite (anti-parallel) to each other as a result of negative exchange interaction between the neighboring moments. It can also be described as a magnetic crystal having two sub-lattices with equal but opposite magnetization. This type of spontaneous magnetic ordering is again dependent on temperature called Néel temperature T_N in this case above which it gets disrupted. The Néel temperature is named after the physicist Louis Néel, who was the first to explain antiferromagnetism in 1936. When a magnetic field is applied at temperatures below T_N, antiferromagnet exhibits a weak response as the field has to overcome the strong collective negative exchange. However at elevated temperatures the antiferromagnetic order is broken to exhibit weak paramagnetism.

Examples include hematite, metals such as chromium, alloys such as iron manganese (FeMn), and oxides such as nickel oxide (NiO). Antiferromagnets are often used in spintronics to pin the magnetization of an adjacent ferromagnet by exchange coupling. The pinned layer serves as a reference in magnetic tunnel junction-based magnetic memories/sensors.

Ferrimagnetism : When the magnetization is not fully compensated by oppositely oriented magnetic moments in the two sub-lattices composing the antiferromagnetic structure, it results in ferrimagnetism. Though the intrinsic ordering is different, a ferrimagnet displays similar characteristics as that of a ferromagnet. Magnetite (Fe_3O_4) is one such example. The temperature dependence of a ferrimagnet can be complex if the Curie temperature T_c of the two sublattices are not identical.

Figure 2.1 describes the different magnetic orders in a pictorial representation (a), and Magnetic Susceptibility (b) as a function of temperatures for the same.

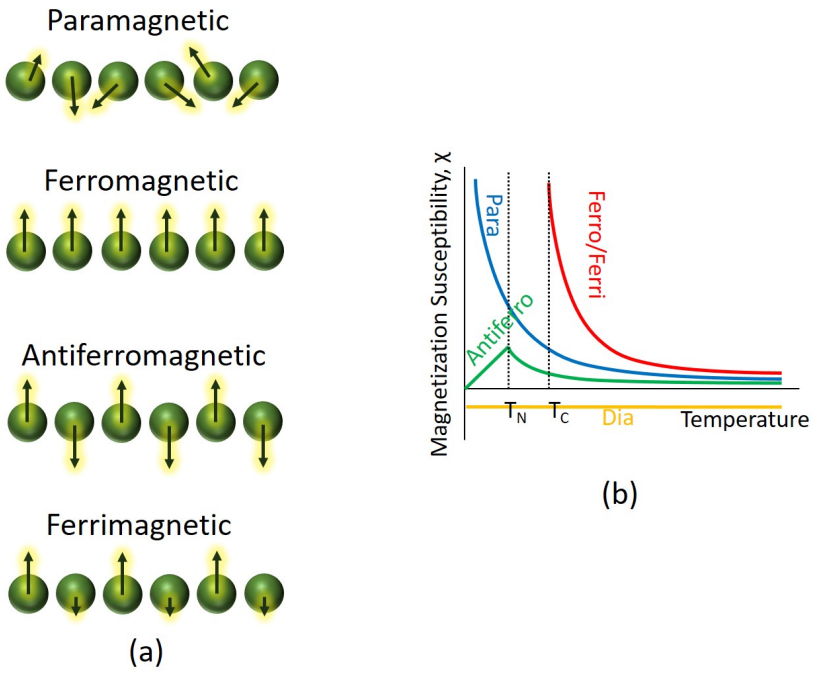

Figure 2.1 – (a)Pictorial representation of natural magnetic ordering. (b) Magnetic susceptibility χ as function of temperature for Ferro,Ferri,Para and Antiferromagnets. Note that $\chi < 0$ for diamagnets and is independent of temperature. For ferro and ferrimagnets χ drops above T_C leading to a paramagnetic behavior. Same is the case for antiferromagnets above T_N

Artificial Magnetic Order : Artificial magnetic order can also be created by combining two or more magnetic materials and metals. Synthetic Antiferromagnet (SAF) and Ferrimagnets are composed of two magnetic layers for example Co separated by a spacer ($\sim$ 1nm) for example Ru. This type of arrangement is easier to tune and control as compared to the natural antiferromagnets and ferrimagnets as the effective interaction can be tuned depending on the nature and thickness of the spacer. The phenomena resulting in such type of interaction

is interlayer exchange coupling[10, 11] often referred to as the Ruderman-Kittel-Kasuya-Yosida (RKKY) interaction. As a function of the spacer layer thickness, it results in an oscillatory behavior of the magnetic ordering, alternating between preferred parallel and antiparallel magnetization alignment of the two magnetic layers.

2.B.2 Types of magnetic energy

The discussion now will be oriented towards ferromagnetism in thin film systems. There are several interactions at play that determine the total energy and give rise to a certain magnetic configuration and its dynamics inside a ferromagnet. Both quantum mechanical and micromagnetic continuum approach have been highlighted[12–15]:

Exchange Energy : Exchange energy is the result of quantum mechanical interaction between neighboring spins/magnetic moments. It is expressed as

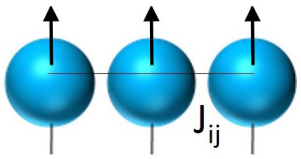

$$\mathcal{E}_{ij} = -\mathcal{J}_{ij}\vec{S_i}.\vec{S_j} \tag{2.1}$$

where $\mathcal{J}_{)|}$ is the Heisenberg exchange constant. It favors a collinear arrangement of spins *i.e.* the spins like to orient parallel or antiparallel to each other. For ferromagnets, $\mathcal{J} > 0$, resulting in parallel alignment. For a chain of 1-D spins the expression becomes

$$\mathcal{E}_{ij} = -\mathcal{J}S^2 \sum_{i,j} \cos\phi_{i,j},\ \phi_{i,j} \sim \mid m_i - m_j \mid where\ m = M/M_s. \tag{2.2}$$

$$\mathcal{E}_{ij} = -\mathcal{J}S^2\left(1 - \frac{\phi_{ij}^2}{2}\right),\ for\ small\ \phi_{i,j} \tag{2.3}$$

$$\mathcal{E}_{ij} = Constant + \frac{\mathcal{J}S^2 z}{2a}\left(\frac{\partial\phi_{ij}}{\partial x}\right)^2 \tag{2.4}$$

In the micromagnetic continuum approach, the energy cost has to be paid if the magnetization is non uniform within the volume of the magnetic material. Ignoring the discrete nature of the lattice, we can write the total exchange energy as:

$$E_{ex} = A\int_V [(\nabla\vec{m})^2]dV \tag{2.5}$$

where $A \simeq \mathcal{J}S^2 z/2a$ is called the exchange stiffness constant (z is the number of sites in a unit cell, a is the nearest-neighbor distance or the lattice parameter) and is expressed in J/m.

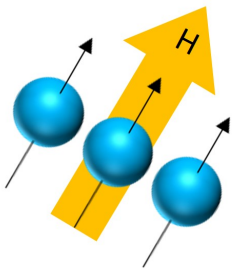

Zeeman Energy : Zeeman energy is the energy of a magnetic moment or that of the magnetic system as a whole in the presence of an external magnetic field. It leads to the alignment of the magnetization along the applied magnetic field. It is expressed as

$$E_z = -\mu_0\int_V \vec{M}.\vec{H}dV \tag{2.6}$$

where M is the magnetization and H is the applied magnetic field and V is the volume of the ferromagnet.

Dipolar Energy : Dipolar energy is a long-range type of interaction. Depending on the arrangement of magnetic moments in a system, magnetic charges arise at the surfaces, giving rise to stray fields. Therefore to minimize this energy cost, the magnetization tends to align in the direction such that the surface charges are minimum. The dipolar energy is expressed as:

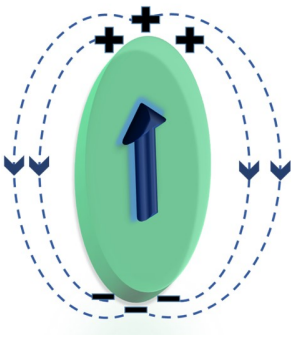

$$E_d = -\frac{\mu_0}{2}\int_V M.H_d dV \tag{2.7}$$

Here H_d =-$\mathcal{N}$.M and $\mathcal{N}$ is the shape-dependent demagnetizing tensor and V the volume of the ferromagnet. This energy is also known as the magneto-static energy or shape anisotropy energy as we see that it is largely governed by the shape of the system. Further as the curl of $\vec{H_d}$ is zero, it can be written as $\vec{H_d} = -\vec{\nabla}\phi$ where ϕ is a potential. Using the concept of magnetic volume charges ($\rho = -\vec{\nabla}.\vec{M}$) and surface charges($\sigma = \vec{M}.\vec{n}$), the magneto-static energy can be expressed as:

$$E_d = \frac{\mu_0 M_s}{2}\left(\int_V \rho\phi dV + \int_S \sigma\phi dS\right) \tag{2.8}$$

Therefore we see that to minimize this energy, the magnetic charges need to be minimized. For minimizing volume charges, $\vec{\nabla}.\vec{M}$ has to be small. For minimizing surface charges, the magnetization prefers to be parallel to the edges and surfaces of magnetic systems.

In case of thin films with uniform magnetization, $\mathcal{N}^{\perp}$=1 and $\mathcal{N}^{\parallel}$=0 , therefore dipolar energy per is defined as:

$$E_d = K_d \sin^2\theta \tag{2.9}$$

where K_d is the dipolar energy constant in mJ/m^3 given by:

$$K_d = -\frac{\mu_0}{2}M_s^2 \tag{2.10}$$

Therefore the shape anisotropy prefers the magnetization to lie in the sample plane.

Magnetocrystalline Anisotropy Energy : It is the energy arising out of preferential alignment of magnetization along certain crystallographic directions. The energy cost is minimum along easy axes/planes and maximum along hard axes/planes. Usually the volume density of magnetic anisotropy energy K is expressed in terms of any set of angular functions associated to the symmetry of the crystal structure. Materials with a cube-symmetric lattice structure like iron, nickel naturally feature three (Fe) or four (Ni) easy axes with their energy density given by

$$E_{mc} = K_{c0} + K_{c1}(\alpha_1^2\alpha_2^2 + \alpha_2^2\alpha_3^2 + \alpha_1^2\alpha_3^2) + K_{c2}(\alpha_1^2\alpha_2^2\alpha_3^2) \tag{2.11}$$

Here α gives the direction cosine, *i.e.*, the cosine of the angle between the magnetization direction and the crystal axis and K_{c0}, K_{c1} and K_{c2} are anisotropy constants. The energy density of such a cubic anisotropy is the result of an expansion in the magnetization components along the easy axes.

For uniaxial case in hexagonal crystals like cobalt, the magneto-crystalline energy density can be defined as

$$E_{mc} = K_1 sin^2\theta + K_2 sin^4\theta + ... \tag{2.12}$$

where θ is the angle between the easy axis and the magnetization and K_1 and K_2 are anisotropy constants. Very often the higher order terms are ignored due to their small contributions and the above expression is simplified as:

$$E_{mc} = K_u \sin^2\theta \tag{2.13}$$

such that K_u is the uniaxial anisotropy constant. The origin of this energy lies in the spin-orbit coupling mechanism describes subsequently in this chapter.

Interfacial Magnetic Anisotropy : One of the crucial discoveries in spintronics was Perpendicular Magnetic Anisotropy or Out-of-Plane Anisotropy in ultra-thin film systems. Most of the envisaged applications now rely on this phenomenon. It was first pointed out by Néel[16] that the difference in environment of the surface or the interface atoms as compared to the bulk atoms leads to interfacial or surface anisotropy which is otherwise considered negligible in thick or bulk materials. In other words, the break in the translational symmetry due to the presence of planar interfaces and surfaces in ultra-thin magnetic multilayer systems strongly affects the anisotropy energy of these systems. It could result in the easy direction of magnetization turning out of plane and hence is also known as Pependicular Magnetic Anisotropy (PMA). The origin of interface/surface energy contribution has been studied extensively. Many theoretical and experimental analysis have been done using various elements in multilayers. The reason has been primarily attributed to complex band hybridization at the interface. However, elastic stress due to lattice distortion can also contribute to this effect[17] (see figure 2.2). The effective magnetic anisotropy energy can be expressed as

$$E_{mc} = K_{eff} \sin^2\theta \tag{2.14}$$

where θ is the angle between the magnetization and the normal to the sample plane. K_{eff} is written as a sum of surface/interface (K_s) and volume contributions(K_v) .[18, 19]

$$K_{eff} = K_v + \frac{K_s}{t} \tag{2.15}$$

where $K_v = K_b + K_d$; K_b is the bulk magnetocrystalline anisotropy and K_d is the shape anisotropy and is negative, and t is the thickness of the ferromagnetic film. K_s includes surface contributions of the two interfaces.

If the surface/interface contribution is positive, then below a certain critical thickness ($t_c = -K_s/K_v$), it overcomes the volume contribution and results in K_{eff} becoming positive i.e the interface anisotropy becomes larger than the demagnetizing contribution in absolute value.

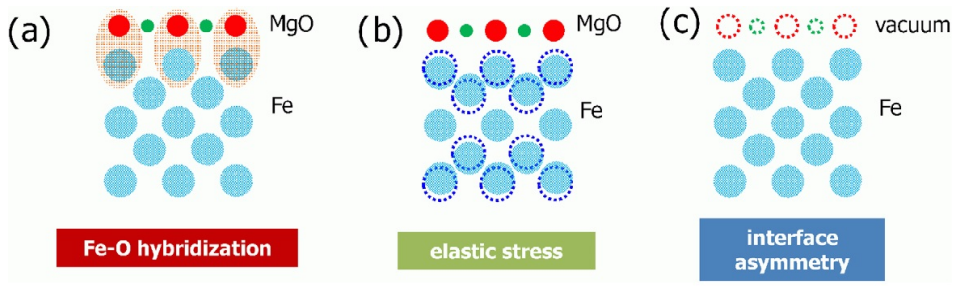

Figure 2.2 – Illustration of the three major contributions to the interfacial anisotropy of an Fe/MgO interface: (a) hybridization of the atomic orbitals of the magnetic layer and the barrier, (b) elastic stress due to the lattice distortion and (c) crystal symmetry breaking due to the interface. Circles show the position of the atoms of Fe, O, Mg corresponding respectively to the largest (blue), medium (red) and smallest (green) spheres. (a) Ellipses show hybridized Fe-O orbitals; (b) dotted circles correspond to initially undistorted Fe atom positions; (c) dotted circles represent the initial positions of Mg and O atoms before their removal to create vacuum/Fe interfa ce.[17]

In this case the easy direction of magnetization becomes perpendicular to the sample plane and hence leads to PMA.

In thin films of Fe or Co, bulk magnetocrystalline anisotropy is usually very small (except in the case of textured films where it is of the same order) with respect to the shape anisotropy. Therefore the volume contribution for the films that I studied in this thesis, mainly comes from the dipolar or shape anisotropy which we know favors in plane magnetization to minimize surface charges.

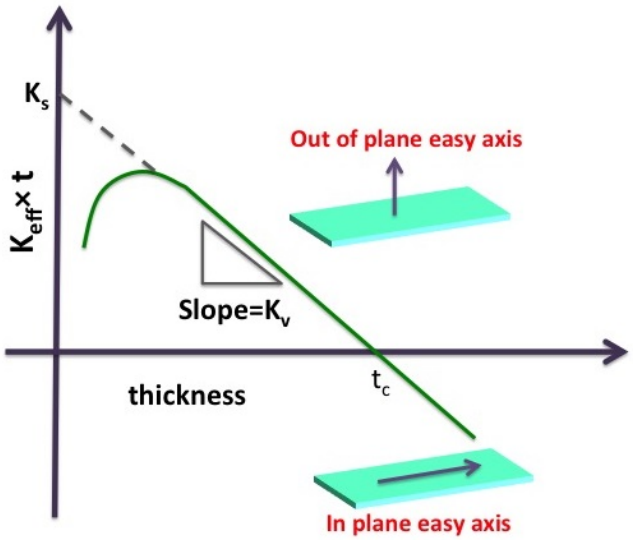

Figure 2.3 – Plot of effective magnetic anisotropy K_{eff} multiplied by the thickness t of the ferromagnet plot as a function of the ferromagnetic thickness. When $K_{eff} > 0$ the anisotropy is perpendicular to the surface *i.e.* out of plane, whereas when $K_{eff} < 0$, the anisotropy is in-plane i.e magnetization prefers to lie in the plane of the ferromagnetic film.

As can be seen in figure 2.3, the slope, equal to K_v is negative (as it is here mainly due to shape anisotropy) and the surface contribution K_s is positive and it contributes to PMA. We

can see that depending on the film thickness, an in-plane anisotropy is obtained for $t > t_c$, i.e. when $K_{eff} < 0$, and an out-of-plane anisotropy or PMA anisotropy is observed for $t < t_c$ when $K_{eff} > 0$.

Also, below a certain thickness (typically 2-3Å), the anisotropy starts to decrease due to the decrease of the Curie temperature as a result of the intermixing of the ferromagnet with the adjacent layers. A strong PMA is thus typically obtained around thicknesses of 1 nm with transition towards in-plane anisotropy at around 1.5 nm. In order to obtain PMA, the film thickness thus needs to be well controlled.

The PMA has been found and investigated both in ferromagnetic/non-magnetic metal multilayers (for example Co/Pd) and ferromagnetic metal/metal oxide thin films (for example Pt/Co/AlOx). Various combinations of these materials have been incorporated and studied in ultra-thin film multilayered structures.

2.C Phenomena due to SOC in the absence of inversion symmetry

After a broad overview over the magnetic interactions that exist in ferromagnets, we will now concentrate on the interactions solely arising due to interfaces. Interfaces between heavy metal/ferromagnet and ferromagnet/insulator in ultra-thin film systems are arenas of rich physical phenomena owing to strong spin-orbit coupling from the heavy metal layer and broken inversion symmetry due to the presence of interfaces. It amalgamates electrical and magnetic degrees of freedom leading to the control of one via the other.

Spin-Orbit Coupling (SOC) is a relativistic effect which is based on the interaction of electron's intrinsic spin with its motion in the orbit around the nucleus. A more generic explanation would be that a moving electron with velocity $\vec{v}$ in an electric field $\vec{E}$ due to the nucleus experiences an effective magnetic field in its rest frame given by

$$\vec{B} = \vec{E} \times \vec{v}/c^2 \tag{2.16}$$

where c is the speed of light. This leads to a Zeeman interaction between the electron's spin σ and the effective magnetic field which in turn is dependent on the momentum of the moving electron described by

$$H_{SO} = -\mu_B(\vec{E} \times \vec{v}/c^2).\vec{\sigma} \tag{2.17}$$

The electric field can stem from the nucleus of the same atom or ion, the neighboring ions or even broken inversion symmetry at an interface. This creates a plethora of phenomena holding immense potential for applications in Spintronics. As the SOC couples the spin and momentum degrees of freedom, one of its consequences in bulk ferromagnet is **Magneto-Crystalline Anisotropy (MCA)**. The crystal field due to neighboring ions together with SOC link the electron motion to the crystal lattice. This leads to the preferred alignment of electron moments hence the magnetization along certain axes (easy) over others (hard). In the case of ferromagnetic thin film systems where the inversion symmetry is broken at the interfaces, the SOC induces **Perpendicular Magnetic Anisotropy (PMA)** where the ground state magnetization prefers to be perpendicular to the interface. This PMA is subsequently enhanced when the thin film ferromagnet is interfaced with heavy metal owing to higher spin-orbit interaction.

A very striking result of the SOC combined with inversion asymmetry is antisymmetric exchange interaction called **Dzyaloshinskii-Moriya Interaction (DMI)**.

2.C.1 Interfacial Dzyaloshinskii-Moriya Interaction

An antisymmetric exchange interaction was first proposed by Dzyaloshinskii in 1957 to explain weak ferromagnetism due to canted moments in antiferromagnets[20]. Later, Moriya[21] linked the existence of this interaction to SOC mechanism and hence the term DMI was coined. SOC in the presence of inversion asymmetry leads to a non collinear arrangement of spins with a defined sense of rotation and this property is known as chirality. Chirality is one consequence of asymmetry. The presence of DMI hence leads to non-trivial whirling magnetic textures like skyrmions. DMI can exist both in bulk systems (referred to as bulk-DMI) like non-centrosymmetric crystals with a B20 crystallographic structure (MnSi and FeGe) where it originates in the bulk, and in thin film systems where it arises from the interface. Inversion asymmetry naturally exists in thin film multilayer systems composed of different materials. Therefore, in ultra-thin bi/tri-layer systems, the DMI being of interfacial origin, is called interfacial-DMI[22, 23]. We will mainly focus on the interfacial DMI for the rest of the discussion.

There have been two main approaches to quantify DMI in different systems. The first well known origin of interfacial DMI in a local moment model is described by Fert and Levy as the interaction between two neighboring magnetic ions with spins $\vec{S_i}$ and $\vec{S_j}$ mediated by a third ion with high SOC (usually a heavy metal)[24–26]. A recent proposition, which has not been experimentally observed until the beginning of my thesis, links the DMI and chiral structures to Rashba type SOC[27, 28].

Fert-Levy Model

Fert and Levy[24] described DMI as a result of interaction between two neighboring spins mediated by a third ion with high SOC.

Quantum mechanically this interaction can be written as:

$$\mathcal{E}_{DMI} = \vec{d_{ij}}.(\vec{S_i} \times \vec{S_j}) \tag{2.18}$$

Here $\vec{S_i}$ and $\vec{S_j}$ are two neighboring spins and $\vec{d_{ij}}$ is the DMI vector as shown in figure 2.4. This interaction leads to spin canting *i.e.* non collinear arrangement of spins hence directly opposing the exchange interaction. We can hence infer from the above equations that the energy of the spins is increased or decreased depending on the sense of rotation (clockwise or anticlockwise) from $\vec{S_i}$ to $\vec{S_j}$ around $\vec{d_{ij}}$ which in turn depends on the sign of $\vec{d_{ij}}$ and is material-specific. DMI was first demonstrated in disordered alloys and later was extended to interfaces between thin ferromagnetic and heavy metal layers[25]. The $\vec{d_{ij}}$ in this case points perpendicular to the plane formed by the three atoms such that $\vec{d_{ij}} = d_{ij}.(\vec{r_{ij}} \times \vec{z})$ where $\vec{r_{ij}}$ is the vector connecting the two spins and $\vec{z}$ is the direction normal to the film oriented from the heavy metal layer to the ferromagnetic thin film[25, 29–31] (see figure 2.4).

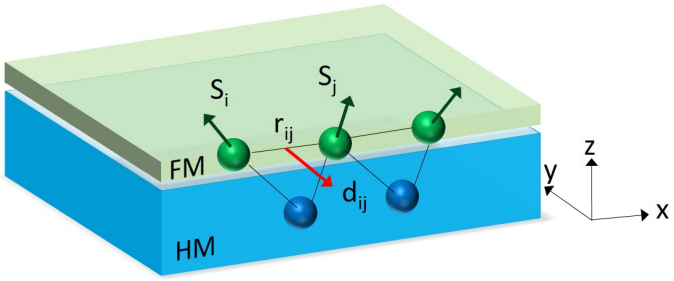

Figure 2.4 – The antisymmetric exchange interaction called Dzyaloshinskii-Moriya interaction described by Fert-Levy as an interaction between two adjacent spins S_i and S_j of a ferromagnet (FM) via heavy metal (HM) atom with strong spin orbit coupling.

Following a micromagnetic continuum approach the DMI energy can be written as follows[32–34]:

$$E_{DMI} = t\int_S D\left[\left(m_x\frac{\partial m_z}{\partial x} - m_z\frac{\partial m_x}{\partial x}\right) + \left(m_y\frac{\partial m_z}{\partial y} - m_z\frac{\partial m_y}{\partial y}\right)\right]dS \tag{2.19}$$

Here D is the effective DMI constant in J/m^2, t is the ferromagnetic film thickness, $m_i = M_i/M_s$ is the normalized magnetization and z is perpendicular to film plane. Theoretically it has been explained that the link between d_{ij} and D depends on the type of lattice scaling as $D = d/at$ where a is the lattice constant and t is the ferromagnetic film thickness.

The DMI, when large enough, competes with other magnetic interactions like exchange, dipolar and interface anisotropy to stabilize ground state chiral spin structures like chiral Néel walls or skyrmions described in detail in the next chapter. These magnetic textures hold immense potential for applications in next generation memory and logic devices. The DMI can be enhanced by structural designing of magnetic multilayers with insertions of heavy metal layers. For example Co on Pt favors anticlockwise rotation of spins. If the Pt/Co is interfaced with another Pt of the same thickness forming Pt/Co/Pt, in the ideal case, the DMI contributions from the two interfaces would cancel each other. Whereas Co on Ir favors a clockwise rotation (consistent with the study by Perini et al.[35]) of spins and hence due to the inversion of the local $\vec{z}$, an Ir/Co/Pt heterostructure leads to addition of the DMI contribution from the two interfaces and hence increases the overall DMI[36–38]. However the additive effects are not always straightforward. Since the DMI is of interfacial nature, the method of layer deposition and hence the quality of the interfaces affect the overall DMI. For example in the study by Hrabec et al.[39], a non zero DMI is observed for Pt/Co/Pt which varies as a function of thickness of Ir inserted in between.

Note that the convention A/B/C means the layer B is sandwiched between the layer A which is at the bottom and layer C which is at the top. We have chosen to use this convention throughout this thesis to be consistent.

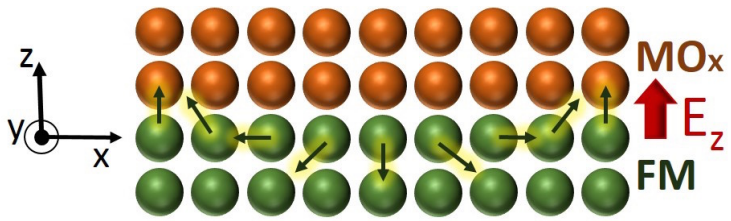

Figure 2.5 – Chiral configuration of magnetization due to the Rashba effect at the ferromagnet (FM) and metal oxide (MOx) interface which is exchange coupled to the conduction electrons moving in ±x direction at the same interface. E_z indicates the intrinsic interfacial electric field which leads to the Rashba effect.

Rashba Model

Another theory has been recently proposed to explain chiral magnetism in ultra thin-films with broken inversion symmetry. It is attributed to the Rashba effect[40, 41] at the interface[27]. In ultra-thin films due to inversion asymmetry, an electric field $E\hat{z}$ exists at the interface. The SOC in this case takes the form of the hamiltonian[27, 28]

$$H_R = \alpha_R \vec{\sigma}.(\vec{k} \times \vec{z}) \tag{2.20}$$

where α_R is Rashba parameter proportional to the electric field ($\alpha_R = -(\hbar^2 E/2m^2c^2)$) and $\vec{k}$ is the electron momentum; It results in spin split energy bands of electrons at the interface. The Rashba effective magnetic field given by[42]

$$\vec{B_R} \propto \alpha_R(\vec{k} \times \vec{z}) \tag{2.21}$$

is experienced by the itinerant electrons resulting in torques acting on magnetization. This mechanism is at the origin of the antisymmetric exchange interaction referred to as **Rashba-DMI**. The itinerant electrons experience spin precession around $\vec{B_R}$ and their exchange interaction with the local magnetic moments results in the magnetization canting with a specific chirality around the same $\vec{B_R}$ as shown in figure 2.5. This Rashba-SOC and thus Rashba-DMI is therefore capable of stabilizing chiral textures in ultra-thin film systems. In fact, it primarily accounts for the DMI contributions arising from ferromagnetic/insulator[43] interface for example Fe/MgO or Co/AlOx, where the Fert-Levy picture cannot completely explain the DMI mechanism. An extended derivation gives $D_{Rashba} = 2k_R A$[27] where D is the DMI constant for the Rashba-DMI, k_R is Rashba coefficient given by $k_R = 2\alpha_R m_e/\hbar^2$ and A is the exchange constant. As the Rashba parameter is proportional to the interfacial electric field, one of the most interesting features of this phenomenon is that it can be sensitive to applied external electric field to facilitate manipulation of spins. This would lead to tuning of the interfacial DMI with applied electric field which forms one of the major goals of this thesis.

2.C.2 Spin-Orbit Torques via Spin Hall and Rashba-Edelstein Effect

Apart from having a strong impact on the static magnetization configuration of ultra-thin ferromagnetic systems described above, SOC can also engage in generating **Spin-Orbit Torques**

(SOT) [44] to control the dynamics of the magnetization.

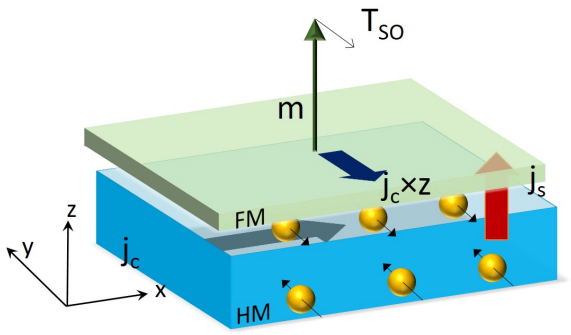

Figure 2.6 – Spin Hall Effect: leading to a transverse spin current j_s (z-direction) with spins polarized ($j_c \times z$) in y direction, in response to a charge current j_c(x-direction) in heavy metals (HM). This generates spin orbit torque which manipulates the magnetization m in the adjacent ferromagnetic (FM) layer.

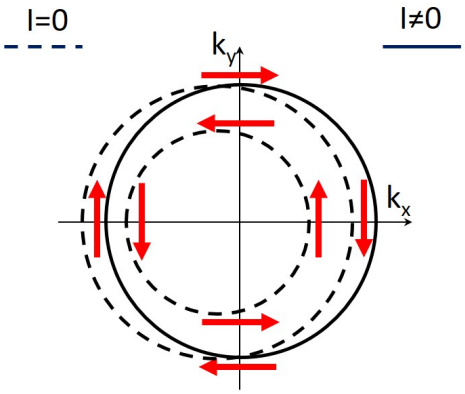

Figure 2.7 – Spin split Fermi surface of electron in the presence of Rashba spin orbit coupling. On the application of current the Fermi contour shifts resulting in a non zero spin density which diffuses as a spin current in an adjacent ferromagnetic layer leading to Spin-Orbit Torques.

There can be two sources of the spin-orbit torques: Spin Hall Effect (SHE) [45, 46] or Rashba-Edelstein effect. The SHE is a bulk effect that results in a spin accumulation at the lateral boundaries of a current-carrying conductor, with the directions of the spins being opposite at the opposing boundaries, as shown in figure 2.6. The charge current hence generates transverse spin currents which can be used to alter the magnetization of an adjacent ferromagnetic layer through transfer of angular momentum. The SHE contributions can be extrinsic: which is linked to Mott scattering, and intrinsic: which is based on the spin-orbit field of a crystal. The strength of the SHE is often described by Spin Hall Angle (θ_{SH}) which is the ratio of spin current generated over applied charge current. The SHE is therefore used to drive chiral domain walls and hence skyrmions via exerted SOT.

Another source of SOTs in ultra-thin film systems consisting of metal/ferromagnet interface is based on the Rashba effect which is of pure interfacial origin. The Rashba effect introduced earlier can induce a homogeneous net spin polarization, leading to a spin current perpendicular

to the applied charge current. This phenomenon is known as **Edelstein effect/Inverse spin Galvanic effect**[47, 48] and can be used to switch magnetization in the adjacent ferromagnetic layer by exerting Spin Orbit Torques (SOT) with the same symmetry as SHE. It can also be used to drive **chiral domain walls** or **skyrmions** in conjunction with SHE. Rashba spin-orbit interaction lifts the degeneracy between the spin up and down bands of conduction electrons at an interface as shown in figure 2.7. The spin state is strongly linked to the momentum k and is opposite for opposite momentum on a Fermi surface for energy minimization (due to time reversal symmetry). When a current is applied in the metal, it shifts this Fermi surface resulting in uneven occupation of k and -k momentum states which leads to spin accumulation. This spin accumulation generates SOTs on the adjacent ferromagnetic layer driving chiral Néel walls or skyrmions.

2.D Conclusion

We saw in this chapter the different magnetic energies that determine the stable magnetization configuration in ultra-thin film multilayer systems and also the phenomena specifically arising from at heavy metal/ferromagnet/metal oxide interfaces, in particular the Dzyaloshinskii-Moriya interaction and its different origins. We will now move on to see its consequences in the form of different magnetization textures in the next chapter.

3

Magnetic spin textures

3.A Introduction

Following the previous chapter based on the magnetic interactions at the interfaces in HM/FM/-MOx systems, the resulting magnetic configurations are now described. The discussion is mainly restricted to thin film systems. The different magnetic chiral textures and their respective advantages in applications are highlighted.

3.B Domains and Domain walls in thin films

A magnetic domain is a region within a ferromagnet where the magnetic moments are uniformly aligned constituting uniform magnetization. A magnetic material may consist of one or several domains. A demagnetized ferromagnet corresponds to a situation where the individual magnetization of each domain comprising it, is randomly oriented such that the net magnetization is canceled. A magnetized system on the other hand refers to the situation where the net magnetization is non-zero. The interplay of the different magnetic energies determines the domain structure in a ferromagnetic film. While the exchange energy prefers uniformly aligned neighboring magnetic moments and hence single-domain configurations, the dipolar energy favors flux closure to minimize surface charges and hence leads to splitting of domains. Anisotropy energy on the other hand likes the orientation of spins/magnetization along specific crystallographic directions ; leading to the existence of an easy axis or an easy plane for the magnetization. Depending on these, a certain number and shape of domains are created in

the ferromagnetic film in the ground state. Magnetic history of the film also plays a role in determining its ground state domain configuration.

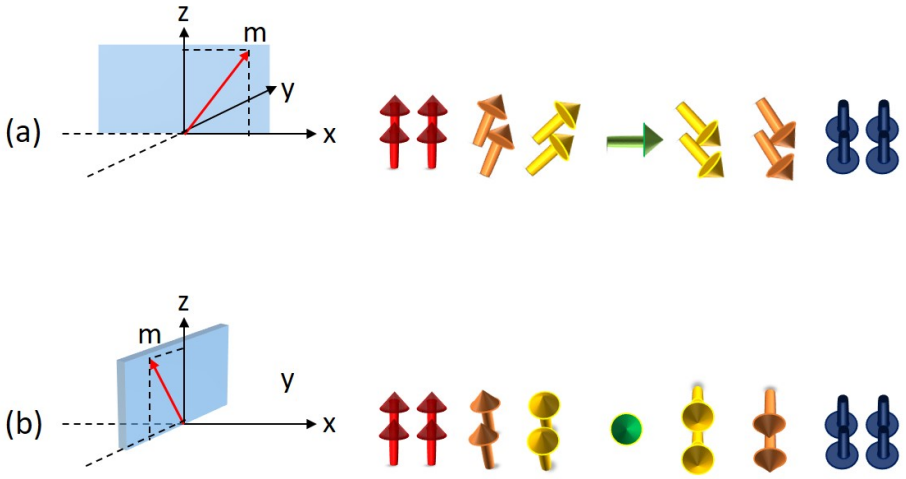

Figure 3.1 – The two types of domain walls with the indication of their plane of rotation of spins: (a) Néel type (b) Bloch type

A domain wall is a transition or a boundary separating two domains with opposite magnetization directions and its width depends on the characteristic length arising due to the competition between the different energies. In ultrathin ferromagnetic films (typically <1nm) the surface anisotropy dominates and leads to Perpendicular Magnetic Anisotropy (PMA) [16] making out-of-plane (OP) magnetization energetically favorable. The magnetization inside the domain wall can rotate in different ways ; the two limiting cases being (i) a spiral across the domain wall *i.e.* with the axis of rotation perpendicular to the domain wall plane called Bloch Wall (BW) [49, 50] and (ii) a cycloidal across the domain wall *i.e.* with the axis of rotation parallel to the plane of the domain wall called Néel wall (NW). They are represented schematically in figure 3.1.(a) and (b). In the case of ultrathin films with PMA, to determine what sort of domain wall costs lower energy, all the different magnetic energy terms need to be considered. While the other contributions remain the same, the cost in magnetostatic energy is higher for NW than for BW due to bulk magnetic charges hence favoring latter in usual cases. However, in the case of ultrathin films with PMA consisting of Heavy Metal/Ferromagnet/Metal Oxide (HM/FM/MOx), an antisymmetric exchange interaction called Dzyaloshinksii-Moriya Interaction (DMI) emerges ; as discussed in Chapter 2. On including the DMI energy contribution we obtain that the DMI alters the energy of NW depending on its sign.

To understand the contribution of DMI to the domain wall energy, I borrow the explanation from Rohart and Thiaville [34]. For simplicity, a 1-D system is considered such that z is the easy axis and the magnetization changes along the x-axis. As $\vec{d_{ij}}$ (the DMI vector) is orthogonal to $\vec{r_{ij}}$ (the vector connecting two spins), DMI favors magnetization rotation in the xz-plane (as z is the axis of the broken inversion symmetry) with a fixed chirality, therefore a single angle θ can

be used to describe the variation of m(x). With $\theta = \cos(\vec{m}, \vec{z})$, the total micromagnetic energy density reads

$$E[\theta(x)] = \int_{x_A}^{x_B} \left[A\left(\frac{\partial\theta}{\partial x}\right)^2 - D\frac{\partial\theta}{\partial x} - K_{eff}\cos^2\theta \right] dx \tag{3.1}$$

where x_A and x_B are the boundaries of the sample in the x direction, A is the exchange constant in J/m, D is the continuous effective DMI constant in J/m^2, $K_{eff}(=K_s/t - 1/2\mu_0 M_s^2)$ is the effective anisotropy of the system in J/m^3. In this equation we can notice that the exchange and anisotropy terms are independent of the sense of rotation of the magnetization ; *i.e.* they are invariant to the sign of θ. On the contrary, the DMI term is chiral such that lowest-energy states are expected for $\frac{\partial\theta}{\partial x}$ of the sign of D favored for the system. It is further shown using standard variation calculus that the function $\theta(x)$ which minimizes the energy is the solution of the following equations:

$$\frac{\partial^2\theta}{\partial x^2} = \frac{\sin\theta\cos\theta}{\Delta^2},\ x_A < x < x_B \tag{3.2}$$

$$\frac{\partial\theta}{\partial x} = \frac{1}{\zeta}, \qquad x = x_A \text{ or } x = x_B \tag{3.3}$$

where $\Delta = \sqrt{A/K_{eff}}$ is the Bloch-width parameter and $\zeta = 2A/D$ is related to DMI. By integration of 3.2 we obtain

$$\left(\frac{\partial\theta}{\partial x}\right)^2 = \frac{C + \sin^2\theta}{\Delta^2} \tag{3.4}$$

where C is an integration constant. Considering an infinite system in the x direction, if the D is small such that the domain-wall energy remains positive, the integration constant C must be zero so that no cycloid develops. Equation 3.4 now has two types of solution. The first one is uniform with $\theta = 0$ or π. The second one corresponds to a domain wall with

$$\theta(x) = 2\arctan\left[\exp\left(\pm\frac{x - x_0}{\Delta}\right)\right] + n\pi \tag{3.5}$$

where x_0 is the position of the domain wall and n an integer. The $\pm$ sign determines the chirality of the domain wall and n enables the two types of wall (from 0 to $\pm\pi$ or from $\pm\pi$ to $\pm 2\pi$). The domain wall energy can then be determined by using equations 3.1 and 3.5.

$$\sigma = 4\sqrt{AK_{eff}} \mp \pi D \tag{3.6}$$

We can hence infer from eq. 3.6 that the DMI introduces a chirality hence lowering the energy of the Néel wall favoring a sense of magnetization rotation in the x-z plane. Therefore, this contribution, when larger than the difference between NW and BW energies (which is due to magnetostatic energy cost arising in Néel type configuration), leads to stabilization of chiral Néel wall[51, 52].

3.C Chiral Domain walls

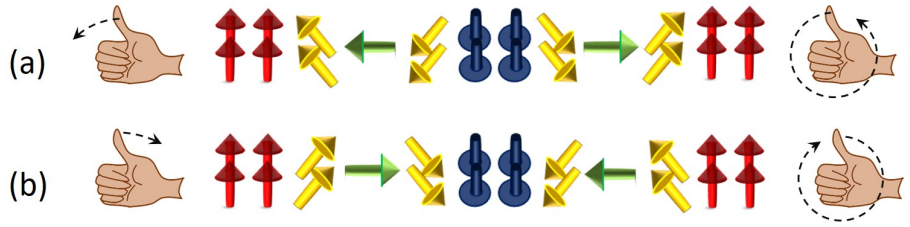

Figure 3.2 – (a) A left-handed chiral Néel domain wall : The spins rotate anticlockwise from up to down and back to up state . (b) A right handed chiral Néel domain wall: The spins rotate clockwise from up to down and back to up state. It can be seen that for both the cases the rotation is continuous.

When the DMI is large enough, more precisely when it is larger than a critical DMI value D_c ($D > D_c = 4\Delta K/\pi$)[29], a Néel type DW is energetically favored. In addition, the sign of the DMI parameter D detemrines the chirality of the NW[22, 23, 53]. Both Fert-Levy DMI[24] and Rashba[27] DMI play entangled roles in producing chiral magnetic textures. Note that there can be different conventions for the DMI sign and the associated chirality depending on the definition of the DMI vector *i.e.* whether $\vec{d_{ij}} = d_{ij}(\vec{r_{ij}} \times \vec{z})$ or $\vec{d_{ij}} = -d_{ij}(\vec{r_{ij}} \times \vec{z})$ where $\vec{r_{ij}}$ is the vector connecting the two spins and $\vec{z}$ is the axis of the broken inversion symmetry. We use the convention that a positive overall DMI ($D > 0$) results in the anticlockwise (ACW) sense of rotation of magnetization across the DW also called left-handed (LH) configuration and a negative DMI ($D < 0$) results in clockwise (CW) rotation called right-handed (RH) configuration. The two types of chiral configurations of Néel type of domain walls is depicted in figure 3.2.

3.D Magnetic Skyrmions

Skyrmions are named after the physicist Skyrme, who developed non linear field theory for interacting elementary particles and described topological configurations as particle like solutions[54]. A magnetic skyrmion[55, 56] is a chiral spin arrangement often described as a whirling spin texture in a magnetic material with particle-like properties[57]. Depending on the chirality, the spins constituting a skyrmion rotate in succession across its width, for example from being up at one edge to down at the center and up again at the other edge. The rotation of the spins is determined by the DMI vector $\vec{d_{ij}}$ introduced earlier. When $\vec{d_{ij}} \parallel \vec{r_{ij}}$ a Bloch-type skyrmion is energetically stable (figure 3.3(a)). On the other hand when $\vec{d_{ij}} \perp \vec{r_{ij}}$, it leads to Néel-type skyrmion (figure 3.3(b)). Skyrmions in two-dimensional case are defined by their winding number or topological number[58]:

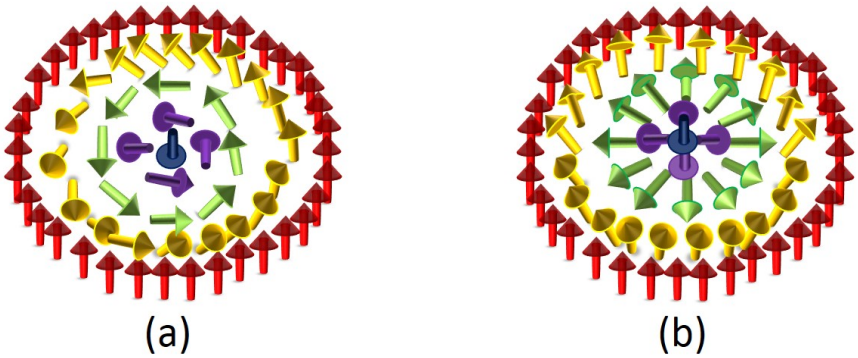

Figure 3.3 – Two types of skyrmions: (a) Bloch type which are stabilized by bulk-DMI and exist in bulk noncentrosymmetric crystals where the spins rotate continuously with their axis of rotation in the direction perpendicular to the plane of the domain wall (b) Néel type which are stabilized by interfacial DMI and exist in thin film systems and the spins rotate continuously with their axis of rotation in the plane of the domain wall.

$$S = \frac{1}{4\pi}\int \vec{m}.\left(\frac{\partial \vec{m}}{\partial x} \times \frac{\partial \vec{m}}{\partial y}\right) dxdy = \pm 1 \tag{3.7}$$

where $\vec{m}$ is the normalized local magnetization which in case of a skyrmion, when mapped on a unit sphere, covers it entirely (4π) and is hence quantized. The non-trivial topology renders the skyrmion topologically protected meaning that it cannot be unwound continuously to result in a state with different S. For example it cannot be transformed continuously to a uniformly magnetized state (S=0) without generating a singularity. Their finite extension due to their solitonic nature enables them to be channelized as information carriers.

Skyrmions were initially identified in B-20 magnetic compounds or thin film chiral magnets like MnSi[59], $Fe_{1-x}Co_xSi$[60] and FeGe[61]. In the case of B-20 magnets, the lack of inversion symmetry of the cristallographic structure gives rise to a bulk-DMI and stabilizes Bloch-like skyrmions below room temperature and under large external magnetic fields. Skyrmions were later observed in epitaxial ultrathin magnetic layers grown on heavy metals like Ir/Fe[22] and Ir/Fe/Pd[62]. Here the interfacial DMI due to broken inversion symmetry plays the pivotal role in stabilizing Néel-type skyrmion. However skyrmions in the abovementioned systems were only stable at low temperatures (<30K) and at high magnetic fields (in the order of T). Applications of skyrmions in spintronics necessitates them to exist at room temperature under zero applied magnetic field and with growth techniques that are compatible with industry requirements.

Therefore the research attention has shifted to sputter-deposited ultrathin films of HM/FM bilayer, HM_1/FM/HM_2 or HM/FM/I (Insulator) trilayers. Here the skyrmions have been observed at room temperature with much lower applied magnetic field. Multilayer stacks with PMA in fact enable additive DMI from several interfaces if the DMI sign is same from a given arrangement of

the individual layers. For several repetitions, it leads to the dipolar coupling of skyrmions in the successive ferromagnetic layers forming a columnar structure stable at room temperature due to large magnetic volume. For example in (Ir/Co/Pt) $\times 10$ skyrmions in the range of 30-90 nm were observed by Scanning Transmission X-ray Microscopy (STXM)[38]. Several other combinations of heavy metal, ferromagnet and metal oxides have been explored where skyrmions have been found to be stable at room temperature including Ta/CoFeB/TaOx trilayers (skyrmion radius R $\sim$ 1 μm)[63], (Pt/Co/Ta)$\times$15 (R $\sim$ 120 nm0) and (Pt/CoFeB/MgO)$\times$15 multilayers (R~120 nm)[64], Pt/Co/MgO trilayers (R~80 nm)[65], and Ta/CoFeB(/Ta)/MgO (R~450 nm)[66].

Skyrmionic bubbles

In several multilayer structures in the presence of interfacial DMI, a distinction is often made between DMI skyrmions (few nm) and dipolar-field skyrmions (few tens of nm to several μm)[67, 68]. Both types are indeed chiral and of the Néel type due to the DMI ; therefore, they share the same topological charge (=1) and are often referred to as skyrmions. The term skyrmionic bubble has been used to describe large μm-sized skyrmions[67, 69, 70]. These skyrmionic bubbles are different from classical bubbles that are only stabilized by dipolar interactions (*i.e.* in the absence of DMI) hence being Bloch-type bubbles with no preferred chirality. Skyrmionic bubbles also share the same behavior as skyrmions in terms of current-induced motion except the fact that they are much slower and seem to be less affected by pinning.

3.D.1 Creation and detection of skyrmions

Controlled nucleation and detection of skyrmions is a prerequisite for their applications in devices. In extended thin films, a fine tuning of the layer thicknesses creates a delicate balance of all the involved magnetic interactions such that the application of magnetic field leads to nucleation of skyrmions at room temperature. This type of skyrmion nucleation has been observed in Pt/Co/AlOx[69], Pt/CoFeB/MgO[64], Ta/FeCoB/TaOx[63]. Confinement effects have also been explored to create and stabilize skyrmions for example by flowing non-uniform currents through geometrical constrictions, micron sized skyrmionic bubbles ($1\mu m$) were formed from stripe domain walls in Ta/FeCoB/TaOx trilayer[63]. In Pt/Co/MgO[65], skyrmion ($130nm$) can be stabilized in the absence of magnetic field by using patterned nanostructures consisting of dots (of size $420nm$). Electric-field-induced writing and deletion of skyrmions was recently demonstrated. It was shown that a switch between a skyrmionic and the ferromagnetic state was possible by application of voltage through the tip of Scannening Tunneling Microscope (STM) for an epitaxial Fe film on Ir(111) at 7.8K[71]. Later on, room temperature nucleation and annihilation of skyrmionic bubbles by electric field was realized in Pt/Co/AlOx[69].

Skyrmions in ultra-thin ferromagnetic films (either single or multilayers) can be imaged using microscopy techniques like Magneto-Optical Kerr Effect (MOKE)[63, 69, 70, 72], Magnetic Force Microscopy (MFM)[73, 74], X-ray Magnetic Circular Dichroism combined with Photo-Emission Electron Microscopy (XMCD-PEEM)[65, 75] and Scanning Transmission X-ray Microscopy (STXM)[38, 64]. Apart from these imaging techniques, skyrmions can be detected by magnetic tunnel junctions which rely on the phenomenon of tunnel magneto-resistance. Further Extraordinary (or Anoma-

lous) Hall-Effect measurements[76, 77] could also indicate the presence and absence of skyrmions.

3.D.2 Current-induced motion of skyrmions

The other important aspect towards skyrmion-based devices is their motion under applied current. Ideally, the skymion motion is supposed to overcome the problem of defects encountered in conventional domain wall motion and even offer higher velocity for lower current densities. Their motion is governed by spin torques. It can be either exerted by (i) Current In-Plane Spin Transfer Torque (CIP-STT) when a spin polarized current flows through the ferromagnet itself or by (ii) vertical spin currents generated by Spin Hall Effect (SHE) or Rashba-Edelstein Effect (Inverse Spin galvanic effect) when a charge current flows in a heavy metal adjacent to the ferromagnet. The distinction between the dominance of these two effects in driving the skyrmion motion is still unclear.

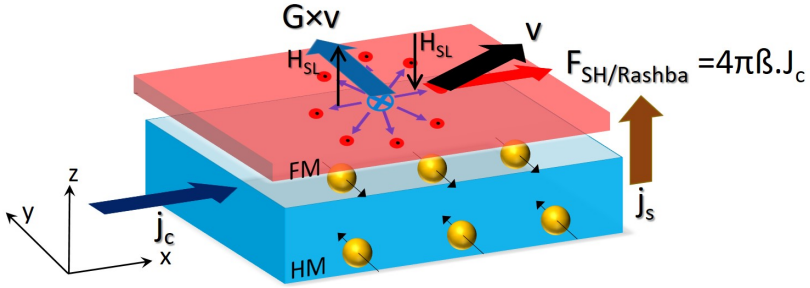

Figure 3.4 – Schematics depicting skyrmion motion under applied current. The charge current j_c in x direction in the heavy metal layer leads to a transverse spin current due to Spin Hall Effect (or and Rashba Effect)(with the spins polarized in +y direction flowing towards the FM layer) An effective Spin hall field H_{SH} acts on the core magnetization of the domain wall on the corresponding edge of the skyrmion. The H_{SH} being opposite at the opposite edges leads to skyrmion motion along the current direction with a velocity v. The Gyrotropic force then acts on this v leading to a transverse deflection of the skyrmion such that the direction of final velocity has both x and y components.

The vertical spin current generated by SHE (or Rashba Effect) has been found to be more efficient in driving the skyrmion both in terms of their velocity and required current density. There are two basic attributes of skyrmion motion. A skyrmion not only moves longitudinally *i.e.* along or against the direction of current but also transverse to it which is a characteristic of its topology as shown in figure 3.4. Thiele equation[78, 79] describes the motion of skyrmion taking these two into account.

$$4\pi\mathcal{B}.j_c + G \times v - \alpha\mathcal{D}.v = 0 \tag{3.8}$$

The first term governs the longitudinal motion of the skyrmion, *i.e.* along the current direction. The tensor $\mathcal{B}$ is the spin torque efficiency of the SHE, j_c is the current density flowing in the HM and given by j_s/θ_{SH}, j_s being the spin current density, and θ_{SH} the Spin Hall Angle (SHA) of that denotes the Spin-Orbit Torque (SOT) efficiency of the HM. The SHE is the HM leads to a spin accumulation at the HM/FM interface and induces a torque on the magnetization. This torque, also known as Slonczewski-like (SL) SOT or damping-like SOT can be represented

as a magnetization-dependent effective magnetic field defined by[80] $\vec{H_{SL}} = H_{SL}(\vec{m} \times (\vec{j_c} \times \vec{z})$ which is in $\pm z$ direction acting on the core magnetization of the DW at the two edges of the skyrmion diameter along the current direction. This leads to its net displacement along or against the current direction. Note that the term $\vec{H_{SL}}$ depends on the magnetization direction (which depends on the chirality and hence the DMI sign) and H_{SL} contains the SHA (θ_{SH}) which is material dependent and can be either positive or negative depending on the HM ; for example positive for Pt[81]. Therefore lets say that with $\theta_{sh} > 0$, the Right-Handed domain walls/skyrmions move along electron flow, whereas the Left-Handed domain walls/skyrmions move along the conventional current direction. In other words, for a given sign of θ_{sh}, both the types (RH and LH) move in the same direction if they have the same chirality, which is fixed by the DMI (more detailed information can be found in the supplementary information of Emori et al.[80]).

The second term is the Gyrotropic force with v the skyrmion drift velocity and $G = (0, 0, -4\pi S)$ being the Gyromagnetic coupling vector, and S the topological charge/skyrmion number defined earlier in equation 3.7. This force, transverse to the skyrmion motion direction, will result in a net deflection of the skyrmion from the trajectory imposed by the SHE (topological Magnus force). Since, the sign of G depends only on the skyrmion core polarity (given by the sign of S), but sign of that force only depends on the skyrmion topological charge. Therefore, skyrmions with opposite topological charge S will be deflected in opposite directions. Therefore, this phenomenon is termed as Skyrmion Hall Effect (SkHE).

In the third term, α is Gilbert damping coefficient, $\mathcal{D}$ is the dissipative tensor. In the case of a skyrmion with rotational symmetry where the skyrmion radius R is much larger than the DW width Δ, it reduces to a scalar $D \propto R/\Delta$[82].

The Skyrmion motion has been explored in several systems. It started with Ta/FeCoB/-TaOx[63, 79] where micron-sized bubbles move due the SOT originating from the SHE in the Ta layer. Their velocities are in the range of 25 µm/s at low current densities of $4 \times 10^8 A/m^2$ suggesting a creep regime, up to 1m/s for higher current density of $6 \times 10^{10} A/m^2$ where they are in the flow regime overcoming the pinning. The observed Skyrmion Hall angle was found to decrease upon the increase of skyrmion diameter. The mean velocities in the case of $[Pt/Co/Ir] \times 20$ were found to be 40 mm/s. Velocities as high as 100 m/s has been achieved for Pt/CoFeB/MgO and Pt/Co/Ta at current densities around $J = 5 \times 10^{11} A/m^2$ up to $J = 2 - 2.5 \times 10^{11} A/m^2$ in the flow regime[64]. For an efficient skyrmion based device it is imperative to ensure high velocity for small (sub-30 nm) skyrmion and minimize the Skyrmion Hall Effect (SkHE). To solve the problem of SkHE and pinning, ferrimagnetic, antiferromagnetic (synthetic or not) skyrmions and antiskyrmions are being investigated.

3.E Other spin textures

3.E.1 Ferrimagnetic skyrmions

In order to overcome the shortcoming of skyrmions in terms of their pinning dominated current driven motion and skyrmion hall effect, ferrimagnetic skyrmions are being explored[83–85] which seem to offer better current driven dynamics. Ferrimagnetic skyrmions are basically antiferro-

magnetically exchange coupled so-called Synthetic Antiferromagnets (SAF) skyrmions having opposite topological charge. They can be realized using either ferrimagnets or ferromagnetic layers with strong antiferromagnetic exchange coupling. The Skyrmion Hall Effect (SkHE) in their case is reduced and in theory suppressed if the net magnetic moment is zero as the Magnus force due to the topological charge is opposite for the two antiferromagnetically couple skyrmions. The longitudinal motion remains unaffected. They are now hence seen to be very promising for applications

3.E.2 Antiskyrmions

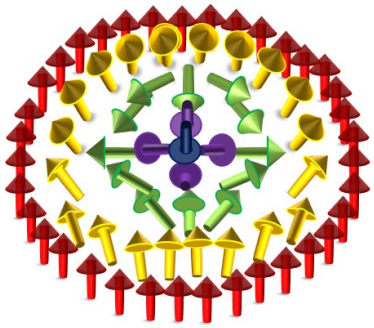

Figure 3.5 – Spin structure of an antiskyrmion

Another type of magnetic structure known as antiskyrmion (shown in figure 3.5) arises when the DMI is anisotropic *i.e.* DMI is of opposite signs along two perpendicular directions. They are composed of boundary walls that alternate between Bloch and Néel type when its boundary is traced. Antiskyrmions like skyrmions can be formed both in bulk systems and thin film multilayers with specific respective crystal symmetries[86, 87]. They also offer suppression of Skyrmion Hall Effect and hence are being currently explored.

3.E.3 Skyrmionium

Skyrmionium is yet another type of magnetic configuration with a ring-like (doughnut) structure shown in figure 3.6. It is often described as being composed of two skyrmions with opposite winding numbers[88, 89]. Its topological charge is S=0 ; therefore it should exhibit a motion without Skyrmion Hall Effect[90, 91]. We observed similar structures in our samples of Ta/FeCoB/TaOx. However their current induced motion or their internal spin structure needs to be investigated for its authenticity.

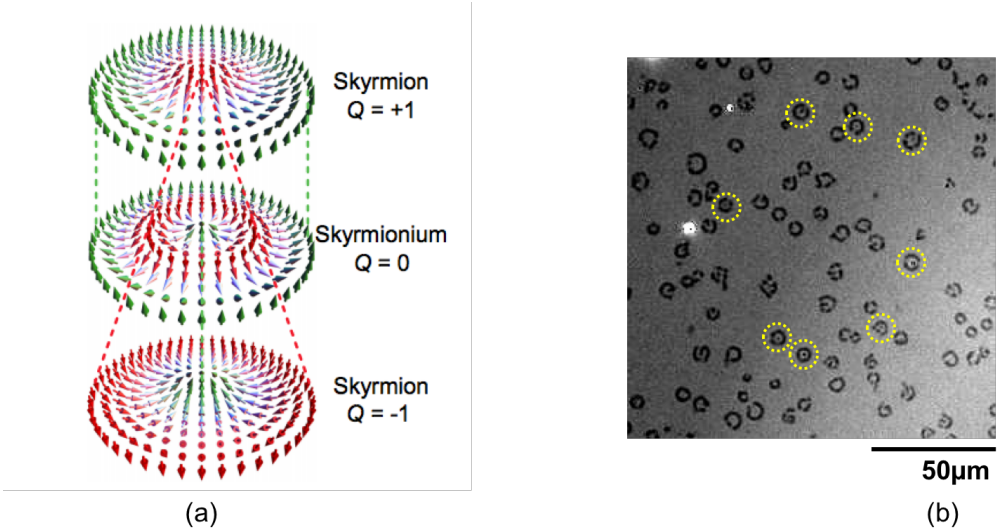

Figure 3.6 – (a) From Zhang et al.[88]: The internal structure of skyrmionium depicted as a coalition of two skyrmions with opposite winding numbers. (b) p-MOKE image of a skymionium-like structure observed in our sample composed of Ta/FeCoB/TaOx.

3.F Why chiral magnetic textures? Envisaged Applications

One of the very famous proposed applications of domains and domain walls is a magnetic racetrack memory[7, 92]. This memory is based on storing the bit-wise information in the domains on a magnetic strip or a 3-D nanowire which therefore offers high storage density. The information can be manipulated by moving the domain walls through applied current via spin transfer torque or even with magnetic field therefore requiring no physical movement unlike the conventional hard disk drive which has to mechanically rotate. Despite these advantages this technique suffers from the requirement of high current densities to write bits and heating effects with high speed. Replacing ordinary domain walls with chiral magnetic structures can help to overcome the present shortcomings.

For example a racetrack memory based on skyrmions, also called **Skyrmion Racetrack Memory**[9, 30, 93], offers many advantages. First, higher integration density can be achieved as skyrmions can be compressed to very small sizes and the internal spacing between the skyrmions can be as low as their diameter. Secondly they are theoretically believed to have faster and flexible current induced motion based on spin orbit torques due to low pinning. Their detection can be similar, like in the case of domain walls, which uses magneto-resistance or other methods solely based on its topological properties. Having said that, experimentally this application is facing a lot of challenges in terms of reducing the skyrmion size and getting rid of pinning and Skyrmion Hall Effect (SkHE) associated with the motion. Therefore antiskyrmions and antiferromagnetically exchange-coupled skyrmions with opposite topological charge are being investigated too for this application as they are expected to solve the aforementioned issues[94].

Besides the application in memory devices, chiral magnetic textures can also be employed to carry bit-wise logic operations. This is based on utilizing their solitonic or particle like properties.

It can be realized through creation and annihilation of skyrmions. Recently skyrmion based AND and OR logic gates have been proposed opening a new a paradigm of skyrmion utility[95]. Several other applications are also budding, like **Skyrmion-based Microwave Detectors**[96] based on their breathing modes[97], **Skyrmion Spin Torque Oscillators**[98]**, Skyrmion-based Synaptic**[99] **or Artificial Neuron Devices and Skyrmion-based Neuromorphic Computing**[100]. In order to realize these applications it is imperative to optimize the skyrmions in terms of their size and enable their dynamic manipulation for the desired applications.

3.G Conclusion

In this chapter we have seen the different chiral magnetic textures that could exist in thin film trilayer systems consisting of heavy metal, ferromagnet and insulator and their envisaged applications. We saw how DMI plays an important role in stabilizing these textures specially skyrmions. We also went through some of the recent methods engaged in creation, detection and observation of skyrmions. A prerequisite for their application in devices is their effective tuning. It is challenging to obtain stable skyrmions and manipulate them as needed. Therefore the next chapter addresses the static and dynamic manipulation of magnetic properties in thin films which in fact is manifested as a change in the properties of skyrmions.

4

Manipulation of interfacial magnetic properties

4.A Introduction

The previous chapters highlighted the intricacies of magnetism at interfaces and how it steers the formation of chiral magnetic structures leading to a new paradigm of spin-based application, more specifically for memory and logic operations. Control of interfacial magnetism is a prerequisite to effectuate the desired applications. It would serve as a mean to design a model system as well as to tune it to suit further needs. In this chapter, we discuss how the interfacial magnetic properties like magnetic anisotropy and DMI can be modulated which involves appropriate choice of materials and their respective thicknesses, interface quality, temperature-dependence and applied voltages. Some of the latest achievements in this area made by several groups are also listed.

4.B Modification of Magnetic Anisotropy

Concentrating mainly on the thin film systems, we know that the effective magnetic anisotropy has both surface and volume contributions. The surface contribution mainly comes from the interface anisotropy and the volume contribution can be magneto-crystalline and magnetostatic/dipolar/shape anisotropy. For ultrathin films, the magneto-crystalline anisotropy is usually very small. Some methods to maneuver the effective magnetic anisotropy is described below.

4.B.1 Variation of Thickness and Composition of Ferromagnet

It is now well known that the effective anisotropy becomes a function of thickness for thin ferromagnetic films. As already explained in chapter 2, the surface anisotropy starts dominating the shape anisotropy for lower film thicknesses [101]. Therefore the volume and the surface contribution to the effective anisotropy can be tuned by adjusting the thickness of the ferromagnetic layer [19, 102]. Figure 4.1 shows the variation of the effective anisotropy as a function of thickness.

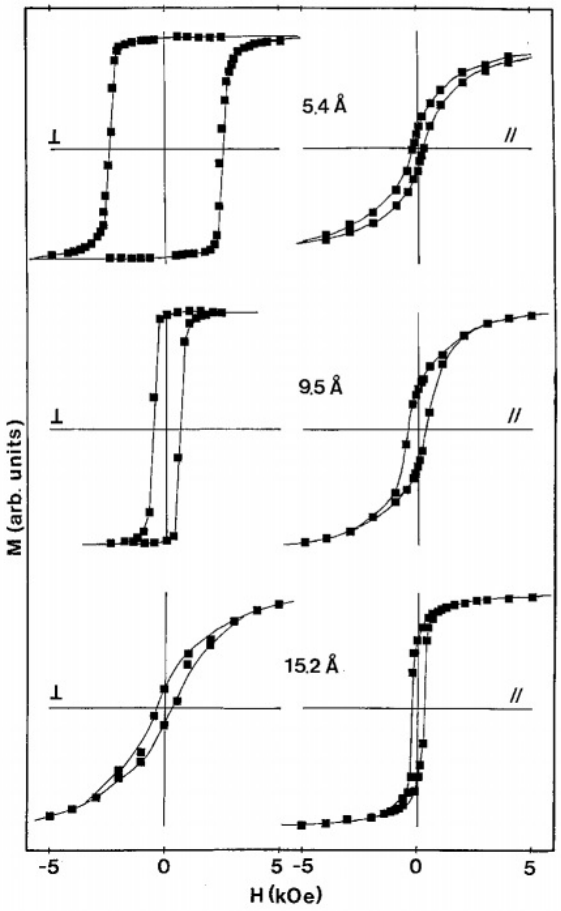

Figure 4.1 – From Bruno and Renard [19]: Hysteresis loop with applied magnetic field H perpendicular and parallel to the film plane for Au/Co/Au sandwiches with Co thickness t = 5.4 Å, 9.5 Åand 15.2 Å, at T=10K

The magnetic anisotropy depends also on the composition of the ferromagnetic layer. For example the magnetic anisotropy of FeCoB layer is a function of the percentage of Fe and Co [103, 104] as depicted in figure 4.2. This can be ascribed to the location of the 3d states of Fe or Co in relation to the 2p orbitals of the oxygen ions in the first magnesium oxide layer which governs the overall contribution to the interfacial anisotropy.

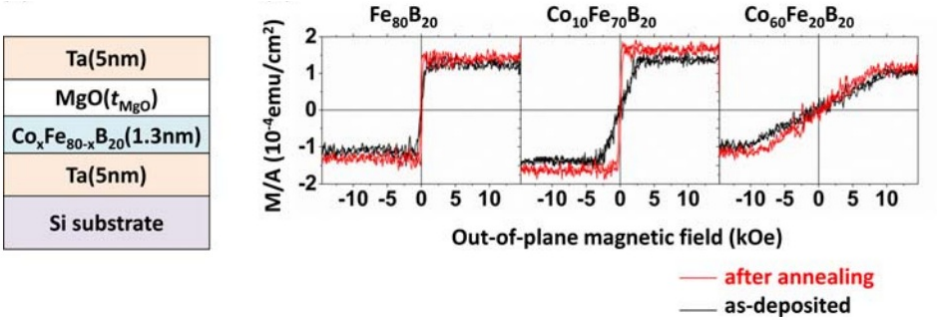

Figure 4.2 – From D. D Lam and Suzuki : Schematic view of sample stacking structures (left) Magnetization curves of samples with 1.0 nm MgO overlayer for the three alloys (black curves: as-deposited, red curves: annealed at 300° C).The saturation field increases with increasing the Co concentration.

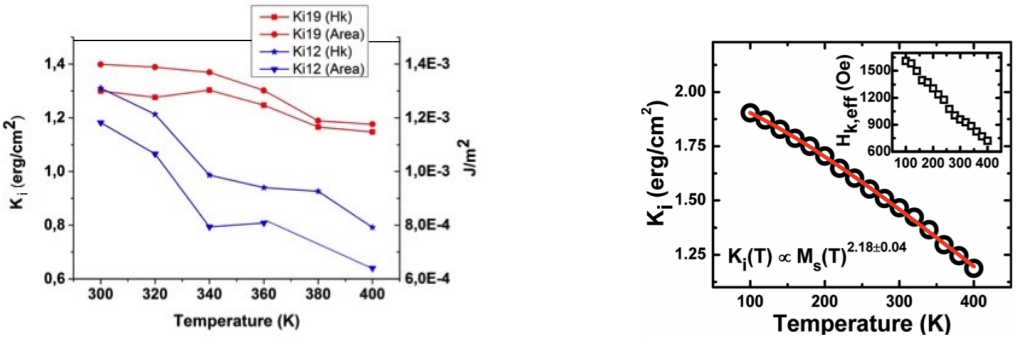

Figure 4.3 – Plot of the variation of interface anisotropy coefficient K_i calculated for two different thicknesses (1.2nm and 1.9nm) of ferromagnet (FeCoB) as a function of temperature obtained experimentally during my master thesis (left graph), A similar plot obtained by Alzate et al. [105] (right graph)

4.B.2 Temperature

The role of temperature is extremely important in the case of ultra-thin ferromagnetic films. If the ferromagnetic thickness is too small, the thermal energy at room temperature can itself lead to its stochastic switching. In fact the magnetization switching from one easy direction to the other due to thermal excitation is given by the Néel-Arrhénius law :

$$\tau = \tau_0 \exp \frac{K_{eff}.V}{k_B.T} \tag{4.1}$$

where τ is the relaxation time, τ_0 is a typical time of 10^{-9}-10^{-10} s , k_B is the Boltzmann constant and T the temperature. We can therefore infer that if the effective anisotropy is low the effect of temperature starts dominating, which is often the case at different transition thicknesses of ferromagnet : (i) ferromagnet to paramagnet in the order of few angstroms or (ii) out-of-plane to in-plane anisotropy in the range of 1-2 nm. In fact, thermal excitation leads to the formation of spontaneous thermally demagnetized domain structures observed in many HM/FM/MOx trilayer systems like Ta/FeCoB/TaOx, Pt/Co/MgO or Pt/Co/AlOx at room temperature. Since the temperature facilitates in jumping over the energy barrier between different magnetization states, it can both work in favor or against magnetization textures,

specially skyrmions. A slight change of temperature can affect them largely. In figure4.3 is an example comparing the variation of interface anisotropy coefficient as a function of temperature obtained during my masters thesis.

4.B.3 Electric Field

Electric field has emerged to be one of the most important tools to play with interfacial magnetism[106, 107]. It offers both position specific and dynamic control of magnetism at interfaces. It was first demonstrated for Fe/Pt and Fe/Pd films using an electrolytic cell[108]. Owing to the ion accumulation and depletion at the ferromagnet interface due to the electrolyte on the application of voltage, a reversible modification of magnetic anisotropy was displayed. This phenomenon then opened a new field of research in terms of controlling the interfacial magnetic properties through voltage.

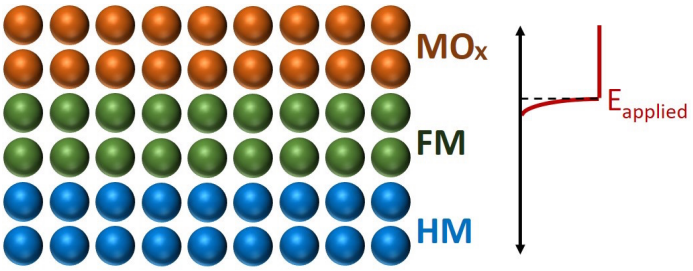

Figure 4.4 – Schematic view of applied electric field across a heavy metal(HM) /ferromagnet(FM) /metal oxide(MOx) system. Due to the screening effect of the electric field in metals, it mainly acts on the FM/MOx interface and does not penetrate the FM/HM interface

Generally when a voltage is applied across a typical HM/FM/MOx trilayer, depending on its sign, it leads to either accumulation or depletion of electrons at the FM/MOx interface. This is only confined to the FM/MOx interface due to the fact that the electric field owing to screening effect in a metal can only penetrate ~ 0.2 into the ferromagnetic film and therefore is negligible beyond it as shown in figure 4.4. The accumulation or depletion of electrons at this interface leads to a change in electronic occupation of orbitals and hence hybridization in the ferromagnetic layer. A simple picture is described in figure 4.5. Since the interfacial magnetic anisotropy is directly a result of complex band hybridization at the interface, it can be directly altered by applied voltage. There can be several mechanisms associated to this electric field effect. A rapid charge redistribution described above occurs on a short time scale ranging from the order of nano seconds to few seconds. Another mechanism could be migration of ions (usually oxygen ions) under applied voltage from the metal oxide to the MOx/FM interface. It could superimpose with the previous mechanism to produce larger changes. Ion-migration has been known to result in larger electric field efficiency (equals to a change of a magnetic parameter per voltage applied per unit thickness) defined by[109] defined by

$$\beta_{Ks} = \frac{\Delta K_s}{V} t_{FM} \tag{4.2}$$

This phenomena however occurs at longer time scales and can range from few minutes to

several hours. Both these mechanisms can lead to the change in the effective anisotropy of the ferromagnetic film facilitating magnetization switching.

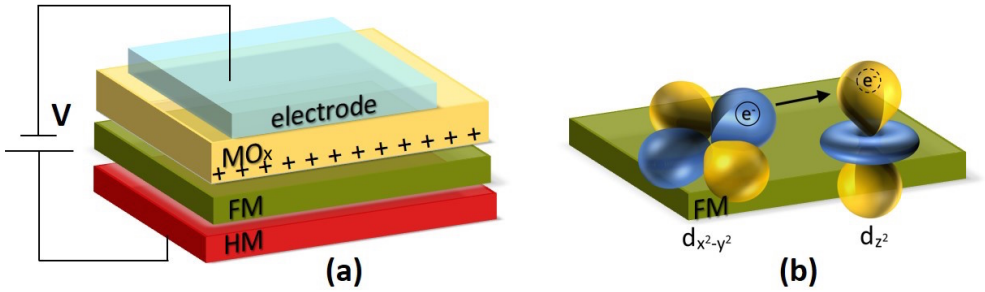

Figure 4.5 – (a) Schematic view of sample stack under applied voltage indicating depletion of electrons at the MOx/FM interface for negative voltage. (b) The rearrangement of electrons in the d-orbitals of the FM layer due the effect of the applied voltage.

Electric field has been found to also change the saturation magnetization and hence the Curie temperature in the case of extremely thin ferromagnetic films (0.4-0.8 nm). This happens typically when the FM thickness is close to transition between ferromagnetic and paramagnetic regimes. For thicknesses in these ranges, all the interfacial magnetic properties become prominent as compared to bulk systems and hence are sensitive to applied voltages. Establishing interfacial control of properties via electric field enables magnetization switching process which is crucial from technological point of view.

Below are few examples of studies done on the application of electric fields to manipulate effective anisotropy for different applications. Y Shiota et al. in 2009 used Au/bcc-Fe80Co20/MgO/polyimide/ITO (grown epitaxially) junctions with perpendicular magnetic anisotropy and realized voltage-induced magnetization switching under an applied magnetic field at room temperature.[110] They saw that the easy axis of magnetization could be manipulated with an applied electric field. It got rotated from in plane to perpendicular as the voltage applied was changed from +200V to -200V. Later in 2010 they realized this effect in a magnetic tunnel junction (MTJ) structure consisting of FeCo/MgO/Fe with Fe layer having in-plane anisotropy and FeCo having out-of-plane anisotropy[111].

In 2010 Endo et al. demonstrated the effect of electric field on MgO/$Co_{40}Fe_{40}B_{20}$ (wedge)/Ta structures.[112] They observed the changes in anisotropy and coercivity using transport measurements. They calculated the change in magnetic anisotropy energy per unit volume as a function of applied electric field which is shown in Fig.4.7.

Some remarkable achievements have been made to control magnetic skyrmions in Ir/Fe structures by electric field. Recently it was shown that electric field can be used to write and delete skyrmions *i.e.* switch between a skyrmion state and a uniformly magnetized state at low temperature (7.8K) and under large applied magnetic fields (in the order of T) using Spin Polarized-Scanneling Tunneling Microscopy (SP-STM) tip[71] shown in figure 4.8(a). Writing and deletion by voltage was mainly attributed to changes in anisotropy and exchange parameter. Magnetic skyrmions are hence seen to be directly controlled by applied voltages paving the way towards their utilization in memory and logic devices. Electric field switching of skyrmionic

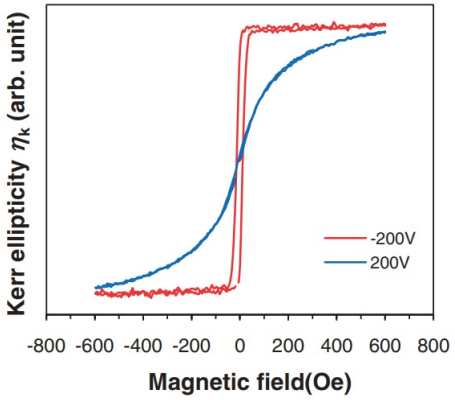

Figure 4.6 – From Shiota et al. [110]: Magnetic hysteresis curves under out of plane magnetic field, of a 0.58-nm-thick Fe_80Co_20 layer, measured under positive (blue) and negative (red) bias voltage applications.

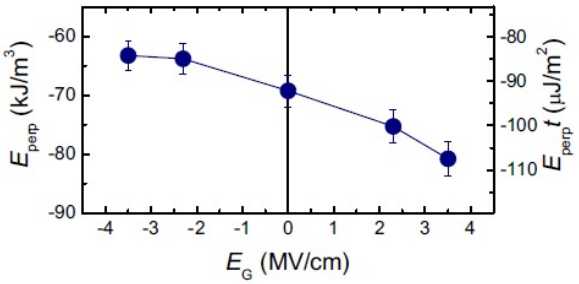

Figure 4.7 – From reference Endo et al. [112]: The electric field E_G dependence of magnetic anisotropy energy for MgO/CoFeB/Ta structures with t_{CoFeB}=1.33 nm. Left vertical axis is for per volume E_{perp} and right is for per sheet area $E_{perp}t$.

bubbles was also demonstrated in Pt/Co/AlOx[69] (figure 4.8(b)) systems at room temperature during the thesis of Marine Schott in joint collaboration between Institute Néel and Spintec. Here the electric field was applied via patterned electrodes on the sample and it was probed by Magneto-optic Kerr Effect (MOKE) microscope. This study also relies on the electric field manipulation of interface magnetic anisotropy and magnetization. Although it was speculated that a change of interfacial DMI could be probable but it could not be made evident. Extracting DMI from MOKE experiments is in fact cumbersome owing to large error bars involved with multiple parameters that need to be determined for calculations.

4.C Modification of Dzyaloshinskii-Moriya Interaction

We have witnessed in the previous chapters how the antisymmetric exchange interaction called DMI provides the framework for the existence of chiral magnetic textures and also novel spin-orbitronic phenomena leading to fast current-induced domain wall motion. We recall that in the case of thin film systems, the origin of DMI not only lies at the heavy metal/ferromagnet interface (Fert-Levy type DMI) but can also stem from ferromagnet/metal oxide interface (Rashba-type DMI). The Rashba type contribution to DMI was only theoretically predicted

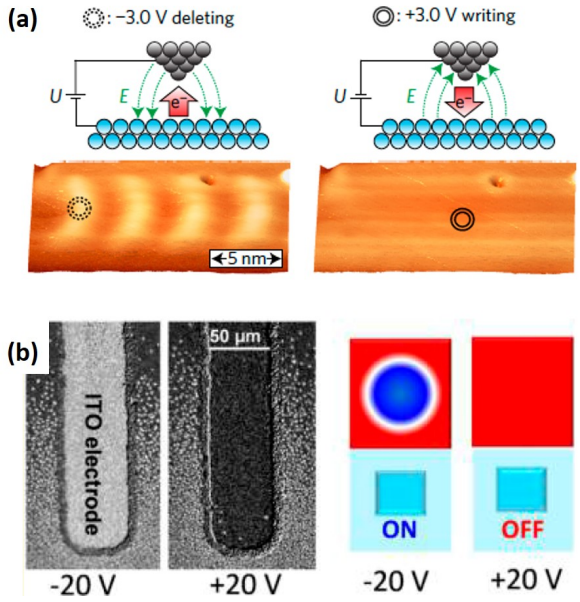

Figure 4.8 – (a) From Hsu et al. [71]: Writing and deletion of individual magnetic skyrmions by Spin-Polarized Scanneling Tunneling Microscopy tip (Cr bulk tip) at low temperatures (7.8K) in Ir/Fe bilayer. Perspective views of subsequent SPâSTM constant-current images of the same Fe triple layer area ($V_{applied}$ = +0.3 V, I = 0.5 nA, B=+2.5 T). The voltage ramps up to $V_{applied}$ = -3 V (+3 V) between the images have been performed at the positions of the dashed (solid) circles, which reproducibly result in deleting (writing) of an individual magnetic skyrmion. (b) From Schott et al. [69]: Electric field induced switching of skyrmionic bubbles at room temperature in Pt/Co/AlOx structures (left): The p-MOKE image of electrode under applied voltage. At -20V the skyrmion density is large whereas almost all the skyrmions disappear at +20V. (right) Schematic representation of the behavior of skyrmions under applied voltage. The electric field acts like a switch, leading to the nucleation and annihilation of skyrmions.

before the beginning of my thesis and an experimental demonstration was never made (this forms one of the major topics of my PhD thesis and is presented in chapter 8).

From a broader perspective, DMI is largely dependent on the relative position of the electronic states of the respective interfaces for example 3d states of FM and 5d states of heavy metal [113] or 3d states of FM and 2p states of oxygen ions in MOx. Static or dynamic DMI engineering at these interfaces can facilitate the tuning of the chiral magnetic textures as well as current-induced domain wall motion for various applications like memory or logic devices. Several approaches have been made to tune the overall DMI in thin film systems.

4.C.1 Multilayer Stacking

One of the ways to enhance DMI is to stack different HM or MOx layers on either side of the FM such that there is an additive effect at each interface making the overall DMI quite strong. For example the sign of the DMIs for Co/Ir and Co/Pt are opposite. On reversing the stack direction *i.e.* Ir/Co gives the same sign of DMI as Co/Pt, therefore a multilayer structure like Ir/Co/Pt has a DMI greater than both Ir/Pt and Co/Pt. Similarly, multilayer stacks like Ir/Fe/Co/Pt are predicted to possess an even higher DMI than Ir/Co/Pt, due to the fact that Ir/Fe gives

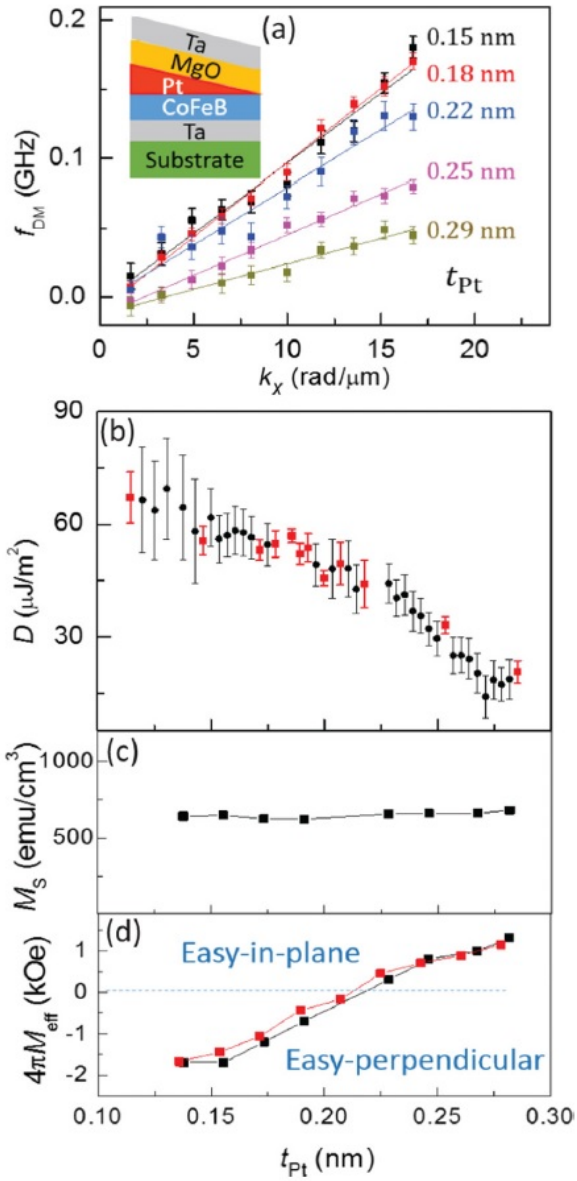

Figure 4.9 – From Ma et al.[114]: Variation of DMI coefficient, M_s, and effective anisotropy as a function of Pt thickness in Ta/FeCoB/Pt/MgO.(a) The obtained linear dependences of f_{DM} (=f_S-f_{AS} explained in the Brillouin Light Spectroscopy section in chapter 5) as a function of k_x for different thicknesses of Pt along with the multilayer structure shown in the inset. The solid lines show the least-squares fits. (b) The interfacial DMI constant D as a function of the Pt layer thickness t_{Pt} derived from the previous plot. The red squares are derived from the linear fits on the k_x dependences of f_{DM} with different t_{Pt}. The black circles are obtained through f_{DM}/k_x at fixed k_x = 16.7 rad/μ m by varying t_{Pt} in a smaller step size. (c)M_S and (d) $4\pi M_{eff}$ as functions of t_{Pt}. The red (black) dots in (d) are obtained from the field dependence BLS (VSM) measurements, respectively.

a higher DMI coefficient than Ir/Co[36, 37]. It was also shown in case of Ta/FeCoB/Pt/MgO heterostructures that the DMI varies linearly as function of the Pt thickness where the DMI contribution comes from both Ta/FeCoB and FeCoB/Pt interafces shown in figure 4.9[114]. This highlights the importance of the two HM layers being channelized to increase the DMI and

decrease the anisotropy to further assist in skyrmion nucleation. Moreover repetitive stacking of $HM_1/FM/HM_2$ can further lead to increased thermal stability of the chiral structures such as skyrmions formed in this system due to large magnetic volume and their dipolar coupling across the successive layers[38]. Theses cases mainly pertain to Fert-Levy DMI[24] mechanism. DMI can also be enhanced by adding oxides on top of HM/FM bilayer, for example Pt/Co/MgO[65]. Here the DMI at Co/MgO interface comes from Rashba effect[27].

4.C.2 Irradiation and Oxygen Adsorption

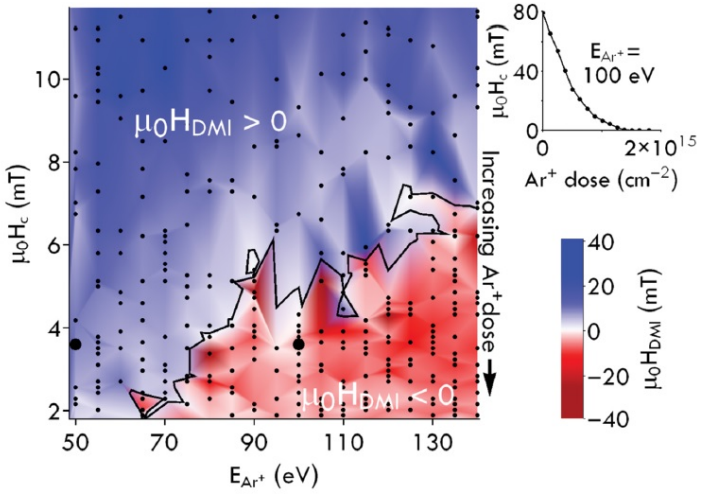

Figure 4.10 – From Balk et al.[115]: A surface plot of $\mu_0 H_{DMI}$ showing variation as a function of $\mu_0 H_c$ and E_{Ar+} with Ar+ dose increasing towards the bottom of the surface plot. Inset:$\mu_0 H_c$ decreases monotonically with Ar+ dose for a sample with E_{Ar+} = 100 eV.

It has been shown recently that DMI can be spatially tuned in HM1/FM/HM2 structures using Ar^+ irradiation technique. For example in the case of Pt/Co/Pt[115] with perpendicular magnetic anisotropy (PMA), this DMI change due to irradiation has been mainly attributed to the increased disorder between the top Co/Pt interface. Also, it is shown that ion-induced interfacial disorder, and reduction of the thickness of the top Pt layer, decrease coercivity and hence the magnetic anisotropy. Considering the DMI, since Pt/Co/Pt is a symmetric structure, in ideal growth conditions it should exhibit a zero effective DMI due the cancellation of the individual DMI contributions being equal and opposite. However, irradiation modifies the top interface, reducing the thickness of top Pt and eventually resulting in Co oxidation, hence leading to the emergence of an effective DMI. It can also eventually result in the inversion of the sign of effective DMI (figure 4.10) which is attributed to top Pt layer removal. Such spatial DMI control could be very promising for designing novel spintronic devices.

Another study in this area shows captivating ideas. It has been shown theoretically that surface oxidation can greatly impact DMI in the case of FM/HM bilayers (*e.g.* Fe/Ir)[116]. It has been shown that for an oxygen coverage of 0.5 monolayer, the DMI exhibits a peak stabilizing chiral magnetic ground state. Further it has also been suggested that the sign and the strength of the DMI is highly dependent on the charge transfer and hybridization between 2p oxygen and 3d-FM, 5d-HM states around Fermi level. It is not only limited to the effect of oxygen

adsorption but can be extended to other electronegative ions (C,N,F) which produce the same effect. As electric field can actively manipulate the oxygen ion concentration at the interface, this work further paves the way towards electrically controlled interfacial DMI which will be discussed next.

4.C.3 Electric Field

Electric Field application to modify magnetic properties has been a very popular field of research over the last few years. Owing to the fact that it is power saving and can offer both spatial and temporal manipulation of magnetic properties, its applications in Voltage Controlled Magnetic Anisotropy (VCMA)- Perpendicular Magnetic Tunnel Junctions (MTJs) has been long proposed as described in the earlier sections. However its implications on DMI until now has not been made very clear. Theoretical predictions have estimated the electric field efficiency (=change in DMI energy/voltage applied per unit thickness) defined by equation:

$$\beta_{DMI} = \frac{\Delta D}{V} t_{FM} \tag{4.3}$$

It is expected to be in the order of β_{DMI}=26 fJ/Vm[43]. Although a very small voltage-induced variation of DMI in thick FM films (20 nm) consisting of epitaxial Au/Fe/MgO by Nawaoka et al[117] was reported, DMI variation with voltage in ultra-thin films has not been addressed yet. The major goal and results of my thesis are oriented towards this idea. The aim is to establish DMI control via applied electric field and further analyze its implications on magnetic skyrmions. This is elaborated in detail in the experimental chapters, primarily chapter 8.

4.D Conclusion

Finally we see that the interfacial magnetic properties can be altered by various means. It is rather fascinating to employ one or several methods together to achieve the results required for targeted applications. The chapters based on the experiments and results of my thesis deal with several aspects of modifying the interfacial magnetic properties based on some of the techniques described above in this chapter. More specifically we expect that the electric field manipulation of DMI forms one of the important aspects of dynamically controlling magnetic skyrmions. Since there is a lack of experimental demonstrations in this regard, we work towards it as will be seen in the following chapters.

Part II

Methods and Characterization techniques

5

Sample Preparation and Characterization techniques

5.A Introduction

In this chapter, the sample fabrication, patterning and characterization techniques are explained. The steps involved to prepare the samples for experiments under applied voltage are described. It includes deposition of insulator (oxides) followed by transparent electrode and its patterning. Further characterization techniques like MOKE magnetometery and microscopy, BLS and VSM are detailed.

I have highlighted the procedures I have carried out myself as well as the ones that were done in collaboration with research scientists from different labs.

5.B Sample Deposition

The thin film deposition in our case is carried out by DC magnetron sputtering. It is based on physical vapor deposition technique in which the material that has to be deposited, is bombarded with ionized gas molecules forming a plasma which then condenses on the substrate. The deposition is carried out in a chamber under vacuum in order to obtain pure quality of the deposited materials (typically in the range of 10^{-6} to 10^{-9} mbar, depending on the performance of the tool). The plasma is created by using an inert gas which is argon (Ar) in our case. The

target material i.e the material to be deposited is positioned at the cathode while the substrate is at the anode. An electric potential when applied leads to a discharge which ionizes the Ar atoms. The Ar+ ions then accelerate towards the target and eject out the target atoms. This occurs when the kinetic energy of the Ar+ ions overcomes the binding energy of the target atoms. The ejected target atoms are driven towards the anode and hence get deposited on the substrate In magnetron sputtering, a magnet is installed at the cathode. The magnetic field generated, modifies the trajectory of the electrons above the cathode leading to an increased number of collisions with the Ar atoms and therefore increased number of Ar+ ions. This leads to an increase in the deposition rate.

We use Actemium machine which possesses 12 targets which allows us to develop complex stacks involving a wide range of materials. The whole deposition process is automated. The actemium tool is also equipped with a treatment chamber in which oxidation and etching steps takes place. The deposited thicknesses are determined by the opening time of the shutter that covers the target. Deposition rates can be modulated by adjusting the current set point by varying the power applied to the cathode. The Ar pressure in the chamber also influences the deposition rate. In our system, it is set to 2.10-3 mbar. The rates basically ranges between 0.03 nm/s and 0.2 nm/s, making it possible to deposit layers as thin as a few tenths of nanometer. Caliberation of the thicknesses is done by X-rays reflectivity.

We used Si/SiO_2 as a substrate. For obtaining a constant thickness of a magnetic/nonmagnetic layer, an on axis deposition is carried. On-axis refers to the case when the depositions are carried out with the target and substrate perfectly aligned with respect to their centers. The thickness of deposited material obtained using on-axis deposition might however vary by 2-5% on the edges of the substrate. Also when the thicknesses deposited need to be very small i.e in the order of few angstroms, the opening/closing time of the shutter/chamber covering the target becomes extremely crucial. Even a slight variation in this impacts the thickness of the material deposited. It sometimes therefore leads to the problem of reproducibility for the same nominal thickness of the material.

For example, the stability of magnetic textures like skyrmions is very sensitive to small variations of interfacial magnetic properties which are directly dependent on the thickness of the ferromagnet. Therefore on-axis deposition can be cumbersome to reproducibly obtain the exact thickness necessary for stable skyrmion region. Therefore a gradient of the thickness of the ferromagnet is favorable to obtain a region where skyrmion are stable. With our deposition machine Actemium, it is possible to create thickness gradients by shifting the substrate laterally from the target which is called an off-axis position. Off-axis deposition leads to a gradient of thickness of the target material being deposited on the substrate which we often call wedge. The two types of deposition positions are represented in figure 5.1.

To overcome the problem of reproducibility of thicknesses with on-axis deposition specially for skyrmion zones, we deposit heavy metal/ferromagnet/metal oxide system using off-axis deposition to produce double wedges, i.e a wedge of the ferromagnet followed by wedge of top oxide perpendicular to it(5.2). This gives a broader range of the variation in magnetic properties which helps in locating the skyrmion zone on the same sample.

Deposition of wedges allows studying the magnetic properties as a function of the ferromagnetic layer thickness and the insulator layer thickness. Using off-axis deposition technique, one of the layers (ferromagnet) is first deposited as wedge along one axis (let us say x), then

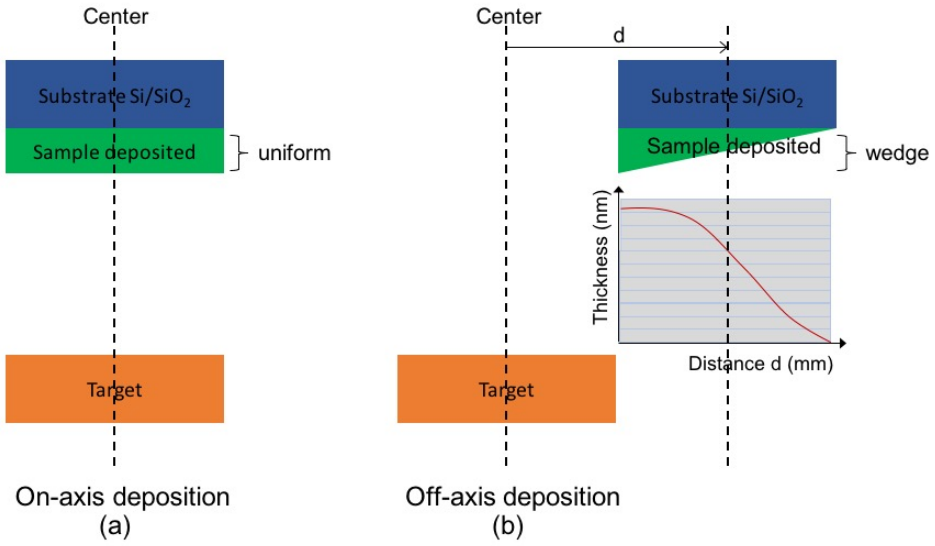

Figure 5.1 – On-axis(a) and Off-axis(b) depositions by sputtering. The off-axis deposition involves lateral translation of the substrate from the center of the target to allow target deposition as a thickness gradient.

another layer of a different material (metal) can also be deposited as a wedge perpendicular to it (let us say y) demonstrated in figure 5.2. It is usually followed by an oxidation step to obtain metal oxide on the top.

As mentioned earlier, the Actemium machine is equipped with a treatment chamber in which oxidation steps can be performed. For natural oxidation, exposure to an oxygen atmosphere for a given time in the treatment chamber is carried out.Different oxygen pressures can be used. The option of plasma oxidation is also available, where an oxygen plasma is utilized to oxidize a metallic element. This technique is more commonly applied to alumina barriers. Also due to the presence of a second wedge of metal layer which is followed by oxidation, we get an oxidation gradient along this layer. This gives access to different combination of the thickness of the two layers and the oxidation state of the ferromagnet/metal oxide interface, which enables us to study the magnetic properties in greater detail. For example the PMA is affected both by the ferromagnetic layer thickness and also the oxidation state of the adjacent non-magnetic material. These two parameters can be simultaneously investigated by means of double wedges. For example, in order to deposit double wedged sample consisting of Ta/FeCoB/TaOx on Si/SiOx 100 mm wafer, first a uniform layer of bottom Ta is deposited. Following this step, off axis deposition of FeCoB forms a wedge in x-direction, a wedge of Ta is then deposited in the y-direction followed by in-situ natural oxidation. Depending on the different samples, sometimes a capping layer (in the order of 0.5-1 nm) is deposited wither of Al or Pt to protect the sample from degradation.

All the sample depositions were carried out by Stéphane Auffret at Plate-forme Technologique Amont (PTA) located at Spintec/CEA.

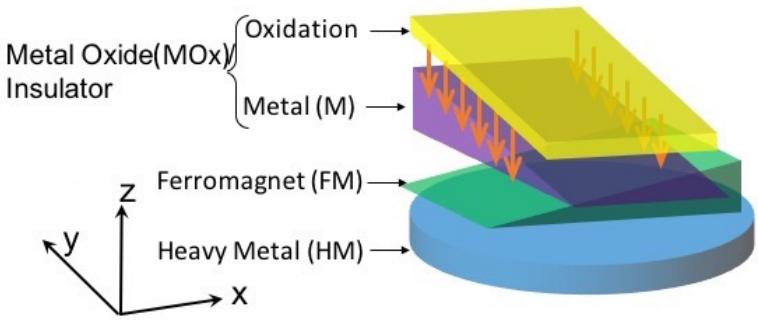

Figure 5.2 – Schematics of a sample consisting of double wedge: a wedge of ferromagnet along x and of the top metal along y direction which is later oxidized creating an oxidation gradient along this axis.

5.C Preparing the samples for examination under electric field

In order to perform measurements like Magneto-Optic Kerr Effect Microscopy or Brillouin Light Spectroscopy under applied electric field, the samples need to be specially prepared. These two techniques employing visible light require large sample areas where electric field can be applied (optical aberration + width of the electrical contact to be made for the application of electric field is in the order of μm) and transparent electrode in order to be able to access the magnetic sample. To apply an electric field, negligible passage of current has to be ensured across the HM/FM/MOx system. For this a thick insulator (usually an oxide) is deposited followed by deposition and patterning of transparent electrode.

5.C.1 Depositing insulating layer of HfOx by Atomic Layer Deposition (ALD)

The first step required to prepare the samples is deposition of thick dielectric or insulating oxide which acts as a barrier and prevents passage of current across the trilayer sample under an applied voltage. Indeed sputtering generally does not allow a 1 nm oxide layer to be free from pinholes over 100μm lateral sizes making this deposition of a thick dielectric necessary. This also prevents any heating of the sample and hence suppresses any temperature induced effects. For our samples consisting of Ta/FeCoB/TaOx, a bilayer of AlOx and HfOx was deposited by Atomic Layer Deposition (ALD) at Institut Néel. ALD is a layer by layer deposition technique for producing thin films of different materials from their vapor phase. It is based on sequential and self limiting reactions and offers precise control of thickness in the order of angstroms. In ALD the precursors are sequentially introduced in the in the reaction chamber. An ALD cycle is a single exposure to the precursors to be deposited and the amount of material deposited depends on the precursor-surface affinity. The number of cycles varied can determine therefore the total thickness of the material deposited. Deposition is carried out at usually temperatures below 350°C. In our case the cycles were carried out at 100°C, to prevent any further annealing of our Ta/FeCoB/TaOx which were previously annealed at 225°C.

The depositions of insulating oxides were carried out at Institut Néel by Marine Schott and other colleagues. I participated in the experiments.

5.C.2 Microfabricating Indium Tin Oxide (ITO) electrodes using UV- Lithography

In order to observe the changes in magnetic domain structures under applied electric field, we need to use transparent electrodes. ITO is one such material facilitating these observations. After the deposition of oxide by ALD, and obtaining the mask pattern on the resin coated on the sample by UV lithography and its development, ITO was deposited on our samples by dc sputtering. The material adheres to the sample in areas where there the resin is absent (figure 5.4(i)). The next step is lift-off.

UV-lithography for patterning

In order to draw micro or nano patterns on the sample for the desired characterization technique, photolithography or UV lithography is used. Basically a design consisting of geometrical patterns of required sizes is drawn on a mask. The sample when in contact with the mask gets selectively exposed to the UV light. The mask design is hence transfered to the sample in the form of either the exposed or the non exposed zones which depends on the type of resist.

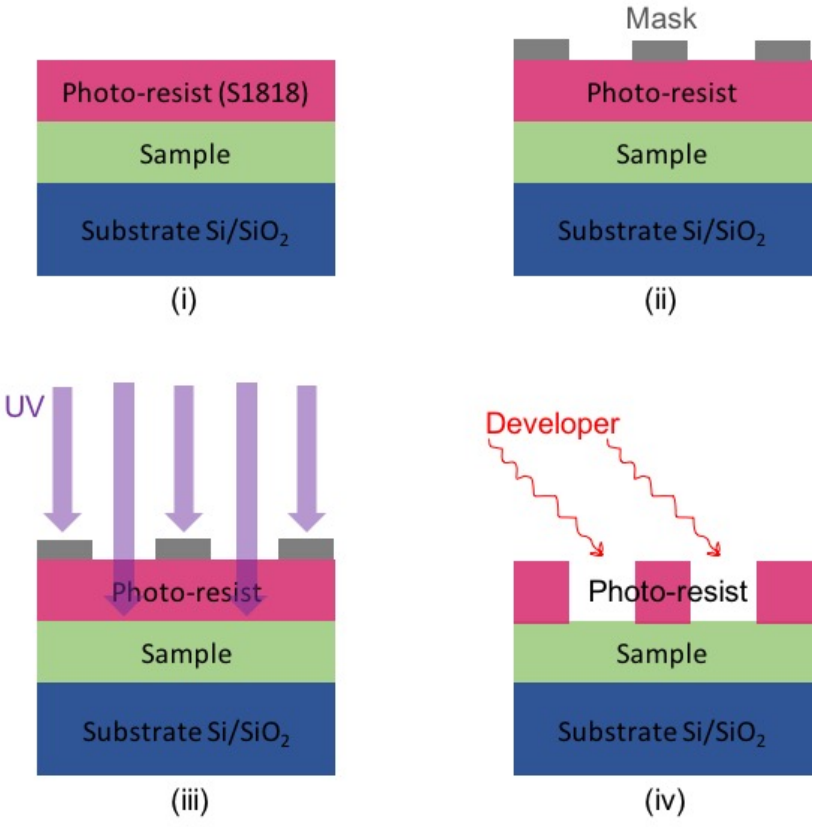

Figure 5.3 – Steps of microfabrication: (i) Deposition of resist on the sample by Spin coating. (ii) Placement of a mask to transfer a geometrical pattern on the sample. (iii) Exposure to UV rays using MJB3 UV lithography setup. (iv) Development of the sample then leads to the dissolution of the exposed resist if the resist used is positive.

In order to pattern ITO electrodes typically of sizes $100 \times 800\mu m^2$ on the sample, it is

first coated with a resist (figure 5.3(i)) using a spin coater which is based on the principle of centrifugation. The resist can be positive or negative. A positive (negative) resist is the one which on exposure to light dissolves (stays) on development. In fact light induces a change in chemical properties of the resist(breaks polymer chain), such that the exposed areas are then sensitive to the solution used for development (figure 5.3(iii)). In our case we use a standard positive resist Shipley S1818. After coating the sample with the resist, it is then annealed at 115°C for one minute in order to eliminate the solvent still present. For the exposure, deep UV lithography (MJB3) was used at Nanofabrication lab at Institut Néel. The mask is aligned with respect to the sample to expose to UV only certain areas of the sample coated with resist in order to transfer the pattern required (figure 5.3(ii)). According to the power of the device and the type of mask used (plastic or glass), the times of exposure could differ.

The development stage then consists of immersing the sample consisting of the exposed resist in the solution used as a developer for 1 minute. The exposed resist dissolves and leads to the appearance of the desired geometry in the form of the non-exposed resist (figure 5.3(iv)). It is then rinsed with water for 1 minute.

Deposition of ITO electrode

After getting the sample consisting of a pattern of resist on the sample, an ITO deposition is carried out. DC magnetron sputtering is used to deposit 30 nm of ITO.

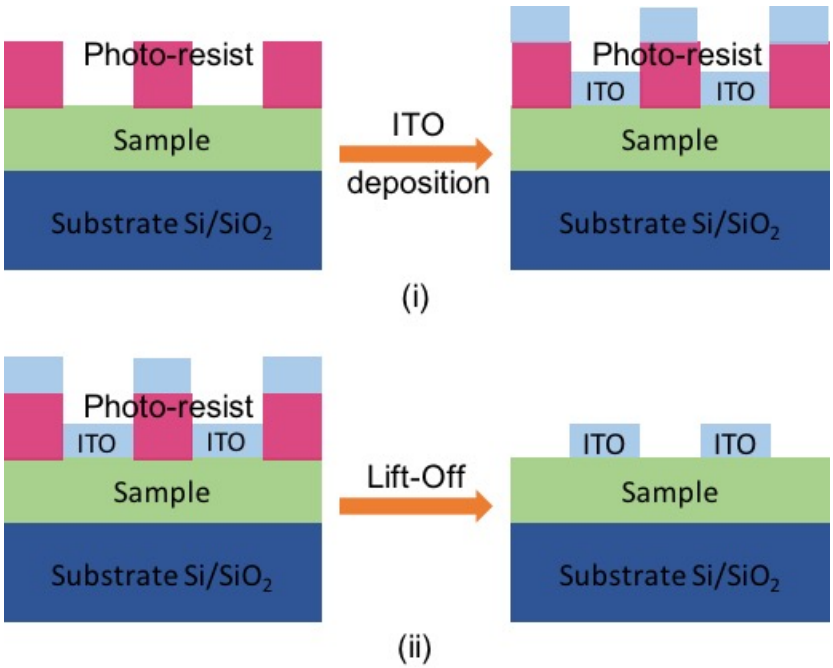

Figure 5.4 – (i) After the development step following the UV lithography, transparent ITO (which will serve as an electrode) is deposited using sputtering. ITO gets deposited both on the top of the resist and in the pits where the resist is not present on the sample.(ii) For the lift-off the sample now is treated with acetone which then removes the resist such that the ITO stays in the pits where the resist was not present and is removed from the rest of the part of the sample creating patterned electrodes.

Lift off

After ITO deposition, a lift-off step is necessary usually in acetone (for 1-2 minutes) and then in isopropyl alcohol (IPA) (for 1-2 minutes) to remove the remaining resist and the material which was above it (in our case it is ITO). The geometry thus defined will be represented by the remaining patterns areas that had been exposed (figure 5.4(ii).

The microfabrication of the electrodes were performed by me at Institut Néel using the mask of Anne Bernand Mantel and Marine Schott.

5.C.3 Connecting electrodes for measurement

After finally obtaining the patterned ITO electrodes on our samples, we stick it on a small (8 cm$\times$ 4cm) plastic sample holder on which there are multiple copper engravings as in the form of strips to connect the patterned electrodes. We use silver wires to connect the ITO electrodes and the appropriate copper lines on the sample holder using and a conducting epoxy glue on the sample and silver paste on the sample holder. The ground connection is made by scratching the sample with a tweezer and connecting this part to the other copper lines. The connections to a Keithley source to apply voltages on the sample are then made through the sample holder.

All the above steps were carried out by me at Institut Néel and at Spintec/CEA.

5.D Characterization techniques

After presenting the deposition and fabrication techniques of the samples, I will now discuss the different characterization tools used to study them, namely: Magneto-optic Kerr Effect (MOKE) magnetometer and microscope, Brillouin Light Spectroscope (BLS) and Vibrating Sample Magnetometer (VSM).

5.D.1 Magneto-Optic Kerr Effect (MOKE) Magnetometry and Microscopy

MOKE[118]?? magnetometry or microscopy is a powerful tool to determine magnetic properties of a sample locally by recording hysteresis loops and imaging domain and domain wall configurations. One of its advantages is that it is a fast method to determine out of plane (OP) anisotropy, in-plane (IP) anisotropy and transition zones.

Principle : Magneto-optic Kerr effect describes the change of the polarization states of light when reflected from a magnetic material. A linearly polarized light experiences a rotation of the polarization plane which is known as Kerr rotation, and a phase difference appears between the electric field components perpendicular and parallel to the plane of the incidence (plane containing the incident light and the normal to the sample surface) which is defined by Kerr ellipticity. By measuring the change of the polarization of the reflected beam, the magnetization state of the sample can be determined. This is achieved by using a polarizer through which a plane polarized laser beam is directed onto the magnetic sample. The reflected light from the sample then passes through an analyzer to determine the Kerr rotation produced by the

interaction of the laser with the local magnetization. There are three types of Kerr effects depending on the magneto-optic geometry used i.e the direction of the magnetization with respect to the plane of incidence. In the polar Kerr effect configuration (figure 5.5 (a)) the

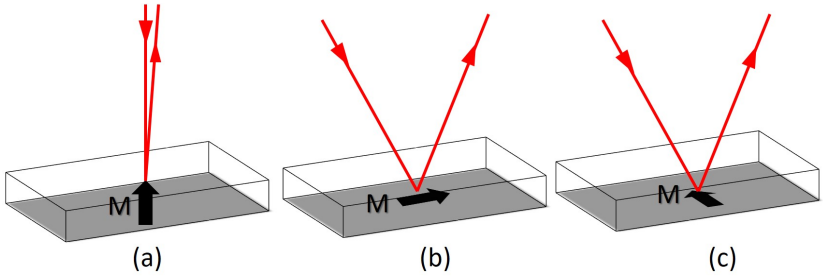

Figure 5.5 – Illustration of various configurations for the magneto-optic Kerr effect, from left to right: polar, longitudinal and transverse

magnetization M lies perpendicular to the sample surfaces but parallel to the plane of incidence. In the case of longitudinal Kerr effect (5.5 (b)) M lies parallel to the sample surface and to the plane of incidence. In the transverse configuration (figure 5.5(c)) M lies parallel to the sample surfaces and perpendicular to the plane of incidence.

MOKE Magnetometer

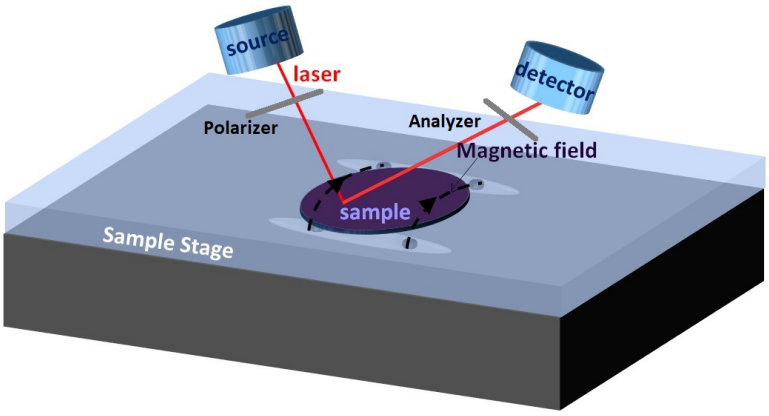

Figure 5.6 – MOKE setup indicating a laser source, a polarizer, an analyzer and detector. The magnetic field has both in-plane and out-of plane components.

We use commercial NanoMoke3 from Durham to characterize our samples. It essentially consists of a laser source, polarizer, analyzer, detector, sample stage and electromagnet. It is based on the magneto-optical Kerr effect described above and is sensitive to all the three, longitudinal, transverse and polar magneto-optical Kerr effects which depends on the positions of sample, polarizer and applied magnetic field.

The laser spot size diameter on the sample is around 300μm with a wavelength of 500 nm and is incident at angle of 45° with respect to the sample surface. The applied magnetic field at the sample location has both in plane and out-of-plane components, the out-of-plane component being 5.3 times smaller than the in-plane one. This geometry enables us to observe polar signal

along with either the longitudinal (if the in-plane component of the applied magnetic field is along the plane of incidence) or transverse (if the in plane component of the applied magnetic field is perpendicular to the plane of incidence) signal at the same time. This allows sensitivity to both the types of anisotropies: Out-of-plane anisotropy (OP)/PMA with polar signal and In-Plane (IP) anisotropy with longitudinal or transverse signals. This MOKE magnetometer used to measure the magnetic properties of thin magnetic films systems.

Typically it is used to trace hysteresis loops as a function of position of laser spot on the sample thanks to a motored x-y stage. We can thus automatically perform MOKE measurement loops at precise positions. In the case of samples with wedges of ferromagnetic layer and/or top oxide layers, measurements can be made at every 1mm distance, which corresponds to a 0.2 Å variation in thickness. A scan in thickness can hence be carried out for the sample sectioning it into parts and averaging many measurements for each point. Fig 5.6 illustratres the MOKE magnetometer setup higlighting different components. An example of the different shapes of

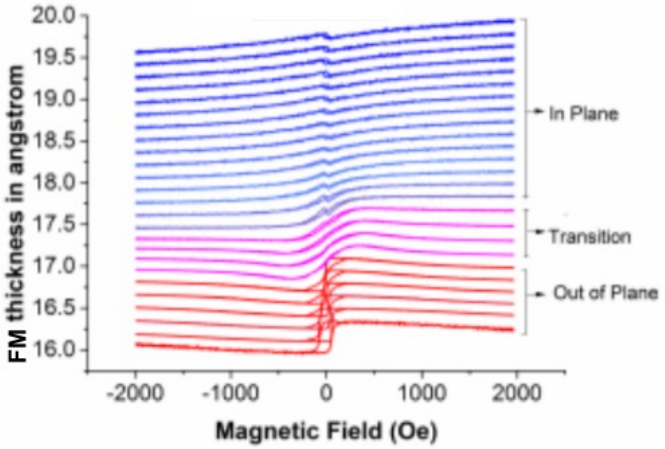

Figure 5.7 – Hysteresis loops obtained as function of FM layer thickness. Note that the Kerr signal is normalized and translated in terms of the thickness of the ferromagnet corresponding to the y-axis of the graph. The shape of the loops is square for lower FM layer thickness indicating PMA. The shape of the hysteresis loops obtained from the MOKE setup for higher FM layer thickness are indicated in blue showing in-plane anisotropy. The loops in pink show the transition loops from out of plane to in-plane anisotropy for increasing FM layer thickness

the hysteresis loops obtained for OP, IP anisotropy and transition regions is demonstrated in figure 5.7. Note here that loops obtained for different ferromagnetic thicknesses have been plot with the thickness indicated on the y-axis. Here the Kerr signal is normalized and translated as a function of the ferromagnetic thickness. For out of plane anisotropy corresponding to lower ferromagnetic thickness, nearly square loops are obtained. Near the ferromagnetic transition thickness from OP to IP, zero remanence loops are observed. On moving to higher ferromagnetic thickness we see that the shape of the loops changes corresponding to IP anisotropy. Since we have both out-of-plane and in-plane components of the magnetic field, we can work on different modes :polar-logitudinal or polar-transverse by changing the direction of the in-plane component of the applied magnetic field. In figure 5.8 we can observe that on changing the

direction of the magnetic field the orientation of the IP loops changes. To be able to distinguish clearly between the OP and IP loops we choose to apply the magnetic field perpendicular to the plane of incidence which is the polar-transverse mode, for our measurements.

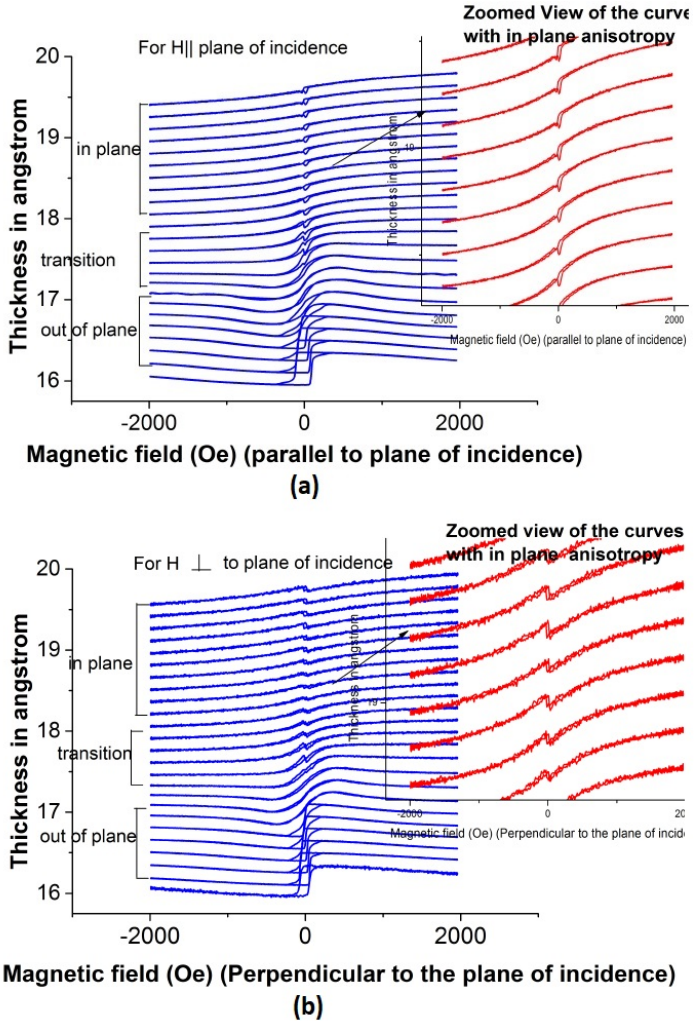

Figure 5.8 – Illustration of the change in orientation of the IP loops corresponding to higher ferromagnetic thickness on the y-axis, obtained when the in-plane component of the magnetic field is applied (a) parallel to the plane of incidence which is longitudinal mode (b) perpendicular to the plane of incidence which is transverse mode.

MOKE Microscope

The magneto-optic Kerr effect microscope can be used to image magnetic domain structures on the surface of magnetic materials. It can be configured for polar, longitudinal and transverse magneto-optical Kerr imaging. I will mainly focus on the polar-MOKE as I have only used this configuration for the characterizations. P-MOKE can be extremely useful to observe the magnetization dynamics as a function of applied magnetic field, electric field or even current for samples with out of plane magnetization.

A MOKE microscope works exactly on the same principle as the MOKE magnetometer except

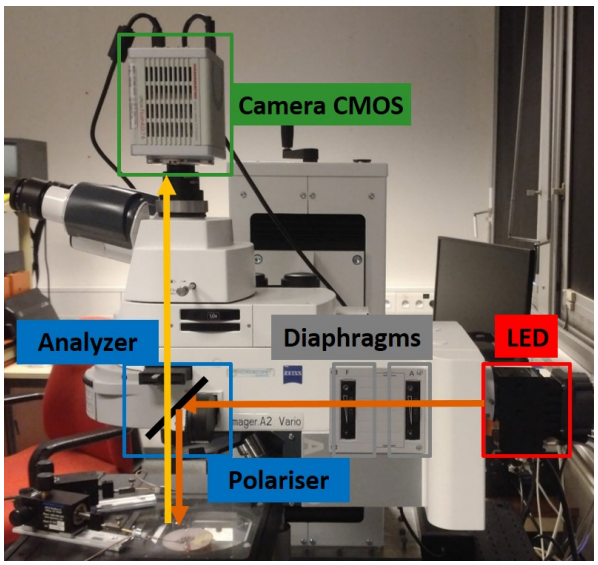

Figure 5.9 – MOKE Microscopy Setup demonstrating the different components (courtesy Willy Lim).

that there is an additional possibility of imaging the samples along with measuring hysteresis cycles. It consists of the same components as MOKE magnetometer, along with a microscope and CMOS camera. The MOKE setup is illustrated in Figs5.9and and5.10 The projection of the change in polarization through the analyzer is measured by the detector (camera) that can converting it into light intensity. Hence with an integrated computer it can be used to image the domains and domain walls in a ferromagnetic sample with out of plane anisotropy. A detailed image of the different components of a MOKE miscroscope is illustrated in figure 5.10. The resolution of the MOKE microscope is given by $r = \lambda/2NA$ where λ is the wavelength of the incident light which in this case is high power red Light emitting Diode (LED) and NA is the numerical aperture of the objective lens. For NA=1, the maximum resolution is $0.35\mu m$. Different lenses can be employed for imaging the domain structures depending on the required resolution.

All the MOKE measurements were performed by me at Institut Néel and Spintec/CEA with the help of colleagues. Later on all the data were treated by me using Origin and Matlab software at Spintec/CEA.

5.D.2 Brillouin Light Spectroscopy

Brillouin scattering is named after Léon Nicolas Brillouin (1889-1969). The french physicist first predicted the inelastic scattering of light (photons) by thermally generated acoustic vibrations (phonons) in 1922. These days Brillouin Light Spectroscopy (BLS) has emerged as one of the most important tools to measure interfacial DMI in ultra thin films consisting of heavy metal/ferromagnet/meta oxide layers. It offers minimum parameters to be determined to extract the exact value of DMI.

Principle : BLS employed to study interfacial DMI is based on the inelastic scattering of a photon by a magnon *i.e.* spin wave. Spin waves in ferromagnet have a spatial chirality, which

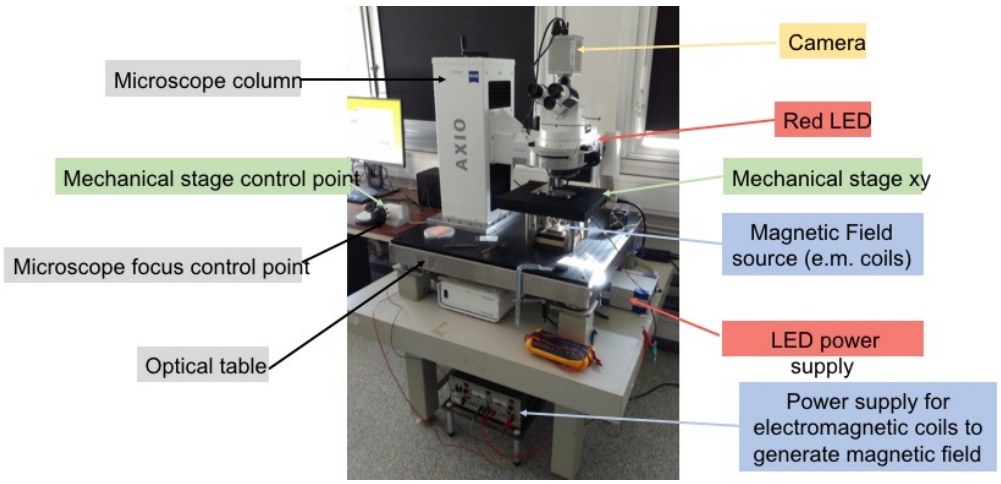

Figure 5.10 – MOKE Microscopy Setup demonstrating the different components (courtesy Willy Lim).

depends on their propagation direction with respect to the direction of the magnetization. Using the an illustration from referenceNembach et al.[119] we see from figure 5.11, that when the magnetization M is parallel to the sample plane, along z-axis in this example, the spin waves traveling perpendicular to it *i.e.* in the $\pm$ x direction have opposite chirality (anticlockwise or clockwise). Since the DMI vector d_{ij} (defined in chapter 2 and 3) imposes its own chirality depending on its sign, it modifies the spin wave dispersion relation. This geometry is known as Damon Eshbach.

When the magnetization is saturated in the film plane, the modification in the frequency of the spin waves propagating in a direction perpendicular to it due to the DMI is given by

$$f = f_0 + \Delta f \tag{5.1}$$

where f_0 is the frequency in the absence of DMI. The change in the frequency Δf is[120, 121]

$$\Delta f = \frac{2\gamma}{\pi M_s} k_{SW} D \tag{5.2}$$

where γ is the gyromagnetic ratio, M_s is the saturation magnetization , k_{SW} is the spin wave vector and D ($\propto d_{ij}$) is Interfacial DMI energy.[114, 119–122] The DMI produces a linear shift in k_{SW}, and depending on the direction of propagation and polarity of the magnetization saturation. If the DMI favors the spatial chirality of the spin wave, the spin wave frequency is reduced and vice-versa. In a BLS setup, a laser spot is focused on the sample and the inelastically backscattered photons are analyzed on their interaction with the magnons /spin waves. It leads to the Stokes process where the magnons are created and the anti-Stokes process where the magnons are annihilated due to conservation of momentum. The energy of the backscattered photons hence corresponds to the frequency difference of the oppositely traveling spin waves. Therefore measurement of the shift between the Stokes (f_S) and Anti-Stokes (f_{AS}) frequency peaks gives a direct determination of DMI.

BLS setup : A BLS setup essentially consists of a laser source, a flexible sample stage and Fabry-Perot interferometer as an analyzer (shown in figure 5.12 which is borrowed from the

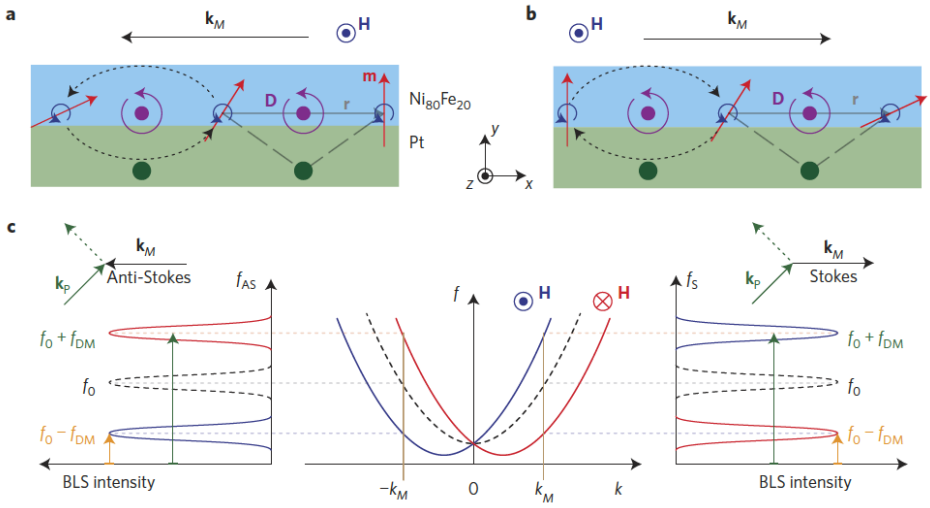

Figure 5.11 – From reference Nembach et al. [119] a, Damon Eshback geometry spin wave propagating at the Ni80Fe20/Pt interface with wavevector $k_M \parallel -x$ with the magnetization $M \parallel +z$. All individual moments precess in the external field H in an identical (anticlockwise) manner, indicated by the blue arrows. The canted arrows depict the dynamic components of the spins at a snapshot in time. The dashed arrows indicate the spatial chirality of the spin wave along x. Any two neighbouring spins (red arrows), are coupled by a DMI vector D (purple vector pointing out of page) via a three-site exchange mechanism that includes a Pt atom (green atoms). The Pt atom serves to both break the symmetry and provide the necessary spinâorbit coupling. The preferred chirality of the antisymmetric exchange indicated by the purple arrow circulating about the DMI vector is identical to the spatial spin wave chirality. b, For $k_M \parallel +x$, the spatial chirality of the spin wave is opposite to that favored by the DMI. The individual moments precess anticlockwise around the external magnetic field H as in a, but now k_M points in the opposite direction. c, The central panel shows schematic spin-wave dispersion curves in the absence of DMI (dashed) and with DMI (solid) for $M \parallel \pm z$, respectively. Sketches of the expected BLS spectra for $-k_M$ (anti-Stokes process, annihilation of a magnon, propagation in the -x direction) and $+k_M$ (Stokes process, generation of a magnon, propagation in the +x direction) are shown on the left and right sides of the lower panel, respectively.

group of M. Belmeguenai at LSPM in Université Paris 13). In the BLS experiment performed at LSPM in Paris, we used Damon Eshbach geometry with 2×3-pass Fabry-Perot interferometer and sufficiently large in-plane magnetic fields to saturate the magnetization in the plane of the sample. The wavelength of the laser employed is $\lambda = 532$ nm. A typical BLS spectrum is shown in figure 5.13 where intensity is plot as a function of the frequency. The corresponding Stokes and Anti-Stokes frequency peaks are shown.

In order to determine the DMI, the frequency difference obtained between the Stokes and Anti-Stokes frequency peaks is plotted as a function of spin wave wave vector k_{sw} whose length is given by$4\pi \sin(\theta_{inc})/\lambda$ where θ_{inc} is the angle of incidence of the laser and λ the wavelength of the incident laser. θ_{inc} is therefore swept leading to k_{sw} variation typically between 0-20 μm^{-1}.Typical frequencies of spin waves probed are therefore in the range of tens of GHz. Figure 8.2 shows the plot of frequency difference as a function the spin wave vector k_{SW}. The variation is linear which is expected as described earlier. The slope of this plot is used to determine the DMI parameter using equation5.2

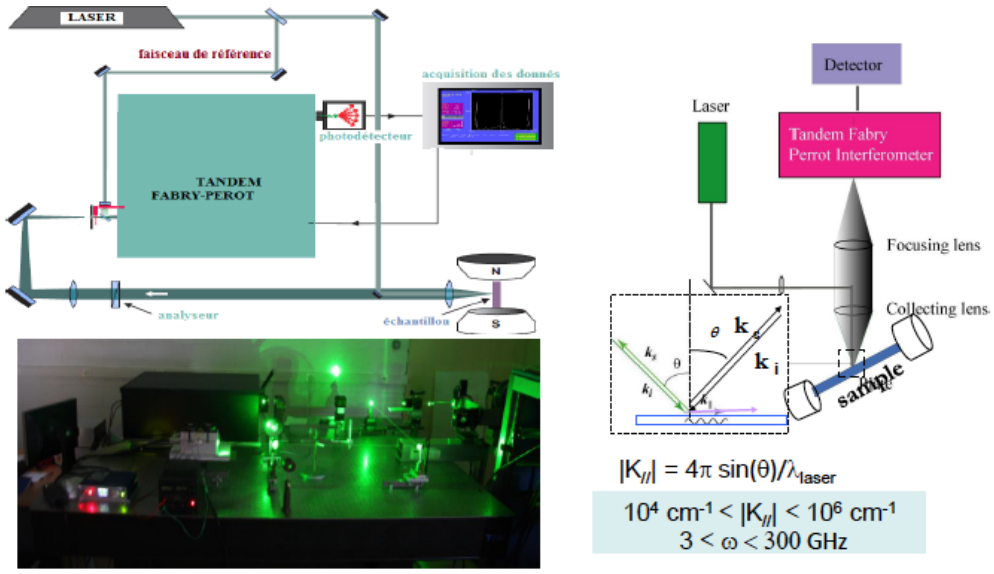

Figure 5.12 – BLS setup indicating the different parts and components (M. Belmeguenai at LSPM in Université Paris 13).

The intrinsic precision of Brillouin measurements is on the order of 0.1 - 0.5%. All the measurements of the BLS spectrum are carried out for both ±H to ensure any discrepancies due to the setup. It hence helps to calibrate the setup accurately

The BLS measurements were performed at the lab LSPM at Université Paris 13 with the help of Mohamed Belmeguenai and Yves Roussigné. I participated in all the measurements. I learned the various steps associated to the BLS measurement including mounting of the sample, alignment and focusing of the laser spot and data accumulation. Later on I treated all the data by myself on origin software.

5.D.3 Vibrating Sample Magnetometer

The vibrating sample magnetometer can give a wide range of information about the magnetic sample like its easy axis, coercivity, anisotropy field, saturation magnetization by the measurement of hysteresis loops.

Principle : The Vibrating Sample Magnetometer is based on Faraday's Law of electromagnetic induction which states that a change in the magnetic flux in a circuit produces a voltage (electro motive force) and hence an electric current flows through it. The sample to be measured is placed in a magnetic field and vibrated close to a pair of pickup coils. The change in magnetic flux in the pick up coils due to the vibration of the sample induces voltage/current which is proportional to the sample's magnetic moment. Using a lock-in technique, the signal at the same frequency as the vibration frequency of the sample is extracted. A varying magnetic field produced by an electromagnet is applied in order to obtain m (H) loop. A schematics of the VSM setup is shown in figure5.15.

The VSM can also be used to measure magnetic moment as a function of applied magnetic field for different temperatures. Both hard and easy axis measurements can be performed for

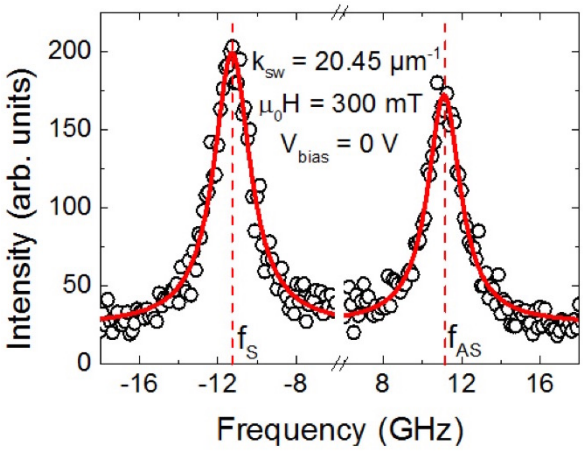

Figure 5.13 – BLS Spectrum: Intensity as function of frequency. The Stokes frequency peak $|f_S|$ corresponds to the creation of the phonon whereas Anti-Stokes frequency peak $|f_{AS}|$ corresponds to the absorption of a phonon. The difference between them $\Delta f = |f_S| - |f_{AS}|$ gives a direct measurement of DMI.

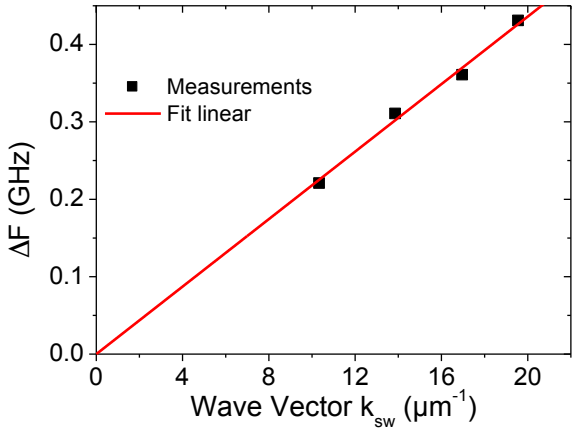

Figure 5.14 – Δf measured as a function of spin wave vector k_{SW}

the in plane and out of plane anisotropy samples. the typical size of the sample s is with the range $0.25cm^2 < s < 1cm^2$. It also has a provision to rotate the sample at any angle with respect to the magnetic field applied which is very beneficial to know the spontaneous alignment of magnetization specially if it is near a transition from in plane to out of plane anisotropy in terms of thickness.

Measurement of Magnetic Anisotropy

VSM can be used to determine the anisotropy energy of a ferromagnetic sample, by performing measurements along two orthogonal directions of the magnetic field relative to the sample, one along an easy axis and one along hard axis. The Magnetic Anisotropy Energy (MAE) is given by the area enclosed between the loops measured along the out of plane direction and in plane direction *i.e.* MAE=Area(OP)-Area(IP).[18],[123] This is based on elementary electromagnetic considerations which show that the energy needed to change the sample magnetization in an

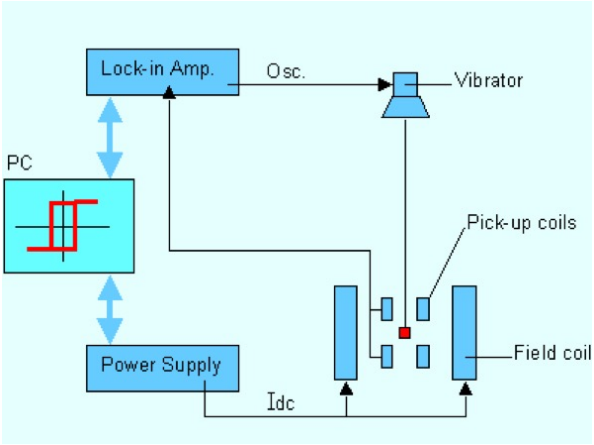

Figure 5.15 – Vibrating Sample Magnetometer (VSM) setup exhibiting different components. The sample is vibrated close to the pick-up coils. The voltage induced in the pick-up coils is extracted through a Lock-in amplifier.

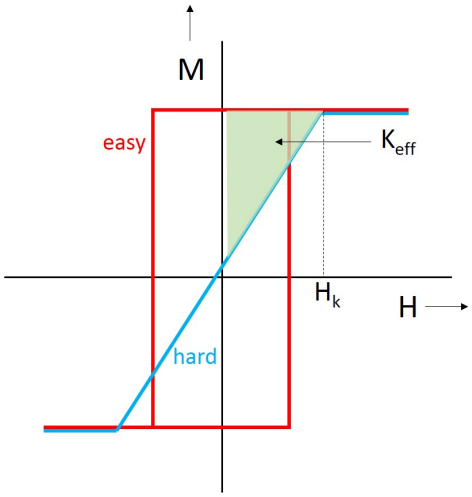

Figure 5.16 – Easy axis and Hard axis measurements by VSM to determine effective anisotropy of the sample.

applied field H by an amount dM is given by $\mu_0 H\, dM$. If the easy axis loop is square then the K_{eff} can be found directly from the hard axis measurement using the relation $H_k = 2K_{eff}/\mu_0 M_s$, where H_k is the anisotropy field measured along the hard axis. Hk corresponds to the magnetic field required to saturate the magnetization along the hard axis. In the case of an OP film, the easy axis will be OP loop and the hard axis will be in-plane. K_{eff} will then be positive. On the other hand, for IP films, the hard axis will be OP and easy axis will be IP loops. In that case, K_{eff} will indeed be negative. The figure 5.16 depicts the area between the easy axis and hard axis loops, which gives the effective anisotropy constant K_{eff}.

All the VSM measurements and data treatment were performed by me at Spintec/CEA.

5.E Conclusion

The above described sample fabrication and characterization techniques have been used for the major part of my PhD tenure. Apart from these aforementioned techniques, I also got trained to prepare magnetic tunnel junctions (MTJs) using clean room facilities. I fabricated several wafers of MTJs using Ion Beam etching, UV lithography, Reactive Ion etching, Evaporation deposition techniques and measured their tunnel magnetoresistance (TMR) vs voltage response. However this study needs to be pursued further in order to conclude any concrete results.

Part III

Results and Discussion

6

Study of different Heavy Metal/Ferromagnet/Metal Oxide systems

6.A Introduction

Engineering the interfaces between ferromagnetic (FM) layer and heavy metals (HM) or/and oxides (MOx) in ultra-thin film systems is crucial for new age spintronic devices. The emerging research is now directed towards phenomena where interfaces play a major role. For example the study and manipulation of magnetic textures like skyrmions which are stabilized by an interplay of interfacial DMI and other magnetic interactions, necessitate a detailed study of interface physics.

In this chapter, several multilayer systems primarily consisting of heavy metal/ferromagnet/metal oxide (HM/FM/MOx) ultra-thin layers have been discussed. The main focus is on the evolution of magnetic properties, in particular the variation of magnetic anisotropy and magnetically dead layers, as a function of the FM layer thickness, top metal (M) thickness and the oxidation state of the FM/MOx interface. This eventually would help us to predict the optimum conditions for obtaining chiral magnetic textures like skyrmions.

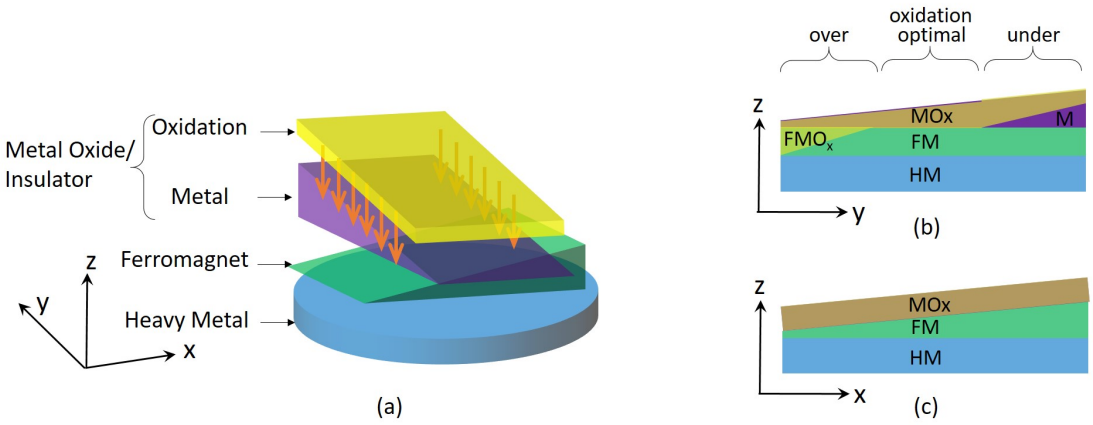

Figure 6.1 – (a) Schematics of double wedge system of HM/FM/MOx trilayer. The wedge of FM and MOx are perpendicular to each other. (b) Along the y-axis *i.e.* where the FM thickness is constant, due to the wedge of top metal, oxidation results in underoxidized, optimally oxidized and overoxidized zones.(c) View of the sample in the x-z plane for a given oxidation state of MOx.

6.B Double wedge sample description

In order to study the evolution of the magnetic properties in HM/FM/MOx system as a function of different FM and MOx, their thicknesses and their interface oxidation state, a double wedge system is used, described in detail in chapter 5. The bottom HM layer has a constant thickness on a Si/SiOx 100mm wafer, a wedge of FM is deposited on top of it by sputtering, followed by a wedge of another metal on the top in the direction perpendicular to the first wedge. An oxidation step then follows to form the top metal oxide layer. Owing to this double wedge, the magnetic properties vary throughout the 100 mm sample giving access to different combination of thicknesses of the two layers and the oxidation state of the top metal. A pictorial demonstration is made in figure 6.1(a). Further we see in figure 6.1(b) that along the y-direction for a constant FM thickness, due to the wedge of top metal, the oxidation state varies giving underoxidized, optimally oxidized and overoxidized zones respectively. The underoxidized region pertains to the part where a large chunk of the top metal is left unoxidized and is in direct contact with the FM layer. Whereas for lower top metal thickness a part of the FM gets oxidized too forming overoxidized region. Figure 6.1(c) shows the same stack along x-direction where we have the wedge of FM layer for a constant thickness and oxidation state of the top Ta.

6.C Magneto-optic Kerr Effect Mapping

Having obtained the sample with double wedge, the next step is to study its magnetic properties. We use Magneto-Optic Kerr Effect(MOKE) magnetometer called NanoMOKE3 from Durham. It scans the sample every 1.5 mm and records hysteresis loops for applied magnetic field. This MOKE setup is sensitive to both out-of-plane (OP) and in-plane (IP) magnetization signals but the sensitivity is higher for the polar than the longitudinal part. The applied magnetic field has both out-of-plane and in-plane components. Therefore these conditions result in different

shapes for the OP and the IP anisotropy zones explained in chapter 5 . Note that this tool is used to quickly identify the OP and the IP anisotropy zones. For quantitative analysis other methods should be employed.

A matlab/origin program is used to plot a remanence map from the above data. We take Ta/FeCoB/TaOx sample as a reference to explain the different anisotropy zones we can encounter on a double wedge and that by extracting certain parameters we can construct a model to better understand such trilayer systems. It can be seen in figure 6.2(a) that the well defined blue region displays low remanence corresponding to hard axis curves or curves with zero coercivity and zero remanenance (like butterfly loop of the skyrmion zone explained in chapter 7) and red region represents high remanence corresponding to an easy axis hysteresis loop. Depending on the thickness of the FM and MOx, OP or IP anisotropy can be preferred leading to high remanence shown in red for both the cases. The OP anisotropy also referred to as Perpendicular Magnetic Anisotropy (PMA), the IP anisotropy and the Paramagnetic (PM) zones are marked in the map. The PM zone can be seen as blue background with pixels of different colors on the top, *i.e.* it is noisy in terms of Kerr Signal and corresponds to the zone which is non magnetic at room temperature. We can also call it as magnetically dead zone or more commonly referred to as dead layers. In means that the Curie temperature of this film (T_C) is below room temperature due to finite size effects. The shape of the hysteresis loops corresponding to the OP, IP anisotropy and PM zone along the two wedges *i.e.* FeCoB wedge and TaOx can be seen in figure 6.2 (b) and (c) respectively.

6.C.1 Variation of properties along the FM wedge

A series of hysteresis loops are shown in figure 6.2(b) along the FM thickness for a constant M layer thickness. Note that the y-axis is normalized Kerr signal translated in terms of thickness of the FM layer. Therefore each loop is obtained for the particular FM layer thickness indicated on the y-axis. The shape of the hysteresis loops indicate the OP, IP and the transition zones. There are two transition zones corresponding to the thicknesses of the FM where (i) the easy axis changes from out-of-plane to in-plane beyond a critical value of t_{FM} (ii) the layer becomes paramagnetic for low thickness of FM. These transition zones are in blue on the remanence map. The noise represents the magnetically dead zones indicating that the corresponding FM layer thickness is magnetically dead.

This succession of anisotropy axes as a function of FM layer is expected. When the FM is too thin, it is paramagnetic and hence not magnetic at room temperature leading to dead layers. Then as the thickness of FM starts to increase beyond a certain threshold, the surface anisotropy starts to emerge giving OP anisotropy. Finally when FM is thick enough, the shape anisotropy (also called dipolar anisotropy) dominates over surface anisotropy leading to IP anisotropy as shown in figure 6.3. This can be understood by recalling the equation in chapter 2 : The effective magnetic anisotropy energy density in uniaxial thin films can be written as a sum of surface/interface (K_s) and volume contributions(K_v) .[18, 19]

$$K_{eff} = K_v + \frac{K_s}{t} \tag{6.1}$$

where $K_v = K_b + K_d$; K_b is the bulk magnetocrystalline anisotropy and K_d is the shape anisotropy

and is negative ($=\frac{1}{2}\mu_0 M_s^2$), and t is the effective thickness of the ferromagnetic film. K_s includes surface contributions of the two interfaces.

6.C.2 Variation of properties along the MOx wedge

A series of hysteresis loops along the MOx layer thickness for a fixed FM layer thickness is also indicated in figure 6.2(c), showing OP zones and magnetically dead zones. Here we see that for the optimum thickness M, as the interface of FM/MOx is optimally oxidized, we obtain OP anisotropy due to K_s being positive and dominating the dipolar contribution. When M is too thin it leads to oxidation of the FM layer forming FMOx which is not ferromagnetic. This overoxidized region leads to paramagnetism and hence dead layers. IP transition for corresponding to slighly overoxidized thickness is however surprising as it corresponds to thinner FM layer. It might be if the K_s of the FM/FMOx is smaller than FM/MOx. Finally for thickner M, i.e underoxidized region, again a PM region is observed which is surprising. In the case of Pt/Co/AlOx, the underoxidized region gives an IP anisotropy. However, here in the present example of Ta/FeCoB/TaOx, we observe dead layers when the top Ta is thick beyond a certain threshold thickness for a certain degree of oxidation. This happens due to the intermixing of the Fe and Ta atoms as heavy Ta is deposited on Fe by sputtering.

To summarize we see that the dead layer/PM region (noisy signal) is obtained for all oxidation states but the transition to from OP to IP anisotropy is obtained for FM layer thickness beyond a certain value that is not same for all M thicknesses indicating that the K_s varies as function of the M layer thickness and hence the oxidation state of FM/MOx interface. I This can be understood as variation of dead layer thickness as a function of M layer thickness shown in figure 6.4: the solid line represents the variation of dead layer thickness (t_{DL}). For a given thickness of M layer, t_M, the transition between OP and IP anisotropy zone varies as shown by the dashed line in figure 6.4 as the value of the surface anisotropy evolves.

In order to get a deeper insight into the evolution of the magnetic properties as a function of the thicknesses of FM and MOx layers we develop a simple model which is described next.

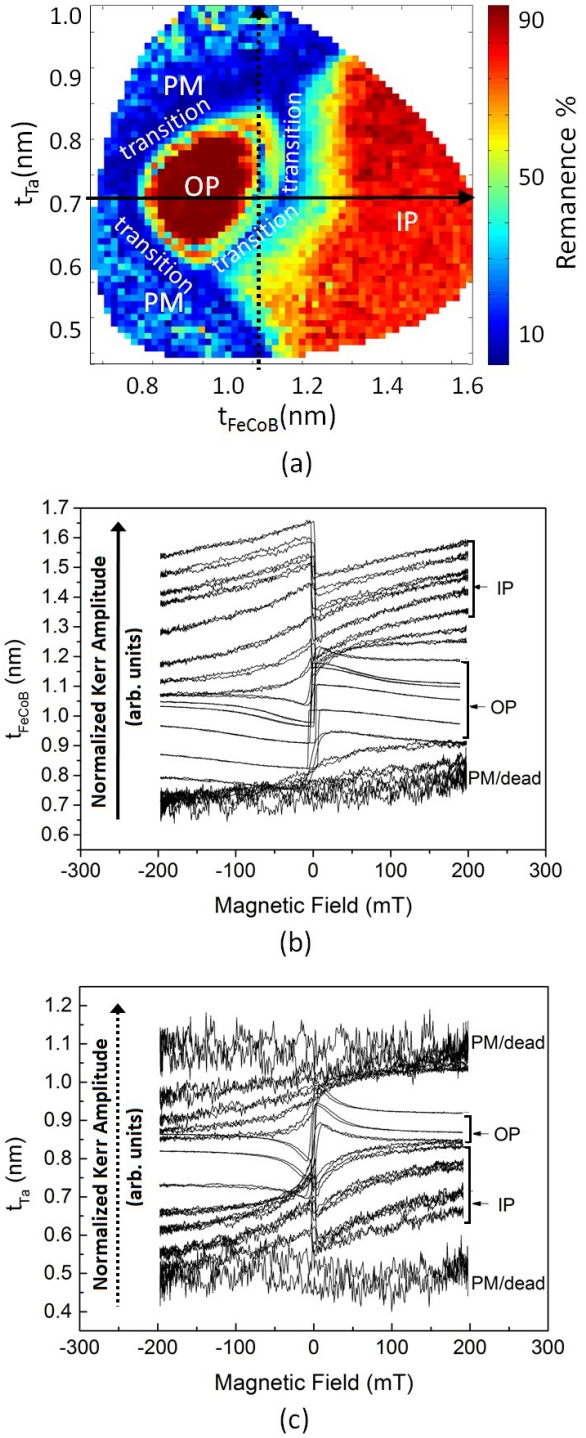

Figure 6.2 – (a) Remanence map obtained from MOKE measurement for Ta/FeCoB/TaOx sample. High and low remanence zones are represented in red and blue respectively. The OP anisotropy, IP anisotropy and the paramagnetic (PM) or dead layer zones are marked. Hysteresis loops along a horizontal cut in the center are shown in (b). The shape of the hysteresis loops reveal the preferred anisotropy as a function of the FM layer thickness. The noisy signalm below represents the paramagnetic or dead layer zone. A similar set of hysteresis loops along vertical cut in the center of (a) is presented in (c) showing the in-plane to out-of-plane and further to in-plane anisotropy transitions as a function of Ta thickness.

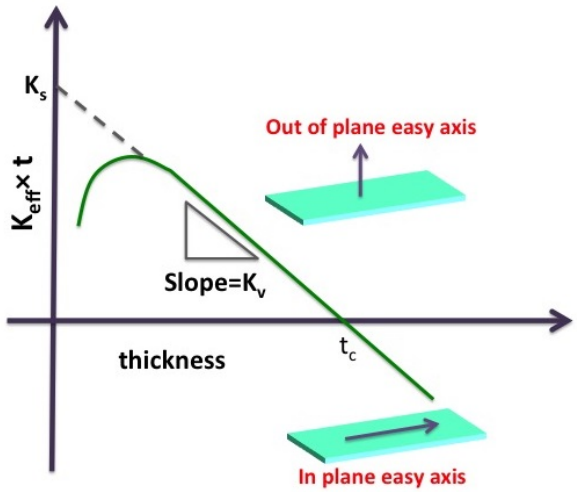

Figure 6.3 – Plot of effective magnetic anisotropy K_{eff} multiplied by the thickness t of the ferromagnet plot as a function of the ferromagnetic thickness. When $K_{eff} > 0$ the anisotropy is perpendicular to the surface *i.e.* out of plane, whereas when $K_{eff} < 0$, the anisotropy is in-plane i.e magnetization prefers to lie in the plane of the ferromagnetic film.

6.D Modeling the magnetic properties of trilayer double wedged structures

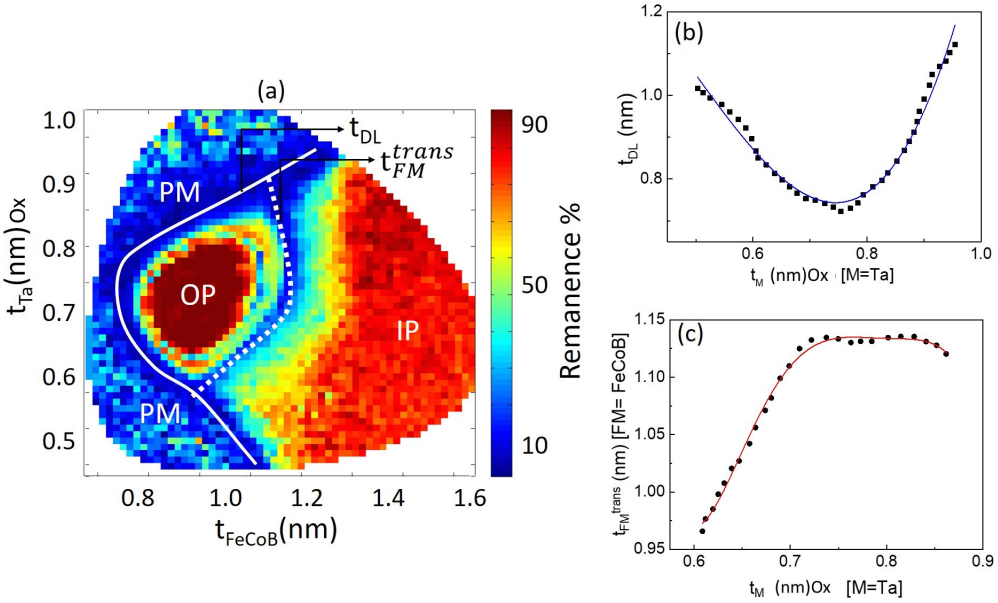

Figure 6.4 – (a)Remanence map obtained from MOKE measurement for Ta/FeCoB/TaOx sample. The dead layer variation and the FM transition thickness variation as a function of the Ta thickness is traced. The corresponding maps are plotted in (b) and (c) respectively

From the remenance maps, a broad idea of the different anisotropy zones and the variation of dead layers can be obtained. To further go into the details we have constructed a simple model based on the characteristics above to better understand and describe these trilayer systems. To build a model I first highlight the details of the magnetically dead layers.

Magnetically dead layers : In ferromagnetic thin films grown by sputtering with a heavy metal underneath and a metal oxide layer on top to increase PMA, the effective thickness of the ferromagnetic layer contributing to the total moment and hence the magnetization is often debated. A prelude to this phenomenon is often the interaction of the ferromagnetic layer with the two sandwiching layers. Sputtering also induces a certain degree of intermixing of these layers at the respective interfaces specially when a HM is sputter deposited on FM. Oxidation of the top metal layer is also crucial in determining the magnetic property of the FM layer. All these factors can render a certain thickness of the ferromagnetic layer being magnetically dead, *i.e.* a reduced total moment is seen than what is expected from the actual thickness of the ferromagnetic layer deposited. The dead layer can be thought of as a ferromagnetic layer with a reduced Curie temperature (T_c) hence paramagnetic at room temperature.

I will now describe what we can expect in the case of double wedged system, where we have a heavy metal underlayer with a constant thickness, followed by deposition of perpendicular wedges of ferromagnet and metal respectively and then successive oxidation of the top metal layer (explained in the figure 6.1). Here, the dead layers can be formed by three sources: (i)

an intermixing of the heavy metal and ferromagnet at the bottom interface, (ii) oxidation of the ferromagnet where the top metal layer is too thin, we call this as being overoxidized (iii) intermixing of the top metal and the ferromagnetic layer (top interface), we suppose this case when the top metal is not adequately oxidized i.e underoxidized. This is what we observe in the remanence map of Ta/FeCoB/TaOx for example.

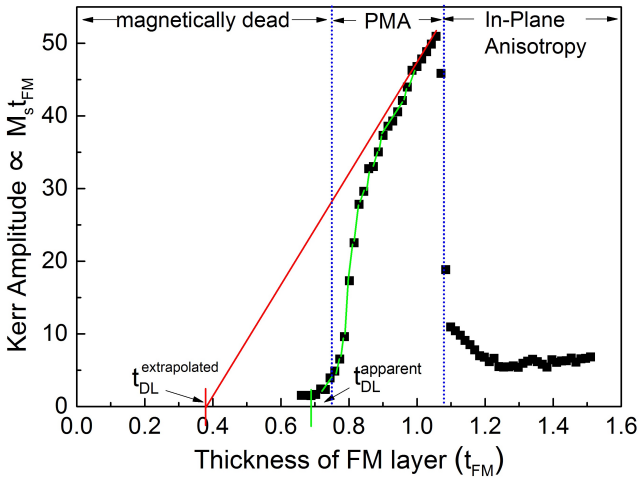

Figure 6.5 – Kerr amplitude as a function of the FM layer thickness.The extrapolation of the constant slope for the highest remanence gives the dead layer thickness t_{DL}^{real} as the Kerr signal is proportional to $M_s \times t_{FM}$. The thickness at which the Kerr signal drops to zero is shown as $t_{DL}^{apparaent}$.

Dead layer paradox : I would like to mention here that the dead layers that we observe in the above remanence map is quite thick from what we usually see in literature. To elaborate, the usual extraction of dead layer thickness is carried out by plotting $M_s \times t_{FM}$ as a function of t_{FM} and finding the x-axis intercept *i.e.* the FM layer thickness corresponding to M_s=0. This can be realized by either performing VSM measurements for various t_{FM}, which can directly give M_s or by Kerr Magnetometry (NanoMOKE3 deescribed in chapter 5) where Kerr amplitude is an indirect measurement of $M_s \times t_{FM}$ along a FM wedge. Kerr Magnetometery is in fact a faster method as it can speedily scan a sample every mm^2 giving large number of data points during short time interval. A plot of Kerr amplitude as a function of t_{FM} is presented in figure 6.5. The usual extraction of dead layer is by extrapolating the constant part of the slope (indicating constant M_s) on the x-axis. It can be seen that for Ta/FeCo/TaOx, the extrapolated dead layer thickness obtained is around 0.38 nm. However it is also seen from the graph that when t_{FM} is decreased, the Kerr amplitude drops way before the dead layer $t_{DL}^{extrapolated}$ obtained by extrapolation. The threshold thickness of the ferromagnet at which the Kerr amplitude drops to zero can be called as an apparent dead layer *i.e.* $t_{DL}^{apparent}$. We can assume that the magnetic properties change drastically between these two thicknesses, the layers are probably still magnetic but with a reduced T_c. Since we perform all the measurements at room temperature, for the sake of simplicity, I will be referring to $t_{DL}^{apparent}$ as t_{DL}. These values of t_{DL} as mentioned before are larger than the ones observed in literature for the aforementioned reasons.

6.D.1 Modeling dead layer variation :

As described previously, using the same remanence map of Ta/FeCoB/TaOx, we can trace the dead layer variation by marking the borders between the OP anisotropy zone and paramagnetic zone, as a function of the top M thickness subsequently oxidized $t_M Ox^*$ (figure 6.4(b)): the solid line represents the variation of dead layer thickness (t_{DL}). This trace can be either modeled as a Gaussian function or a polynomial function with a saturation limit, illustrating the dead layer dependence on the (i) overoxidized part (ii) optimally oxidized and the (iii) underoxidized part. Now to construct a simple model, we hypothesize that the dead layer has three origins as depicted in figure 6.6a, and we thus write it as

$$t_{DL}(t_M) = t_{DL}(bottom) + t_{DL}(ox) + t_{DL}(M) \tag{6.2}$$

This dead layer thickness corresponds in our model to the thickness of FM above which there is magnetism at room temperature. The $t_{DL}(bottom)$ corresponds to the contribution from the bottom HM layer, which in the present example is Ta layer. As this layer has a constant thickness for the whole wafer, we consider this dead layer contribution as a constant. Then $t_{DL}(ox)$ is the threshold layer due to the oxidation of FM layer in the overoxidized region, it thus corresponds to the thickness of FeCoB in the present case that is converted in non magnetic FeCoB-oxide. Obviously, its thickness is larger when more oxygen atoms reach the interface, *i.e.* for thinner Ta. A polynomial variation is used for $t_{DL}(ox)$ as a function of top t_M oxidized which is t_{Ta} in the present case, with the constraint that at the optimum oxidation state, this contribution is zero. Also, for a Ta thickness that is zero, it would lead to oxidation of the FeCoB that would be over a thickness t_{DL}^{OxMax} that would be defined by the quantity of oxygen provided to the system. The thickness of FeCoB oxidized is linked to the quantity of oxygen needed to fully oxidize FeCoB as compared to the Ta. This can thus give a hint on the stoichiometry of the oxide.

For the $t_{DL}(M)$, taking the case of $t_{DL}(Ta)$ we hypothesize that the more Ta deposited on top of the FeCoB, the thicker the dead layer, as it seems to be linked to a mix of Fe and Ta. Again a polynomial variation is taken for the $t_{DL}(Ta)$ with t_{Ta}. A Gaussian distribution can also be used to depict the same but we have put that for the perspectives. Finally, we impose that the dead layer thickness cannot be larger than the FeCoB thickness. It will thus saturate with the thickness of FeCoB.

6.D.2 Modeling ferromagnetic re-orientation transition thickness (t_{FM}^{trans}) variation

Further we also see that the magnetic anisotropy changes as a function of FeCoB thickness and is also dependent on the thickness of the top metal oxide (TaOx for the present case). Using equation 6.1, it can be shown that in the case of OP to IP anisotropy transition, corresponding

*Note that $t_M Ox$ denotes the thickness of top metal (=Ta,Mg,Al etc) followed by an oxidation step. Due to the thickness gradient of the top metal, oxidation results in an eventual oxidation gradient of the metal.

to K_{eff}=0, the equation can be written as:

$$K_v + \frac{K_s}{t_{FM}^{trans} - t_{DL}} = 0 \tag{6.3}$$

$$K_s = -(t_{FM}^{trans} - t_{DL}) \times K_v \tag{6.4}$$

such that t_{FM}^{trans} is the transition thickness from OP to IP anisotropy. Therefore on the same remanence map the transition thickness t_{FM}^{trans} of FeCoB layer can be traced as a function of the top TaOx thickness by marking the borders between OP anisotropy and IP anisotropy zone. As a function of the M layer thickness and its oxidation state, t_MOx, the transition between OP and IP anisotropy zone varies as shown by the dashed line in figure 6.4 as the value of the surface anisotropy evolves. This variation of t_{FM}^{trans} can hence indicate the variation of K_s as a function of the top metal oxide (TaOx in the present case) therefore giving information about the quality of the interface. The variation of K_s can also be modeled as a Gaussian or a polynomial. We have used a Gaussian function for our model with different sigmas (half width at half maximum) : σ_{Ox} and σ_M to indicate the possibly different variation of the Gaussian function on the overoxidized and underoxidized parts of the t_M respectively as shown in figure 6.6b.

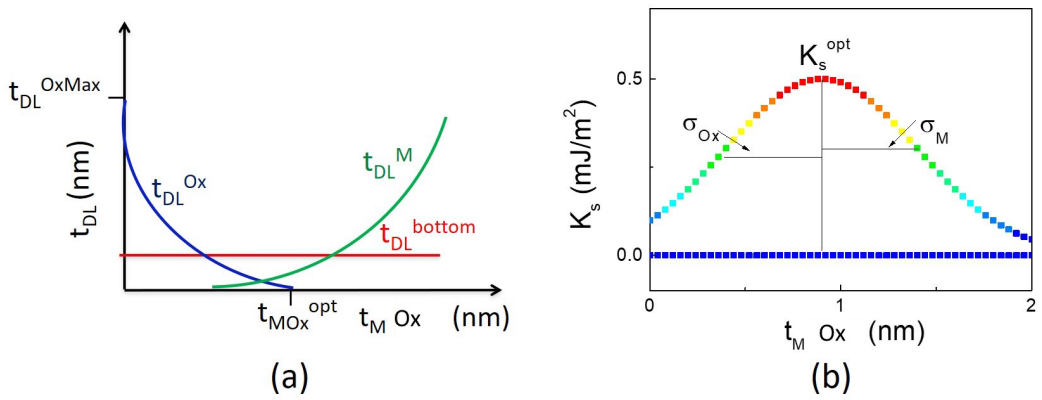

Figure 6.6 – (a) Dead layer t_{DL} modeling as function of t_MOx: with polynomial variation for the underoxidized and overoxidized zone contributions and constant for the bottom HM layer. (b) Surface anisotropy K_s modeling as a function of t_MOx: by combining the t_{FM}^{trans} and t_{DL} variation extracted from the remanence maps. The function used is Gaussian with two different σs (σ_{Ox} for the overoxidized part and σ_M for the underoxidized part)

6.D.3 Resulting effective anisotropy K_{eff} variation

To calculate the effective anisotropy we use equation 6.1. The M_s is the bulk M_s that we have used and is constant as long as the ferromagnetic thickness is larger than the dead layer thickness. For the value, we have used M_s= 1 MA/m.

For the calculation of K_s, as it is interfacial anisotropy, we made it vary along the wedge of Ta and not along FeCoB wedge as it is linked to the oxidation state of the FeCoB/TaOx interface. The maximum K_s is found at the optimum oxidation position (optimum thickness).

Then we used a Gaussian variation along the wedge, with different values of σ_{Ox} and σ_M in the overoxidized and underoxidized region respectively. Again, in the case when the dead layer thickness is equal to the total ferromagnetic thickness, we impose a K_s=0 as the film is no more magnetic. This leads to dead layer that are non magnetic by definition and thus have no magnetic anisotropy. Finally K_{eff} is calculated by using: $K_{eff} = \frac{K_s}{t_{FM}-t_{DL}} - \frac{1}{2}\mu_0 M_s^2$

6.D.4 Fitting of the experimental data

In order to fit our experimental data with the MOKE remanence maps, we thus calculate K_{eff} for thicknesses in the extended range of 0-2 nm for both Ta and FeCoB *i.e.* t_{FM} and t_M. In our plots, K_{eff} is either zero (non magnetic, corresponding to dead layers), positive, thus leading to PMA or negative, leading to in-plane anisotropy.

As many parameters are present, I will explain how we have performed the fitting procedure.

First, the dead layer profile is fitted using the polynomial described in equation6.2 which is given by the transition for thin FeCoB thicknesses, between PMA (or in-plane anisotropy in some cases) [†] and the non-magnetic/paramagnetic (PM) region. The shape of the left transition is thus completely given by the dead layer thickness and is not affected by any other parameter.

After optimizing the parameters linked to the dead layer thickness and its variation, we fit the shape of the transition between PMA and in-plane anisotropy by tuning K_s and the two σ. Let us stress here that the shape of this transition is strongly dependent on the shape of the dead layer profile evident from equation 6.4, and therefore it is fitted after the fitting of the dead layer profile. The value of M_s is fixed and is not fitted as it is interrelated to K_s and hence K_{eff} . Indeed, by increasing the M_s and K_s by a factor of 2, we obtained exactly the same map. So we have fixed M_s in our simulations as the variations of parameters on the same wafer is significant even if the real value of M_s and K_s may be a bit different. Further optimization of this model using more appropriate values of M_s and K_s for different systems might be needed in the future to quantify the results.

[†]Note that terms Perpendicular Magnetic Anisotropy (PMA) and Out-of-Plane (OP) anisotropy mean the same and have been used interchangeably. It is not to be confused with paramagnetic zone which is abbreviated as PM.

6.E Study of different HM/FM/MOx systems

I now describe the study of different HM/FM/MOx consisting of wedges of FM and M layer. We employ our phenomenological model described above to understand these systems in greater detail. We have studied two main systems namely: Ta/FeCoB/MOx and Pt/Co/MOx.

6.E.1 Ta/FeCoB/MOx

We study Ta/FeCoB (FeCoB composition is $Fe_{72}Co_8B_{20}$) system with two different top metal oxides: (i) TaOx and (ii) MgO. Both these systems are widely popular in spintronics. For example Ta/FeCoB/MgO is a standard stack for magnetic tunnel junctions (MTJs) for Magnetic Random Access Memory (MRAM) applications and Ta/FeCoB/TaOx is known to host skyrmions for applications in memory and logic devices. Therefore a detailed study of these two systems is of major interest. To study both these systems, a double wedge of FeCoB and top MOx is used. I will first compare the influence of the top metal oxide on shaping the magnetic properties and then the changes produced by annealing on both the systems. I will also use the phenomenological model described above to analyze these samples in greater detail in terms of their dead layers and anisotropy.

Effect of top oxide

Here we see how the top metal oxide plays a major role in determining the magnetic properties of the system in terms of its anisotropy and dead layers.

Ta/FeCoB/TaOx sample has been already introduced in the previous sections. We saw precisely how the dead layer and anisotropy varies as a function of the FeCoB layer thickness as well as the oxidation of the top Ta layer from the remanence map. To recall, we see that the dead layers (paramagnetic zone) arise both on the overoxidized part corresponding to low Ta thickness and on the underoxidized part corresponding to large Ta thickness. The former is due to oxidation of FeCoB and the latter is due to the intermixing of Fe and Ta ions at the interface due to the heavy metal Ta being sputtered on Fe. For lower FeCoB thickness (0.8-1.1 nm), the surface anisotropy dominates giving OP anisotropy/PMA, whereas for higher thicknesses (>1.2 nm), IP anisotropy prevails.

In Ta/FeCoB/MgO, we confirm that the anisotropy and dead layers is not only dependent on the FeCoB thickness but also the oxidation state of the FeCoB/MgO interface[123]. Comparing this stack with Ta/FeCoB/TaOx, we first observe that the dead layer zone is much smaller in the latter case, in particular for the underoxidized region. This can be understood by considering that Mg being lighter damages less FeCoB than Ta when sputtered on top. The OP anisotropy zone is much larger in case of MgO as the top oxide. It suggests the interface quality is better in case of FeCoB/MgO producing less intermixing and lesser dead layers. Further more the increased area of OP anisotropy can be attributed to the crystallinity of MgO.

Effect of annealing

Annealing leads to crystallinity of the sample stack and hence the magnetic properties evolve. I is therefore interesting to compare its effects on different systems. We use the phenomenological

model to visualize the change in the magnetic properties of a system before and after annealing qualitatively. It provides deep insight into the facts such as the improved quality of the interface after annealing, the reduction of dead layers and also the diffusion of certain metal atoms into adjacent layers. Here we present two systems that have been examined before and after annealing.

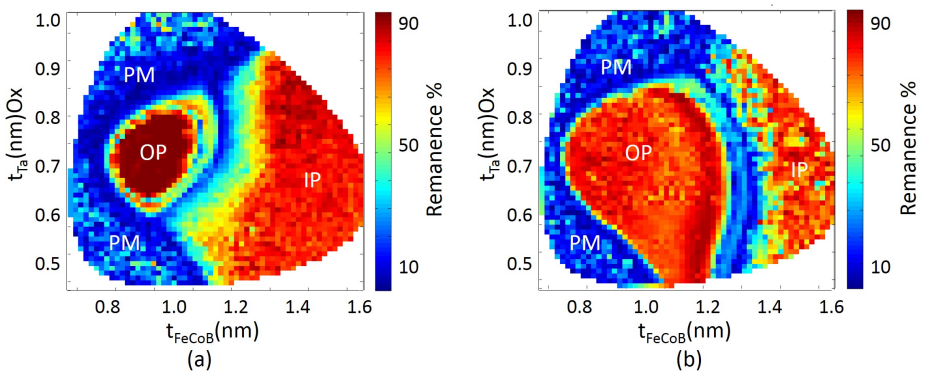

Figure 6.7 – Before (a) and after(b) annealing (225°C for 30 minutes in ultra-high vacuum) remanence maps of Ta/FeCoB/TaOx.

Ta/FeCoB/TaOx sample has been already introduced in the previous sections. We saw precisely how the anisotropy varies as a function of the FeCoB layer thickness as well as the oxidation of the top Ta layer. The sample was then annealed at 225°C for 30 minutes under high vacuum. The annealing conditions for this system had been optimized in earlier experiments, the details of which I will not indulge at this point.

After annealing, the sample is mapped again using the same nanoMOKE setup and remanence map is plotted. On comparing the remanence maps before and after annealing as shown in figure 6.7, we see that the PMA or the OP anisotropy zone has expanded, mainly for the lower thickness of the top Ta. The OP-IP anisotropy transition region is shifted towards higher thickness of the FeCoB (1.3nm) as compared to the un-annealed sample (1.1 nm). This is consistent with the fact that FeCoB becomes crystalline on annealing as compared to being amorphous before leading to an overall increase of PMA. The thickness values of FeCoB corresponding to OP anisotropy is consistent with previous study on this stack[63].

The dead layer region due to the overoxidized part seems to have very slightly reduced which might be due to recovery of more optimally oxidized interface. This can be attributed to the pumping of oxygen caused by Ta on annealing. However we note that the top paramagnetic/dead layer zone does not evolve after annealing. This suggests that annealing has no affect on the dead layer part formed due to the mixing of Fe and Ta atoms : once there is contact between Fe and Ta, it reduces magnetization and annealing does not modify this contact. The reason behind such a behavior can be that Ta being heavy metal when sputtered on FM will damage more the FM than in case of a lighter element for example Mg. If more Ta is sputtered, it damages the FM more (underoxidized region). Also, it is important to note that the dead layer arises also due to the bottom Ta/FeCoB interface, however in this case Fe or Co, which are lighter, are sputtered on heavy Ta and therefore do not cause damage (or very small in amount) as compared to Ta being sputtered on them in underoxidized region.

Now using the model described above we are able to reproduce maps of this system the before and after annealing as represented in figure 6.9 (a) and (b). The dead layer variation before and after annealing is also plotted as shown in figure 6.10(a). We observe that the dead layer in the underoxidized region is exactly the same before and after annealing.

We then extract the anisotropy variation before and after annealing (figure 6.10(b)). We notice a slower drop of anisotropy for overoxidized region after annealing and almost no change for the underoxidized region. This is consistent with the decrease of dead layer thickness and a better crystallinity at FeCoB/TaOx interface. As boron (B) is usually pumped in the adjacent Ta layer in a standard Ta/FeCoB/MgO system, in the case of Ta/FeCoB/TaOx for the underoxidized part, we may infer that B goes to both top and bottom Ta layers thus not improving much the PMA.

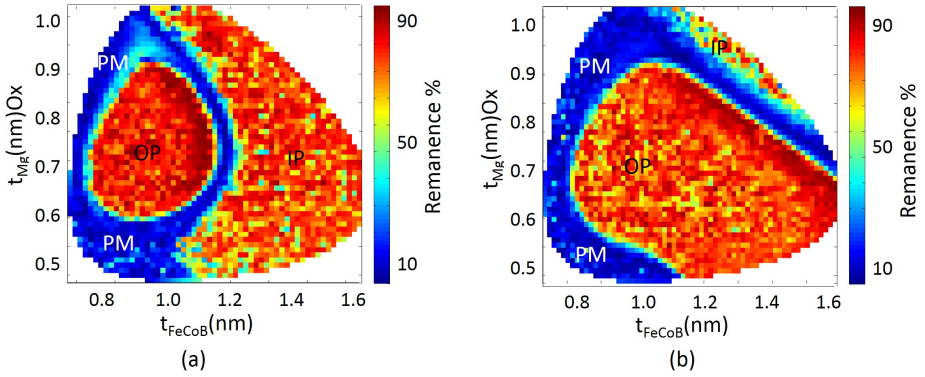

Figure 6.8 – Before (a) and after(b) annealing (250°C for 60 minutes in ultra-high vacuum) remanence maps of Ta/FeCoB/MgO.

A similar study is made for Ta/FeCoB/MgO system. Remanence maps are plotted before and after annealing the sample at 250°C for 1 hour under high vacuum. This annealing condition again has been optimized previously.

From the Remanence maps presented in figure 6.8 it can be seen that after annealing (i) the OP anisotropy zone expands to higher thickness of FeCoB, completely pushing the IP anisotropy zone (ii) and a reduction of dead layer in the overoxidized zone *i.e.* for low Mg thicknesses.

The improvement of OP anisotropy after annealing like in the previous case of Ta/FeCoB/-TaOx indicates the improvement in the crystalline structure of the sample. Moreover since MgO is also expected to have a well defined crystalline structure after annealing, the expansion of the OP anisotropy zone is even larger than in the case of Ta/FeCoB/TaOx system. Both in the befor and after annealing remanence maps we see that for a constant FeCoB, if the MgO thickness is increased beyong a threshold (~0.95 nm) it results in IP anisotropy which has also been observed in literature[123].

The reduction of the dead layers after annealing in the overoxidized part suggests that the oxygen is pumped back from the top Ta upon annealing leading to the recovery of optimally oxidized interface.

The model is then used to reproduce the maps shown in figure 6.9 (c) and (d). The dead layer variations are extracted(figure 6.11(a) and (b) showing a slight increase in value of the minimum dead layer and also mainly in the underoxidized region. In fact minimum dead layer

increase is visible on the after annealing remanence map itself. This could be attributed to a slight shift (1-2 mm) of the sample position placed after annealing during the NanoMOKE scan. However, the dead layer evolution in the underoxidized region suggests that a probable mixing of the Fe and Mg atoms occurs for higher Mg thicknesses after annealing leading to a slight increase of dead layers. We have to be careful with this hypothesis as the transition region on the wafer is relatively close to the edges where all the material properties start to decrease a bit. This however, at least gives an upper bound for dead layers.

The evolution of K_s is however striking. We can see from figure 6.11 (a) and (b) that after annealing the K_s no longer drops for lower Mg thicknesses. This suggests a perfect interface between Fe/MgO which explains the huge expansion of the OP anisotropy zone.

Comparing Ta/FeCoB/TaOx and Ta/FeCoB/MgO, we see two striking differences: (i) the dead layers obtained in the case of Ta/FeCoB/TaOx is much larger than for Ta/FeCoB/MgO. This can be due to the fact that Ta being heavy, when sputtered on Fe or Co causes intermixing whereas Mg being lighter does not. (ii) The OP anisotropy is much wider (almost a factor of 2) for Ta/FeCoB/MgO as compared to Ta/FeCoB/TaOx after annealing. For the optimally oxidized case the transition from OP to IP anisotropy occurs for higher thickness of FeCoB in the case of Ta/FeCo/MgO ($t_{FeCoB} > 1.6nm$) as compared to Ta/FeCoB/TaOx ($t_{FeCoB} > 1.3nm$).

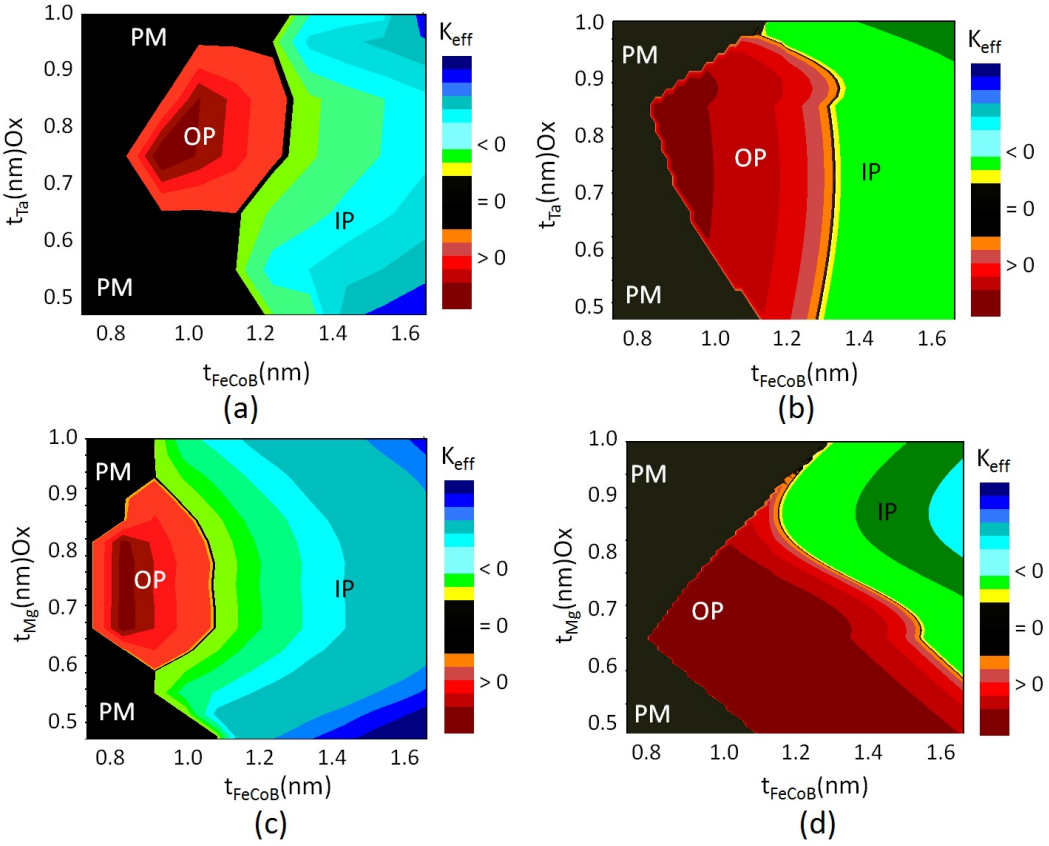

Figure 6.9 – $K_{eff} \times t_{FM}$ simulated maps as a function of FM and MOx layer thickness obtained for Ta/FeCoB/TaOx before(a) and after(b) annealing and in Ta/FeCoB/MgO systems before(c) and after(d) annealing. They have been adjusted with the experimentally obtained respective remanence maps.

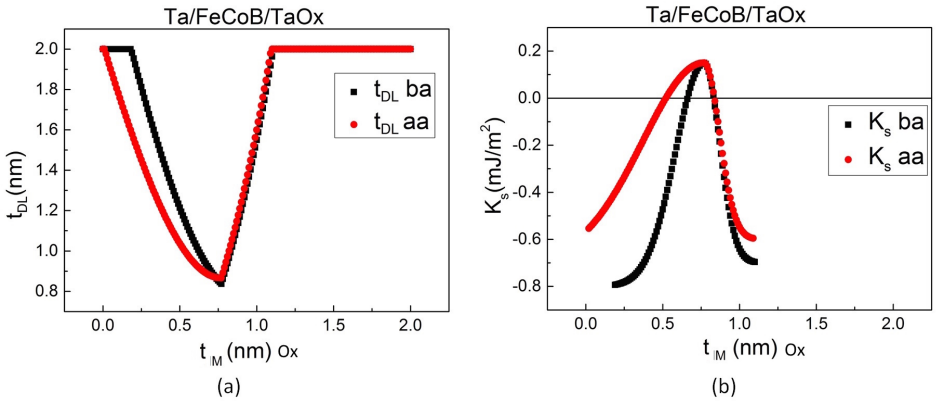

Figure 6.10 – The variation of dead layer t_{DL} and K_s extracted before and after annealing for Ta/FeCoB/TaOx as a function of TaOx (represented as t_{NM}, NM=non metal on the x-axis).

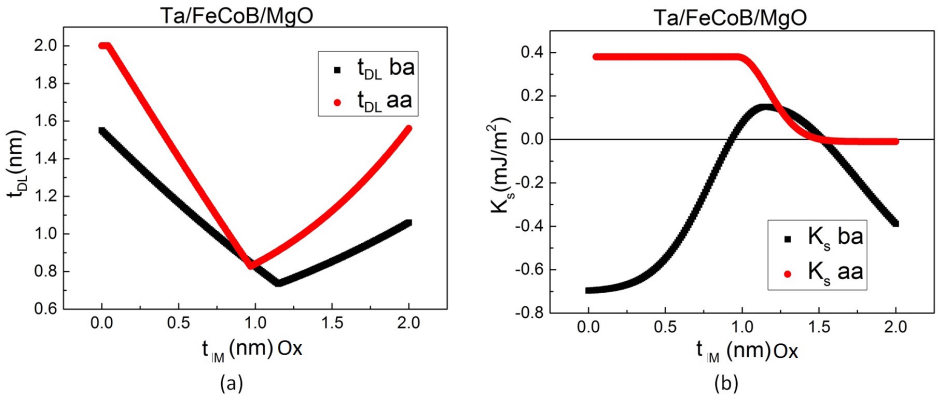

Figure 6.11 – The variation of dead layer t_{DL} and K_s extracted before and after annealing for Ta/FeCoB/MgO as a function of MgO (represented as t_{NM}, NM=non metal on the x-axis).

6.E.2 Pt/Co/MOx

Here we describe how the top oxide layer in the case of HM/FM/MOx system, affects the magnetic properties for the same HM/FM. We compare three systems namely: Pt/Co/AlOx, Pt/Co/MgO and Pt/Co/TaOx. All these samples were prepared by sputtering consisting of a double wedge, *i.e.* a wedge of Co and on top of it a wedge of Al or Mg or Ta in a direction perpendicular to the previous wedge followed by an oxidation step. Natural oxidation was used in the case of Pt/Co/MgO and Pt/Co/TaOx (same as for Ta/FeCoB/MOx systems) whereas plasma oxidation is used in case of Pt/Co/AlOx. These samples were not annealed in order to avoid the inter-diffusion at the Pt/Co interface. MOKE mapping of the three samples were then performed and remanence maps were plotted for each of them.

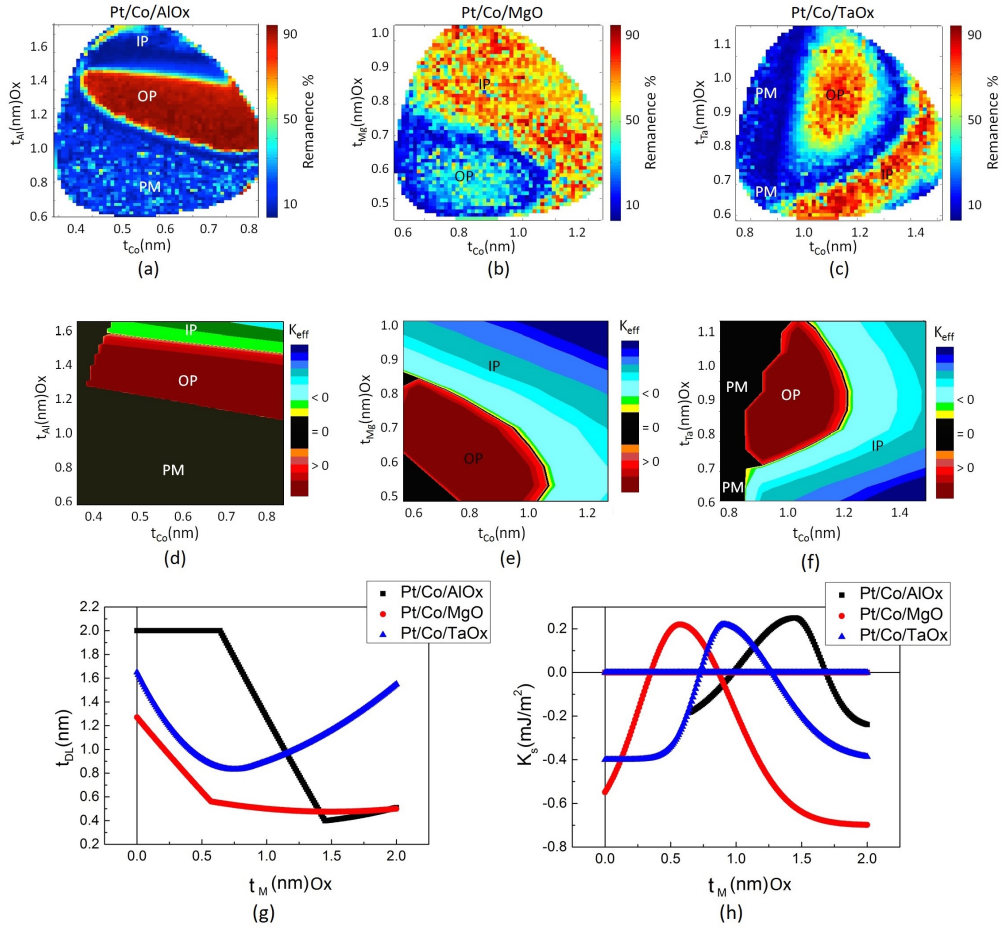

Figure 6.12 – Remanence map obtained from MOKE measurement for Pt/Co/AlOx (a), Pt/Co/MgO (b) and Pt/Co/TaOx (c) sample. The corresponding $K_{eff} \times t_{FM}$ simulated maps as a function of FM and MOx layer thickness obtained for Pt/Co/AlOx (d), Pt/Co/MgO (e) and Pt/Co/TaOx (f) systems. They have been adjusted with the experimentally obtained respective remanence maps.Variation of dead layer t_{DL} (g) and K_s (h) extracted for the three systems as function of the MOx layer thickness (as t_{NM} NM=non magnetic) is also represented.

Dead layer variation

In the case of Pt/Co/AlOx, we observe from the remanence map in figure 6.12 (a) that we have dead layers/ paramagnetic zone over quite a large range of Co thickness (0.4nm to 0.8nm) until the Al on top is thick enough (1 nm). In other words for lower Al thicknesses we can expect that the Co is oxidized hence corresponding to the overoxidized zone which leads to dead layers whereas when Al thicknesses increases the oxidation becomes optimum. This could be due to 'aggressive' oxidation with plasma that makes O atoms penetrate deeper in Co layer. It is also important to note that the dead layer is quite small in the underoxidized region.

In the case of Pt/Co/MgO shown in figure 6.12 (b), firstly we see that the paramagnetic zone or the dead layer zone is almost absent in the thickness range of the two layers, Co:0.6 to 1.2 nm and Mg: 0.5 to 1.0 nm. We can infer that the dead layer zone is probably below this thickness range. As we don't clearly see the PM region (might be due to edges of the wafer), we should be careful in the interpretation here therefore the extraction of the dead layer is an upper limit.

For the remanence map of Pt/Co/TaOx in figure 6.12 (c), we observe that the dead layer zone is large for higher thickness of Ta and below 0.95 nm of Co. It is however smoother than in the case of FeCoB indicating that Fe is more sensitive than Co to the presence of Ta.

The remanence maps of the three systems described above were also fitted using the model. The respective maps are generated consistent with the experimental observation shown figure 6.12(d)(e)(f). The dead layer t_{DL} dependence on MOx thickness is plotted for each case in figure 6.12(g). It can be better visualized with these graphs that In the case of Al, until an optimum oxidation is reached the anisotropy is almost zero resulting in dead layers. On obtaining the optimum the dead layers are drastically reduced.

In the case of MgO, the dead layer increases for smaller Mg thicknesses which indicates the overoxidized case in which Co is oxidized. For larger Mg thickness the dead layer does not increase indicating a perfect interface between Co and MgO. For Pt/Co/TaOx, as expected the dead layer increases for higher Ta thickness corresponding to the underoxidized case indicating an imperfect interface between Co and TaOx when the Co thickness is low and a partial destruction of magnetism due to Ta deposition on Co. For overoxidized region : same slope is observed as the previous two cases.

Anisotropy variation

We see from the remanence map in figure 6.12 (a), that AlOx contributes largely to the PMA in Pt/Co/AlOx system. Within the thickness range of Al ranging from 1.2 nm to 1.4 nm, we get PMA for a wide range of Co thickness. Above a 1.5nm of thickness of Al, *i.e.* an underoxidized zone, IP anisotropy is preferred. Further we see that beyond 1.4 nm thickness of Al, the preferred anisotropy becomes in-plane for almost all the thickness of Co. This trend is similar to what has been observed by Manchon et al. [124] and Rodmacq et al. [125]. However, thickness of Al corresponding to OP anisotropy was lower in their case as the oxidation time was longer than what we have for our samples. Therefore they observed OP anisotropy for lower Al thickness due to optimally oxidized Pt/AlOx interface whereas in our case the range of Al thickness to observe OP anisotropy shifted to higher values. Moreover below a certain Al thickness, i.e overoxidized case when the Co gets oxidize too, we observe a decrease of OP anisotropy which

finally leads to paramagnetic state which is in agreement with Manchon et al., by contrast[125] report that the anisotropy evolves from being reduced OP to IP anisotropy over time for the same case. This can be related to the motion of the oxygen ions through the interface which brings this change but it is still unclear.

The overall behavior of the dependence of anisotropy has been explained by Manchon et al.[124] on the basis of interfacial oxidation. In the underoxidized case, the bonds at the Co/AlOx interface are primarily Co-Al and the magnetization of Co lies in-plane. The onset of PMA is governed by the replacement of Co-Al by Co-O, which corresponds to the optimum oxidation state and leads to positive K_s. Finally for overoxidized case the Co gets oxidized through penetration of oxygen atoms through the grain boundaries decreasing the exchange coupling between the magnetic grains and hence the overall anisotropy.

In the case of Pt/Co/MgO in figure 6.12 (b) the out-of-plane to in-plane anisotropy transition is rather diagonal across the remanence map. This means that for the same thickness of Co lets say 0.8 nm, we can get PMA when the Mg thickness is between 0.5 to 0.7 nm whereas on exceeding this thickness range of Mg, the anisotropy becomes in-plane. Similarly for 0.6 nm of Mg, we can have PMA within 0.6 to 1.0 nm of Co and in-plane anisotropy above that. This two fold dependence of anisotropy on the FM and MOx layer thickness is extremely important to keep in mind in order to optimize this system for various applications, for instance for skyrmions[65].

For Pt/Co/TaOx, the picture is quite different(figure 6.12 (c)). Here we observe that for low thicknesses of top Ta (0.6 to 0.8 nm), the anisotropy preferred is in-plane over wide thickness range of Co. Whereas when the top Ta thickness increases then PMA is preferred for lower Co thicknesses (1-1.3 nm) beyond which it becomes in-plane. Here we see that within a certain thickness range of Ta: 0.8 to 1.1 nm which also corresponds to the optimally oxidized zone, the anisotropy is mainly dependent on the Co thickness going from out-of-plane for lower thicknesses and in-plane for higher thicknesses.

We use our model to extract the interface anisotropy K_s variation as described before as a function of MOx thickness in figure 6.12(h). Here we first observe that the optimum interface anisotropy is obtained at different thicknesses of MOx which also corresponds to the optimally oxidized state of the MOx. The interface anisotropy decreases on moving away from the corresponding optimally oxidized MOx thickness. The drop of interface anisotropy on the left part of the curve that is for lower MOx thicknesses corresponds to the overoxidized case leading to dead layers and hence paramagnetic zone. The drop on the right hand side on the other hand indicates the underoxidized case where the preferred anisotropy becomes in-plane in general but can also be paramagnetic like in the case of Pt/Co/TaOx. Such a behavior of the interface anisotropy was also observed by Manchon et al.. The drop of anisotropy for lower M thickness also means that the interface is no more Co/MOx but Co/CoO (it is not yet paramagnetic as we still have a square loop). This was not so obvious as it is again an interface with an oxide. So the M is important for interfacial anisotropy The shape of K_s for all three cases is surprisingly similar (shift of optimum thickness due to type of oxidation and maybe oxygen content of MOx *i.e.* stoichiometry) and different amplitudes (not surprising as the materials are different).

This material study is still being pursued to formulate quantitative results. For the model, we need to optimize the fitting of the dead layer by choosing a Gaussian function which makes the fit smoother. We also need to clearly distinguish between the real and apparent dead layers

and the variation of M_s and k_s along them to present more realistic systems. The appropriate value of the M_s needs to be used for each HM/FM/MOx system which would enable us to extract the corresponding values of K_s and K_{eff}. Furthermore, we plan to add the DMI energy and the calculation of domain wall energy to the model. The aim is to be able to visualize the areas of low domain wall energy on the reconstructed map of effective anisotropy which would hint at the possible skyrmionic zones (skyrmions can be nucleated in low domain wall energy zones).

6.F Conclusion and Perspectives

We hence see that the choice of FM, or the top MOx and their respective thicknesses and interfacial oxidation state, shapes the magnetic energy contours in HM/FM/MOx system. It is in terms of the transition regions from out-of-plane anisotropy to paramagnetic or out-of-plane to in-plane transition for their corresponding thicknesses. From a simple model constructed on these ideas we could determine qualitatively how annealing affects the interface anisotropy and the appearance of dead layers in the system in the case of Ta/FeCoB/TaOx and Ta/FeCoB/MgO. We could further compare several systems like Pt/Co/AlOx, Pt/Co/MgO and Pt/Co/TaOx on the basis of the top oxide layer in terms of anisotropy and dead layer profile variations. This method provides a way to study in detail all the magnetic parameters and their mutual dependence for several systems.

This material study is still being pursued to formulate quantitative results. For the model, we need to optimize the fitting of the dead layer by choosing a Gaussian function which makes the fit smoother. We also need to clearly distinguish between the extrapolated and apparent dead layers and the variation of M_s and k_s along them to present more realistic systems. The appropriate value of the M_s needs to be used for each HM/FM/MOx system which would enable us to extract the corresponding values of K_s and K_{eff}. Furthermore, we plan to add the DMI energy and the calculation of domain wall energy to the model. The aim is to be able to visualize the areas of low domain wall energy on the reconstructed map of effective anisotropy which would hint at the possible skyrmionic zones (skyrmions can be nucleated in low domain wall energy zones). The next chapter deals with locating the stable skyrmionic zones in Ta/FeCoB/TaOx system as a function of the thicknesses of FeCoB and TaOx.

7

Observation of magnetic skyrmions

7.A Introduction

In the previous chapter we saw how the magnetic properties evolve as a function of layer thicknesses in different HM/FM/MOx systems. We also located the low domain wall energy zones in these double wedges where we expect to stabilize skyrmion phases. In this chapter, the experimental observation of skyrmion bubbles in Ta/FeCoB/TaOx system using Polar Magneto-Optic Kerr Effect Microscopy (p-MOKE) is presented. It is detailed how the manipulation of material parameters lead to stable skyrmion phases. The skyrmions are observed in different transition regions namely: out-of-plane anisotropy to paramagnetic zone and out-of-plane anisotropy to in-plane anisotropy, as a function of the FeCoB and TaOx thicknesses. A brief study of their motion is also demonstrated.

Skyrmions are chiral magnetic textures being vastly explored currently for their potential use in memory and logic devices. They were discovered initially in bulk non centro-symmetric crystals like MnSi and FeGe at low temperature[59, 60]. They have recently been observed at room temperature in thin trilayer systems consisting of a heavy metal (HM), a ferromagnet (FM) and metal oxide (MOx) like Ta/FeCoB/TaOx[63], Pt/CoFeB/MgO[64] and Pt/Co/MgO[65]. In these systems, an antisymmetric exchange called the interfacial Dzyaloshinskii-Moriya interaction (DMI) arises due to broken inversion symmetry and spin orbit interaction. This interaction competes with other magnetic interactions like exchange, dipolar, anisotropy and Zeeman to stabilize skyrmions. However observing magnetic skyrmions at room temperature is not straightforward. One way is to form them from chiral stripe domains by using geometrical

constrictions and flowing spatially non uniform currents[63]. Another way is to nucleate them using solely the interface properties. Several ways exist to maneuver the interface which can be instrumental in stabilizing skyrmion phases. Some studies have shown to engineer the interface using thin insertions of heavy metal in between the ferromagnet and insulator[66]. The oxidation state of the insulator on the top, which is often a metal oxide, has also been seen to affect the perpendicular magnetic anisotropy and DMI[116] which can directly lead to tuning of the interface for stable skyrmion phase.

We investigate in detail a stable energy landscape for skyrmion phase by studying the magnetic properties as a function of ferromagnetic and insulator layer thickness and its oxidation. In order to access skyrmionic bubble phase in thin films, the domain wall energy given by $\sigma_W = 4\sqrt{AK_{eff}} - \pi \mid D \mid$[64, 126] with K_{eff} the effective anisotropy ($K_{eff} = K_s/t - 1/2\mu_0 M_s^2$ where K_s is the surface anisotropy) and A the exchange stiffness, should be low *i.e.* either K_{eff} is low with no DMI or the DMI coefficient is large enough to nearly compensate anisotropy contribution in σ_W. To achieve this, a fine tuning of the layer thicknesses, stoichiometry and interface quality is necessary.

7.B Tuning double wedges of FeCoB and TaOx layers in Ta/FeCoB/-TaOx for skyrmion nucleation

We concentrate on Ta/FeCoB/TaOx trilayer for the rest of our study as it offers several material parameters to play with in order to tune the interfacial properties for skyrmion nucleation.

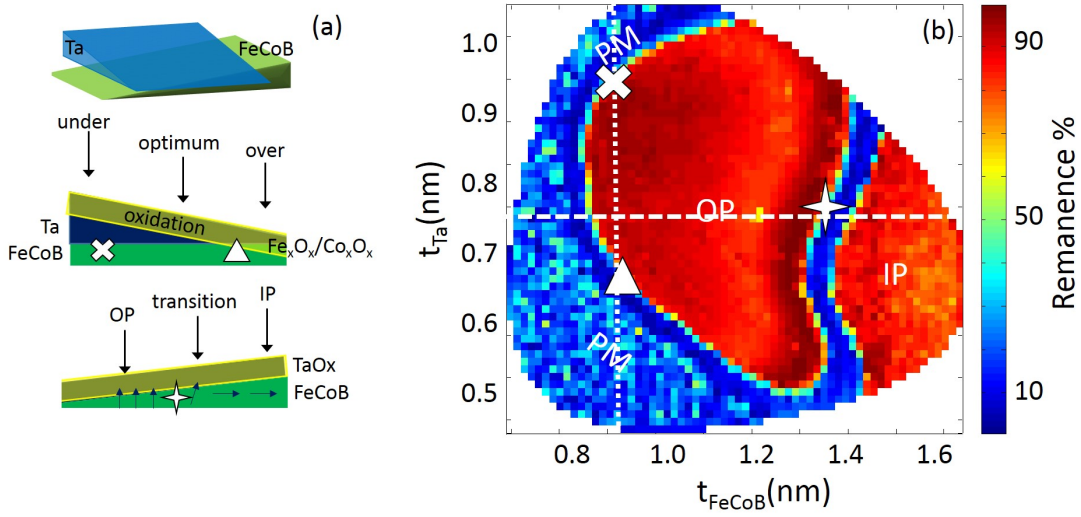

Figure 7.1 – (a) Double wedge system: a wedge of Ta deposited perpendicular to the wedge of FeCoB. This is followed by oxidation which gives optimally oxidized, underoxidized and overoxidized Ta zones.(b) Remanence map of Ta/FeCoB/TaOx obtained by MOKE. Red indicates high remanence and blue low remanence. The shape of the hysteresis loops reveals the paramagnetic, perpendicularly magnetized and in plane magnetized zones as demonstrated by schematic on the left. The positions marked by cross, triangle and star represent the zones where the skyrmion phase is stable.

7.B.1 Sample details

To study this system, a double wedge deposition technique (shown in figure 7.1a) by sputtering was used. On a 100mm Si wafer substrate with 500nm-thick thermally oxidized SiO_2, first un underlayer of Ta (3nm) is deposited. This is followed by deposition of FeCoB wedge (0.59-1.69nm) using off-axis deposition technique described in chapter 5. Perpendicular to this wedge, another deposition of Ta wedge($0.45 - 1.04\mathrm{nm}$) is carried out followed by natural oxidation step (oxygen pressure $150\mathrm{mbar}$ for $10\mathrm{s}$). The oxidation of the Ta wedge leads to underoxidized and overoxidized Ta zones on the opposite edges apart from the optimal oxidation in the center as shown in figure 7.1a. For surface protection of TaOx, a thin layer of Al(0.4nm)is deposited after it. This double wedge provides access to all combinations of thicknesses of FeCoB and top Ta. The sample was further annealed at 225°C for 30 minutes to improve perpendicular magnetic anisotropy (PMA).

7.B.2 Characterizing magnetic properties of Ta/FeCoB/TaOx trilayer by MOKE magnetometry

First, in order to map the magnetic properties of the double wedged sample, Magneto-optic Kerr effect(MOKE) magnetometry was performed. MOKE magnetometer, with a focused laser (spot of $300\mu\mathrm{m}$), was used to characterize every mm^2 of the sample. Due to its 45° light incidence and a 2D applied magnetic field, our MOKE setup (described in chapter 5) is sensitive to both out-of-plane and in-plane components of magnetization. The shape of the hysteresis loop obtained at every measured point, reveals the anisotropy favored at that point.

Transition regions along the FeCoB and TaOx double wedge

Perpendicular Magnetic Anisotropy to Paramagnetic state transition A map of the remanence (Fig 7.1b) shows that the perpendicular magnetic anisotropy region is limited to $0.9 - 1.3\mathrm{nm}$ of FeCoB, above which in-plane anisotropy is favored energetically. For FeCoB thicknesses in the range $0.85 - 1.2\mathrm{nm}$, we observe paramagnetic regions (PM) along the two extremes of the top Ta wedge that give zero remanence and noisy signal. For instance, if we follow the dotted line of Fig 7.1b, corresponding to $t_{FeCoB} \approx 0.95\mathrm{nm}$, PM region is obtained for $t_{Ta} < 0.65\mathrm{nm}$ or $t_{Ta} > 0.92\mathrm{nm}$. For low Ta thickness, the surplus of oxygen, not trapped in TaOx layer, will reach FeCoB and partially oxidize the ferromagnet. In this overoxidized region, the ferromagnetic layer thickness is thus reduced and it leads to lower Curie temperature (T_C). When T_C crosses room temperature, the layer thus becomes paramagnetic. This is similar to the behavior observed in other systems such as Pt/Co/AlOx[69]. Also for high Ta thicknesses, we observe a paramagnetic region. In this case, it means that TaOx is partially replaced by Ta at the top FeCoB interface. Ta at the interface with FeCoB leads to dead layer (of the order of 0.3nm) and it is supported by our ab-initio calculations (done by M. Chshiev) that show that the magnetization of Fe is reduced when in contact with Ta at the interface. Therefore we can see that oxidation of the Ta layer on top of FeCoB largely affects the anisotropy and can be use to tune the same.

Perpendicular Magnetic Anisotropy to In-Plane Anisotropy state transition On the remanence map of figure 7.1b we also observe another region with zero remanence, but in this case, it is not noisy as in the case of the paramagnetic region. It corresponds to the out-of-plane (also called Perpendicular Magnetic Anisotropy) to in-plane anisotropy transition when the FeCoB thickness increases. Therefore if we follow the horizontal dashed line along the sample as shown in figure 7.1, we encounter paramagnetic zone, out-of-plane and subsequently in-plane anisotropy zones.

Phenomenological Model to interpret the variation of magnetic properties A phenomenological model was developed (explained in Chapter 6) to qualitatively interpret the variation of the magnetic properties like perpendicular magnetic anisotropy, dead layer profile, surface anisotropy (K_s) and effective anisotropy (K_{eff}) across the sample. Our model manages to reproduce qualitatively the experimental remanence map. It shows for instance that annealing mainly improves the underoxidized region which leads to reduction of dead layers and increase of surface anisotropy. Through this model we can deduce that the transition regions are the zones with low domain wall energy. Therefore we can expect easy nucleation of skyrmions at these sites.

7.B.3 Study of magnetic domain configuration by p-MOKE microscopy

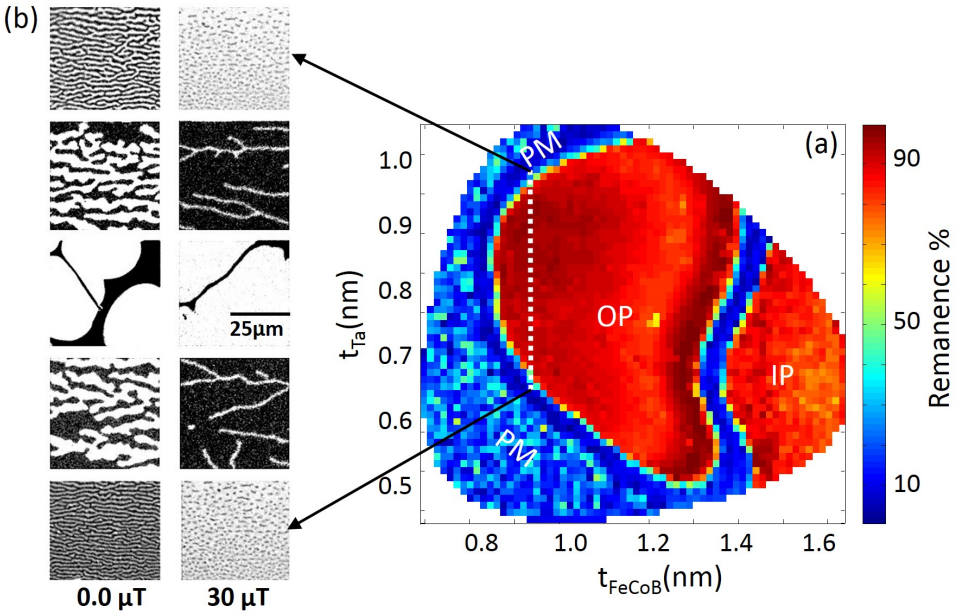

Figure 7.2 – Polar Kerr image of magnetic domains along the TaOx wedge. (a) The demagnetized stripe domains at 0µT (left) and their transformation on applying out of plane magnetic field of at 30µT (right) corresponding to the Ta thickness marked by the white dotted line in the (b) remanenance map of the Ta/FeCoB/TaOx double wedge obtained by MOKE magnetometry.

Having an idea about the possible zones of transition from the MOKE mapping, we then performed p-MOKE microscopy measurements to study the magnetic domain configuration and possible skyrmion nucleation sites. In the optimally oxidized Ta zone, the PMA is high and hence in the absence of magnetic field large domains are energetically stable. The magnetization reversal on the application of out of plane magnetic field is dominated by domain wall propagation mechanism. The evolution of the domain pattern from 0μT to 30μT along the top Ta wedge is shown in figure 7.2.

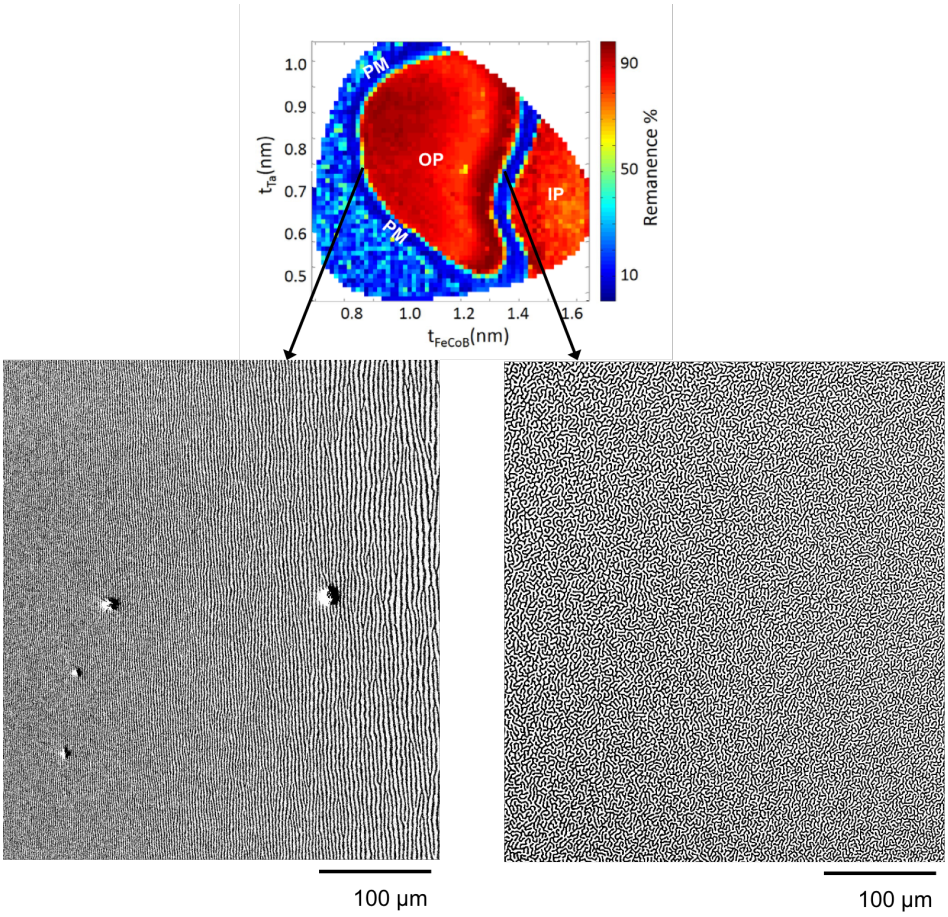

Figure 7.3 – P-MOKE images of two types of demagnetized domain configuration located at two transition zone. On the left: stripe like domains oriented along their length perpendicular to the out-of-plane anisotropy to paramagnetic transition as shown in the remanence map above, right: Labyrinthine domains at the out-of-plane to in-plane anisotropy transition

7.B.4 Skyrmion bubbles in Perpendicular Magnetic Anisotropy to Paramagnetic state transition region

As we move towards the out-of-plane to paramagnetic transition zone, the size of the domains at zero field reduces to become stripes. In fact these stripes correspond to a thermally demagnetized state. It occurs due to low domain wall energy on account of lowering of anisotropy and saturation magnetization such that the nucleation energy of domains is in the order of thermal energy at room temperature. The stripe like domains are observed to be oriented along the

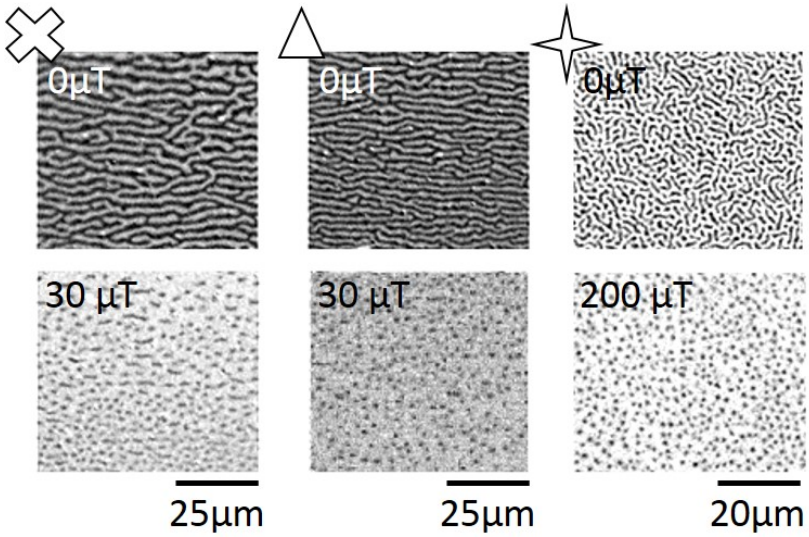

Figure 7.4 – Polar Kerr image of skyrmionic bubbles in the different transition zones. Left: the demagnetized stripe domains at 0μT (above) and the skyrmionic bubbles at 30μT (below) in the transition from out-of-plane to paramagnetic zone where the top Ta is underoxidized. Middle: the demagnetized stripe domains at 0μT (above) and the skyrmionic bubbles at 30μT (below) in the transition from out-of-plane to paramagnetic zone where the top Ta is overoxidized. Right: the demagnetized labyrinthine domains at 0μT (above) and the skyrmionic bubbles at 200μT (below) in the transition from out-of-plane to in-plane anisotropy zone. The symbols above the images (cross, triangle and star) correspond to the points on the double wedge shown in figure 7.1.

frontier of the out of plane to paramagnetic transition zone. Since the magnetic parameters like M_s (thus T_c) and K_s drop abruptly in a direction perpendicular to this transition zone, the stripes are elongated along the direction where the variation of these parameters is less pronounced : see figure 7.3. On the application of a small out of plane magnetic field, a skyrmionic bubble phase is seen. The Zeeman energy in this case balances out the other interactions and the presence of DMI leads to a stable skyrmion phase. These bubbles appear quite isolated and non interacting with each other. Their motion under current is quite uniform as described in the following sections. The value of DMI in this zone was measured by BLS and was found to be $0.2 mJ/m^2$ which is consistent with the values in the literature for this system[63]. On further increasing the magnetic field, a uniformly magnetized state becomes favorable. Figure 7.5 shows the hysteresis cycle measured in this zone and the corresponding p-MOKE images at different applied magnetic field.

Motion of Skyrmionic bubbles

To qualitatively observe the motion of the bubbles under applied current, we used conducting tips integrated with the p-MOKE setup. An out-of-plane magnetic field was applied to stabilize the bubbles while observing their motion under current. The bubbles formed in the out-of-plane anisotropy to paramagnetic transition zone move uniformly along the current flow *i.e.* against the electron flow indicated in figure 7.6. The uniform motion of these bubbles under applied current by spin-orbit torques confirms their non trivial topology and hence their skyrmionic

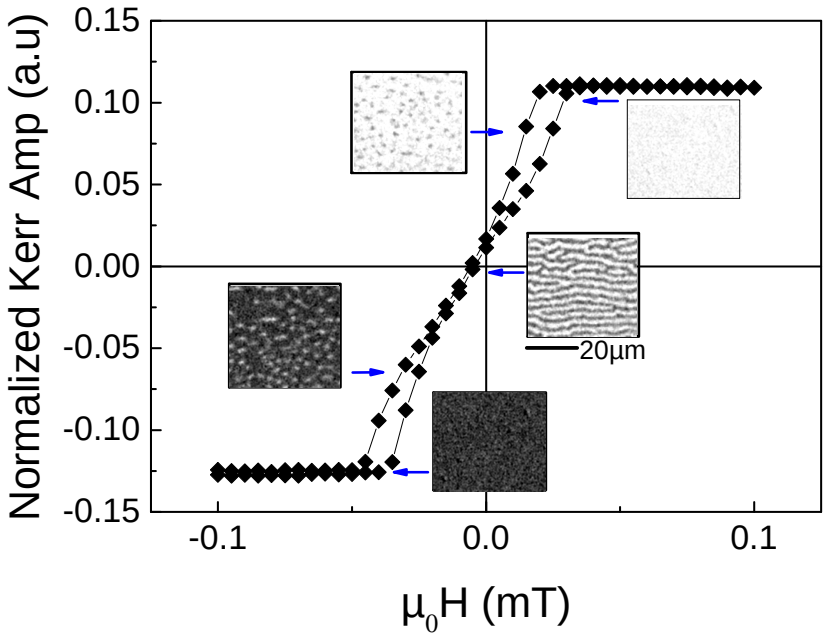

Figure 7.5 – Hysteresis loop and the corresponding images obtained by p-MOKE in the out-of-plane to paramagnetic transition zone. At 0 magnetic field, demagnetized stripe domains are observed. On increasing (or decreasing) the field, a stable skyrmionic bubble phase appears. White contrast represents +z direction and black vice versa. On further increasing (or decreasing) the field a saturated ferromagnetic state is obtained.

nature. In fact when the domain walls are chiral Néel type, *i.e.* the magnetization always rotates clockwise (or anticlockwise depending on the sign of DMI), the torque changes sign from one edge of the bubble to the other. As both magnetization inside the wall and torque change sign on opposite edges of the bubble, it results in a motion of the edges in the same direction, which thus leads to a uniform motion of the bubble, without distortion. To make a quantitative study of the motion of bubbles under current, we used UV lithography and etching to pattern Hall crosses on the Ta/FeCoB/TaOx trilayer in the out-of-plane to paramagnetic transition zone where the motion was observed to be quite uniform. The size of the contact pad is 150μm. A constant out-of-plane magnetic field of 30μT is applied to form the bubbles. A DC current of 0.11 mA (leading to a current density of $2 \times 10^8 A/m^2$ in the 150μm pad) is applied between the contact pads so that it flows in the Ta/FeCoB metallic bilayer. A velocity of $\approx 20\mu m/s$ is obtained which is similar to the study by Jiang et al. [63].

7.B.5 Skyrmion bubbles in Perpendicular Magnetic Anisotropy to In Plane Anisotropy state transition region

The other transition zone as mentioned above is between the out of plane and in plane anisotropy regions along the FeCoB thickness. In this transition zone, a demagnetized domain structure prevails too at zero field. However in this case the domain structure is isotropic labyrinthine like in appearance. The FeCoB is thicker in this region and hence the overoxidized zone is reduced. The M_s remains therefore unaffected. The magnetic properties are nearly uniform in both the horizontal (along FeCoB wedge) and vertical (along TaOx wedge) directions. This can

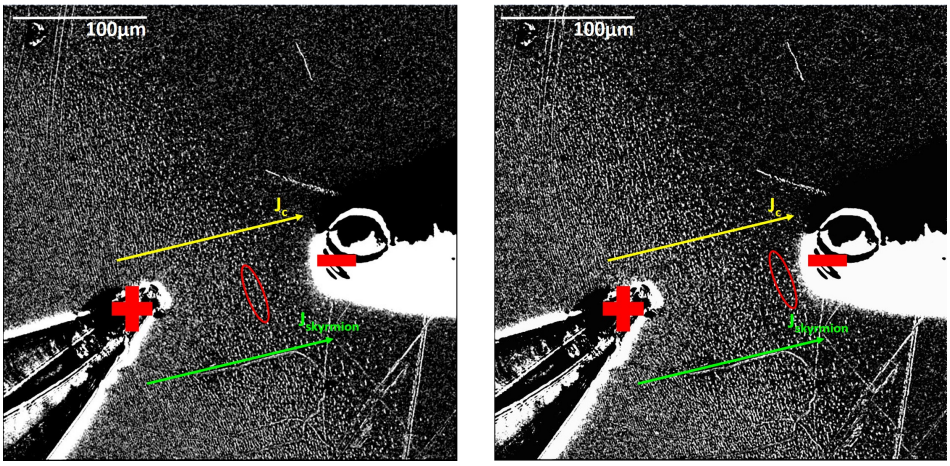

Figure 7.6 – Polar Kerr image of skyrmionic bubbles in the out-of-plane to paramagnetic transition zone under applied current. The tips used for applying current are visible in the image with the indicated polarity. The arrows indicate the direction of current flow and skyrmion flow. The two images on the left and right are successively taken under applied current in the interval of 2 seconds respectively. The motion of skyrmionic bubbles in this zone is quite uniform and free from pinning or distortion.

be the reason that leads to uniform labyrinthine like demagnetized domain structure as there is no preferred sense of orientation as compared to the stripes in the out-of-plane to paramagnetic transition zone, as shown in figure 7.3. Application of a small out of plane magnetic field stabilizes skyrmionic bubble state for the reasons described in the previous section. However contrary to the skyrmionic bubbles in the region of out of plane to paramagnetic transition, they appear in a more lattice like formation. This difference is also observed in their motion under current which is described in the next section.

Motion of Skyrmionic bubbles

The motion of the bubbles formed in the out-of-plane to in-plane anisotropy transition region seems to be dominated by pinning. It can be seen in the figure 7.7 that on the application of current, the bubbles elongate. The video acquired of the motion reveals that some bubbles demonstrate successive elongation and contraction and move forward in the same direction which would indicate a homochiral nature. Some however remain pinned, some disappear and some expand continuously. As the interfacial DMI is dependent on the thickness of FeCoB, it might be lower in this zone owing to thicker FeCoB. This would lead to the DMI being lower than the critical value to stabilize perfect Néel type chiral skyrmions. Therefore we have to still investigate in detail this type of motion of bubbles to conjecture if they are chiral or not.

7.B.6 Analytical Model to explain the stable skyrmionic bubble zones

We use the analytical model of isolated bubble developed in ref Schott et al. to calculate its energy relative to the saturated state. This model incorporates the contributions from: dipolar, exchange, anisotropy, Zeeman and DMI energies as a function of the bubble diameter. The

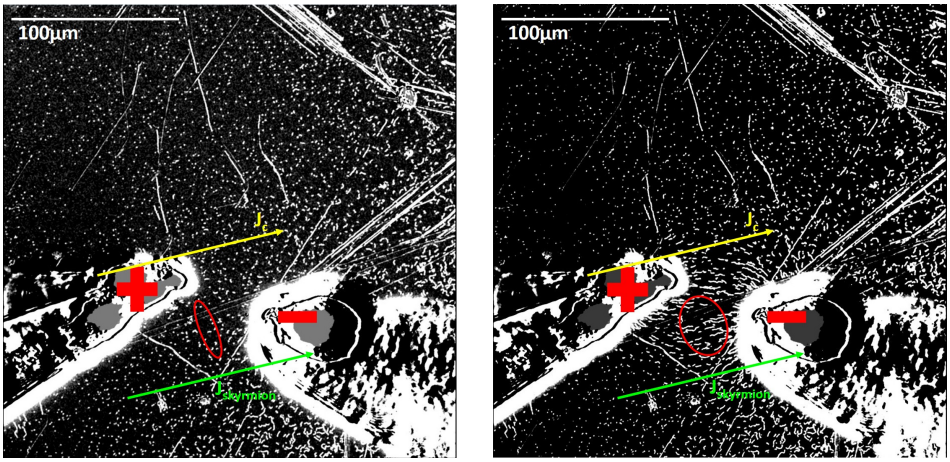

Figure 7.7 – Polar Kerr image of skyrmionic bubbles in the out-of-plane to in-plane anisotropy transition zone under applied current. The tips used for applying current are visible in the image with the indicated polarity. The arrows indicate the direction of current flow and skyrmion flow. The two images on the left and right are successively taken under applied current within the interval of 2 seconds respectively. We see that the most of the bubbles get elongated along the direction of the current. The video obtained from this motion shows that some of them move following successive expansion and contraction along the current direction. It cannot be concluded if they are chiral or not. This is contrary to what we observe in the case out-of-plane to paramagnetic zone where the motion is uniform free from distortion indicating homochirality.

energy of an individual bubble relative to the saturated state can be written as:

$$\delta E_{sb}(R, t, M_s, \sigma_W) = \sigma_W t 2\pi R + 2\mu_0 M_s H t \pi R^2 - \mu_0 M_s^2 \pi t^3 I(d) \tag{7.1}$$

where σ_W is the domain wall energy, t is the layer thickness, R is the bubble radius, M_s is the saturation magnetization, $\mu_0 H$ is the applied magnetic field, and I(d) is the stray field energy gain where $d = 2R/t$ (details in ref Schott et al.[69]). Here the DMI is included in the domain wall energy. Any inhomogeneities in domain wall structure or any non circular shape domain is thus not taken into account. Here the objective is to investigate whether a stable energy minima for the bubble state exists for the set of parameters extracted at different transition regions. In the cases of under or overoxidation, a lower thickness, D_s, K_s and M_s lead to a bubble with a diameter of 1.8μ m. In the case of the OP to IP transition, all these parameters are higher except the DMI value and lead to a minimum of energy for a 2.2μ m diameter stable bubble. The total energy is calculated and compared with the thermal energy ($k_B T$) to estimate the thermal activation barrier which is plot in figure 7.8. We can see clearly that the nucleation energy barrier for the skyrmion bubbles in the out-of-plane to in-plane anisotropy transition zone ($t_{FeCoB} = 0.9nm$) is higher than that for out-of-plane to paramagnetic transition region($t_{FeCoB} = 0.6nm$). The table 8.2 summarizes the parameters used for the analytical calculation. We thus conclude from these calculations that a stable energy minima exists for a skyrmionic bubble for both the sets of parameters confirming the experimental observations.

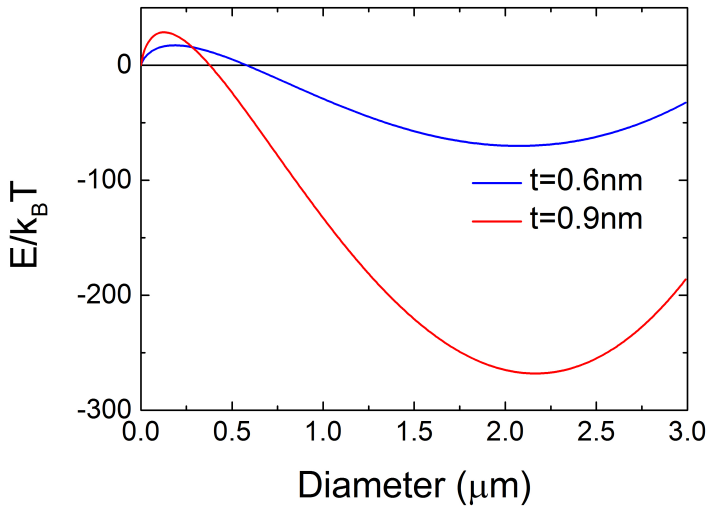

Figure 7.8 – Analytical model: variation of the energy difference between the bubble state and the saturated state as a function of the bubble diameter. Dipolar, anisotropy, exchange, Zeeman and DMI energies have been taken into account. The magnetic parameters used for the two curves are the ones for the bubble zone in the transition from (i) out-of-plane to paramagnetic zone and in the transition from (ii) out-of-plane to in-plane anisotropy zone. In both cases, a energy minima for a bubble exists.

M_s (MA/m)	K_s (mJ/m^2)	D_s (fJ/m)	A (pJ/m)	t (nm)	$\mu_0 H$ (mT)
Analytical model					
0.98	0.374	+120.25	12	0.6	0.3
1.0	0.605	-91.2	12	0.9	0.5

Table 7.1 – Parameters used for analytical model.

7.C Conclusion

In this chapter we saw how the different interfacial magnetic properties vary as a function of FeCoB layer thickness and top Ta layer thickness and its oxidation state. A delicate balance between these result in the formation of skyrmionic bubbles on the application of small out of plane magnetic field. There are two distinct regions where skyrmions are formed (i) near the out-of-plane to paramagnetic transition and (ii) near out-of-plane to in-plane transition. Their observed motion in these two regions is quite different. The skyrmion bubbles in the out-of-plane to paramagnetic transition zones move uniformly in the direction of applied current confirming their homochirality. Whereas, the motion of bubbles in the out-of-plane to in-plane transition zone is non-uniform. Some of them elongate and contract moving in the direction of current while some remain pinned or disappear. We therefore cannot conclude if they are chiral.

In the next chapter we explore the change in the interfacial magnetic properties and hence of skyrmions in the out-of-plane to paramagnetic transition zone (which we found to be homochiral) as a function of applied electric field.

8

Electric field effect on Ta/FeCoB/TaOx systems

8.A Introduction

Electric field effect is now foreseen to be ubiquitously employed to build energy efficient and versatile spintronic devices. Voltage gating offers a dynamic control of the interfacial magnetic properties that has been proposed to be useful for write operations in Magnetic Tunnel Junctions (MTJ)[106, 107] and to tune the sensitivity and detectable field range in magnetic sensors. More recently in thin film systems consisting of a heavy metal/ferromagnet/insulator heterostructures, electric field induced manipulation of magnetic skyrmions[59, 60] has been demonstrated which is even more promising for the envisioned next generation skyrmion based memory and logic devices[69, 71]. In these studies the voltage induced modulations have been mainly ascribed to changes in magnetic anisotropy and saturation magnetization. However, the effect of electric field on the antisymmetric exchange known as interfacial Dzyaloshinskii Moriya interactions (DMI)[127] has not been clearly addressed. The DMI has a fundamental role in stabilizing the skyrmions and also determines their chirality. Therefore DMI control through voltage would directly affect the size and chirality of skyrmions and their velocity under applied current. This would establish an unprecedented control over skyrmions and chiral domain walls and could lead to novel spin-orbitronic devices.

We therefore focused our experiments on addressing this aspect. We chose to study Ta/FeCoB/TaOx for this purpose which is known to host magnetic skyrmions. We performed Brillouin

Light Spectroscopy (BLS) measurements to directly determine the changes in the interfacial DMI of this system as a function of applied electric field. We further performed polar Magneto-optic Kerr Effect (p-MOKE) measurements on the same sample to highlight the time scale effects of the electric field on DMI and other magnetic properties simultaneously. Micromagnetic simulations were then performed using the experimentally obtained parameters to give a deeper insight into the internal structure of skyrmions expected at different voltages as a result of the change in the magnetic properties.

The BLS measurements were performed in collaboration with M. Belmeguenai and Yves Roussigné at LSPM in Université Paris 13. I actively participated in the experiments. I also prepared the setup to apply the electric field for BLS measurements under voltage.

The micromagnetic simulations were done by Roméo Juge in the group of Olivier Boulle at Spintec. I actively participated in the simulations and the discussion involved. I also provided the required magnetic parameters and their evolution under electric field obtained experimentally for the simulations.

8.B Electric Field Effect on DMI: Brillouin Light Spectroscopy (BLS) measurements

8.B.1 Experimental setup and configurations

BLS is a technique which is known to give a direct access to the interfacial DMI through frequency shifts of oppositely propagating spin waves (described in chapter 5). We prepared our samples for BLS measurements under electric field by depositing thick insulating oxide followed by patterning of transparent through lithography (described in chapter 5). Polar MOKE images in figure 8.1b shows the demagnetized stripe domains (at $0\mu T$)and skyrmionic bubbles (at $30\mu T$) under the electrode. It is this electrode that is connected to a voltage source. It is important to note is that we chose the underoxidized TaOx zone of our sample for the electric field study (different zones and their characteristics are described in the previous chapter 7).

The schematic setup of the experiment is shown in figure 8.1a. A constant magnetic field of 300 mT is applied perpendicular to the plane of incidence which is the plane containing the incident and reflected laser beam, allowing the probing of spin waves propagating in the plane perpendicular to the applied magnetic field in the Damon-Eshbach (DE) geometry, as represented in fig 8.1a. The applied magnetic field $\mu_0 H$ is above the saturation field of the sample as determined from magnetometry loops. The frequency shift in the Stokes and Anti-Stokes resonances is analyzed using a 2x3 Fabry-Perot interferometer (3-300 GHz) and is calculated by

$$\Delta f = | f_S | - | f_{AS} | \tag{8.1}$$

Calibrations were done to remove any offset[128] by measuring BLS spectrum under both $\pm\mu_0 H$. The laser spot of $100\mu m$ in diameter was focused on the electrode which is connected to the voltage source. The length of the probed spin wave vector is given by $k_{SW} = 4\pi \sin(\theta_{inc})/\lambda$ where $\theta_{inc} = 60^\circ$ is the angle of incidence and $\lambda = 532$ nm the wavelength of the incident laser.

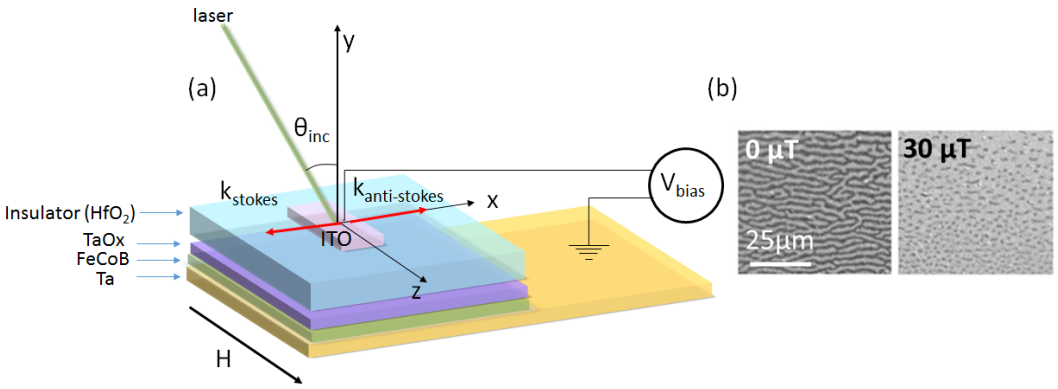

Figure 8.1 – (a) Schematic of the sample and setup for BLS measurement. During the accumulation of the spectra (4h), constant voltage is applied on a $150 \times 800 \mu m^2$ transparent ITO electrode and a magnetic field H is applied to saturate magnetization along z. (b) p-MOKE microscopy images of (left) thermally activated demagnetized stripe domains that transform into (right) skyrmionic bubbles on the application of small out of plane magnetic field ($30 \mu T$).

8.B.2 Wavevector k_{SW} dependence of frequency difference Δf

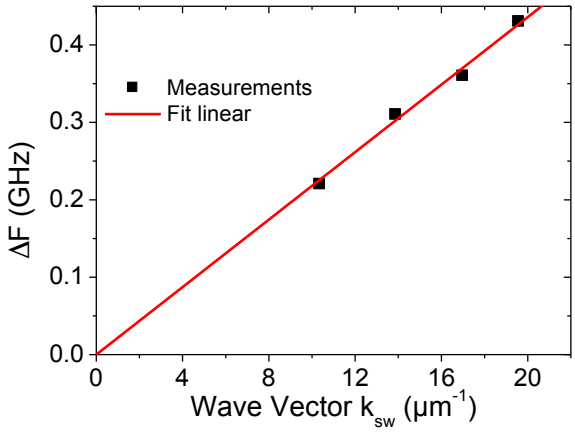

Figure 8.2 – Δf measured as a function of spin wave vector k_{SW}

The first part of the experiment is to determine the response of the difference in the Stokes and Anti-stokes frequency peaks as a function of the spin wave vector k_{SW}. We observed that the frequency difference varies linearly with the spin wave vector k_{SW} (see fig. 8.2), which is what is expected from the given expression [120, 121]

$$\Delta f = \frac{2\gamma}{\pi M_s} k_{SW} D \tag{8.2}$$

where γ is the gyromagnetic ratio, M_s the saturation magnetization and D Interfacial DMI energy. [114, 119–122]

Having observed a linear Δf Vs k_{SW} behavior, we could perform the BLS measurements at one fixed $k_{SW} = 20.45 \mu m^{-1}$ under different applied voltages. This in fact allows fewer mea-

surements and hence prevents electrode degradation due to long hours of voltage application.

8.B.3 BLS spectra under different applied voltages

We measured the BLS spectra at 0, -10V and +10V for an accumulation period ranging from 4 to 15 hours. The corresponding BLS spectra are represented in figure 8.3a. The frequency

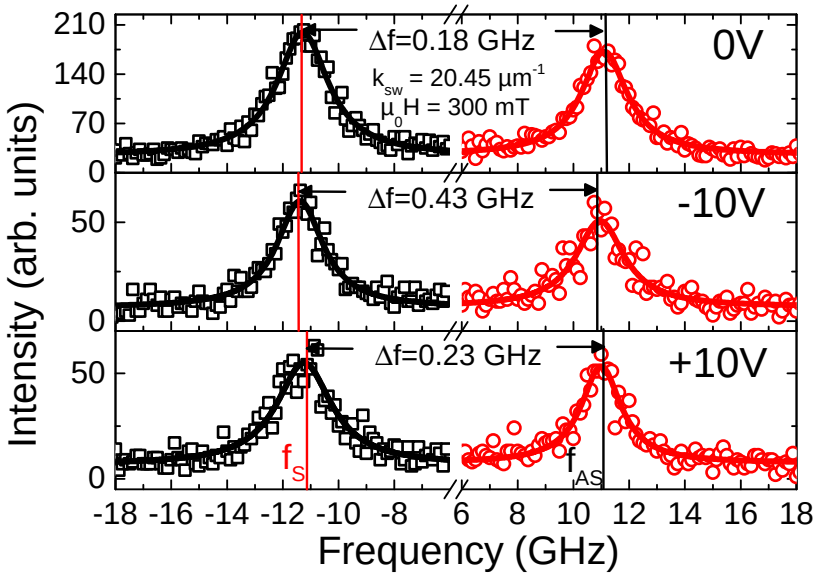

Figure 8.3 – BLS spectra (open symbols) measured while applying 0V,-10V and +10V and the corresponding Lorenztian fits (solid curve). f_S and f_{AS} correspond to frequencies of the Stokes and the Anti-Stokes peaks and are marked with vertical lines. The shift in frequency $\Delta f = | f_S | - | f_{AS} |$ is proportional to the interfacial DMI. It changes by 140% between 0 and -10V.

difference Δf between Stokes (f_S) and anti-Stokes (f_{AS}) peaks $\Delta f = | f_S | - | f_{AS} |$ is determined from the Lorentzian fits. For a gate voltage of -10V, we observe a significant change of the BLS spectrum, corresponding to 140% increase of Δf. By contrast, a very small change in Δf is observed for +10V. Similar non-linearity with voltage has been reported in studies of electric field effect on interfacial anisotropy[106, 109]. Since data acquisition for BLS lasts several hours, the electric field effect measured here corresponds to long time scale phenomena which involves ion migration and hence can produce non-linear effects. We recover the 0V spectrum (see section8.B.3) after the -10V and +10V measurements indicating complete reversibility of the involved mechanisms.

Determination of DMI as a function of applied voltage

Interfacial DMI energy D is determined from Δf using expression 8.2. Here $\gamma/2\pi = 28.5$ GHz/T was determined by Ferromagnetic Resonance (FMR) on 5 nm FeCoB films by M.Belmeguenai at LSPM in UniversitÃ Paris 13. M_s averaged over $3mm^2$ at 0V ($1.05 \times 10^6 A/m$) is measured by Superconducting Quantum Interference Device (SQUID) magnetometry and its variation with voltage is measured from the Kerr signal amplitude of hysteresis loops observed by p-MOKE (inset of Fig. 8.4b). Less than 6% variation of M_s is observed in this voltage range. Taking

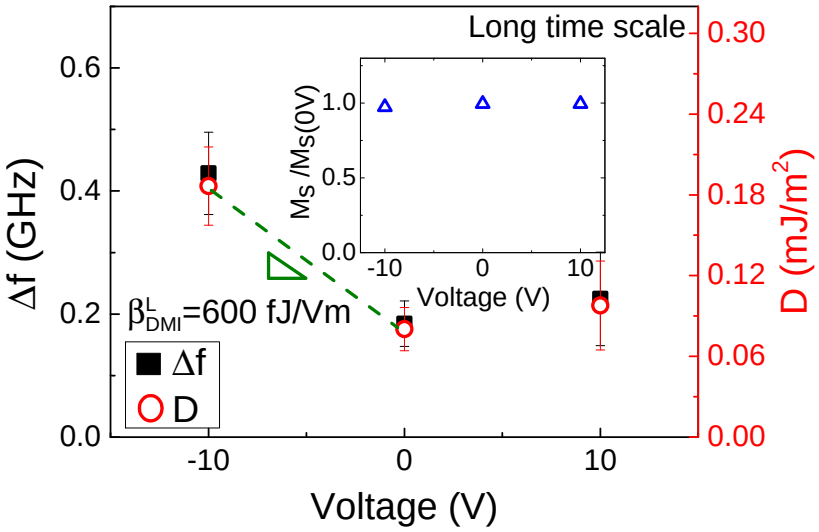

Figure 8.4 – Variation of Δf and deduced D as a function of applied voltage. The error bars in Δf are calculated from the fits of spectra. To extract D, the M_s variation with applied voltage has been taken into account (see inset showing 6% variation of M_s measured by p-MOKE).

this variation into account, the evolution of D with voltage is extracted, as represented in Fig. 8.4: it varies from 0.08 ± 0.01 at 0V to 0.18 ± 0.03 mJ/m^2 at -10V, giving a variation of $\Delta D = 0.1 \pm 0.04$ mJ/m^2. We thus achieve 130% variation of DMI in response to an electric field of $E = -170$ MV/m. Taking into account our error bars on DMI calculation, the estimated DMI increase is between 70 and 200%. It corresponds to a variation of the surface DMI coefficient by $\Delta D_s = \Delta(D.t) = 65 \pm 25$ fJ/m, where t is FeCoB thickness taking into account the magnetically dead layer, the efective ferromagnetic thickness t = 0.65 nm, (see chapter 6 for the detailed explanation of dead layers). This variation of D (resp. D_s) is three (resp. two) orders of magnitude higher than the only previous experimental observation of voltage induced DMI in thick films[117] ($\Delta D = 40$ nJ/m^2 or $\Delta D_s = 0.8$ fJ/m).

Reversibility of BLS measurements

First to check the time constants of the different electric field mechanisms involved, we studied the evolution of the equilibrium stripe domain width L_{eq} through p-MOKE on the scale of minutes to hours shown in figure 8.5. As the change in the stripe domain width is directly dependent on the domain wall energy σ_W and hence DMI, their evolution in time is directly related to the evolution of σ_W and hence DMI explained in subsection 8.C.1. We see in figure 8.5 that saturation is reached over 1 hour time scale. This ensures that the BLS measurements, correspond to the stable equilibrium of the system as data acquisition time is 4 hours. Further we also observe from the BLS measurements that the DMI value at 0V is recovered after -10V or +10V measurements under bias applied for 4 hours illustrated in figure 8.6. This indicates that the electric field effect mechanism involved is under reversible regime. However on exposing the electrode to 20V for 12 hours, we see that the DMI value at 0V could not be recovered, suggesting an irreversible mechanism or a possible electrode damage.

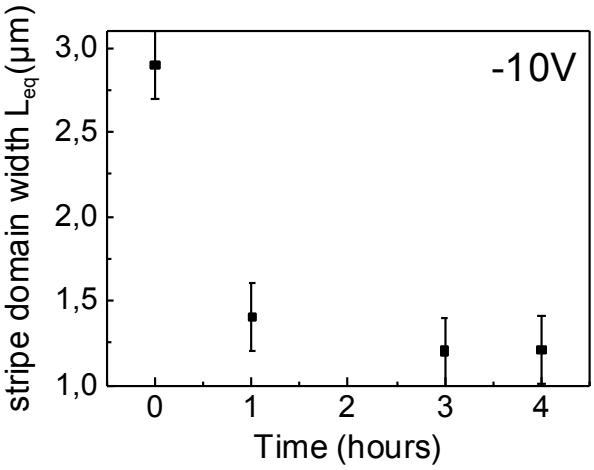

Figure 8.5 – Evolution of equilibrium stripe domain width L_{eq} with applied voltage duration, as measured by p-MOKE microscopy.

Discussion

From BLS measurements we obtain a large electric field efficiency coefficient for the DMI β_{DMI}^{long}=600fJ/Vm between 0V and -10V. The observed voltage induced variation of DMI in Ta/FeCoB/TaOx samples is even larger than its relative value at 0V. This relatively small DMI value of 0.08 mJ/m^2 at 0V is consistent with other studies in similar systems based on Ta/FeCoB, where the top oxide is MgO [113, 129, 130], indicating a small Fert-Levy DMI contribution of Ta/FeCoB interface. It is for instance much smaller than the value about $1-2mJ/m^3$ obtained in Pt/Co/AlOx samples [121, 131]. By contrast, Rashba-DMI at FeCoB/TaOx interface is likely to exist [27] and to contribute to the total DMI. Our values are similar to the results of Yu et al. [66, 132], where the structures are similar with top layer of Ta(0.8-0.9Å)/MgO or TaOx. Moreover, given the short screening length of electric field in a metal, the gate voltage only affects this top FeCoB/TaOx interface. Thus the strong sensitivity of DMI to gate voltage we have observed suggests that the major contribution to DMI comes from this interface. This result could thus validate the existence of Rashba-DMI at FM/oxide interfaces and its large sensitivity to electric field as explained figure 8.7.

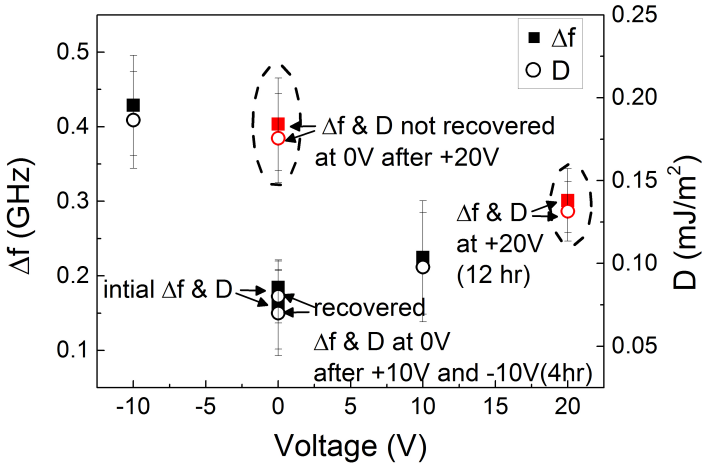

Figure 8.6 – (a) Variation of frequency difference Δf measured by BLS and deduced interfacial DMI as a function of applied voltage. The recovery of Δf and hence the interfacial DMI energy D at 0V after the measurements at -10V and 10V, (the sequence of measurements being (i) 0V, (ii) -10V, (iii) +10V, (iv) 0V) indicates the reversibility of the voltage effect. However on the application of higher voltages (+20V) for very long durations (12 hours), the electric field effect becomes irreversible indicating irreversible ion migration or a possible electrode damage.

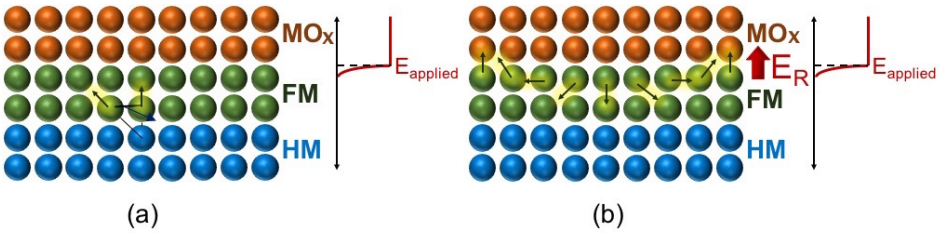

Figure 8.7 – Schematics of the interface between heavy Metal (HM), ferromagnet (FM) and metal oxide (MOx) representing the effect of applied electric field. (a) Fert-Levy DMI contribution remains unaltered by the applied electric field due to the screening effect. (b) The applied electric field directly acts on the FM/MOx interface leading to the modulation of Rashba-DMI contribution.

8.C Electric Field Effect on magnetic domains: Magneto-Optic Kerr Effect measurements (MOKE)

To further explore the influence of electric field on magnetic parameters like anisotropy and exchange, we systematically studied magnetic domain configuration using p-MOKE microscopy on the same sample at different applied voltages. As mentioned in the theory chapter 4, the electric field mechanism can vary depending on the materials involved and the duration of voltage application. Therefore it is important to distinguish between the long and the short term voltage application effects on the magnetic properties.

8.C.1 Long Time Scale effects

First, to be able to compare with the BLS measurements we performed p-MOKE measurements over long time scales (4 hours). Like in the case of BLS, we recovered the initial magnetic parameters at 0V after the measurements under voltage, once again confirming the reversibility of the effects. However irreversible changes in the magnetic properties were also observed for higher voltages applied for a long time.

Measurement of L_{eq} *and extraction of* σ_W

P-MOKE images were recorded at different applied voltages at the end of each 4 hour duration. We see in Fig. 8.8(a) that at zero magnetic field and zero applied voltage, stripe domains are identical both below and outside the electrode. The spontaneous thermal demagnetization results in high nucleation density and domain wall mobility. The stripe domains are hence close to their lowest energy state. By measuring their equilibrium width L_{eq} at different voltages, the corresponding domain wall energy σ_W can be extracted using[69]:

$$\sigma_W = \frac{\mu_0 M_s^2 t}{\pi} \ln\left(\frac{L_{eq}}{\alpha t}\right) \tag{8.3}$$

with t the ferromagnetic film thickness, and α a constant taken equal to 0.955. As the domain sizes in our case is larger than the domain wall width and the ferromagnetic film thickness is smaller than the characteristic dipolar length[133], this model could be safely applied in our case. The extraction of L_{eq} from the p-MOKE images was carried out using fast Fourier transform on MATLAB software (see Annex). At negative voltages, L_{eq} undergoes a strong reduction in size and the stripes become closely spaced as seen in Fig. 8.8a (right) (from 2.9 μm at 0V to 1.1 μm at -10V). Taking into account the small variation of M_s in this voltage range, we deduce σ_W. It is found to decrease strongly for negative voltage whereas a weak decrease is observed for positive voltage as shown in figure 8.8b.

The p-MOKE measurements over long time scales (4h) which were done to mimic BLS measurements thus corresponds to the saturation region. Later on, we observe on measuring again at 0V after the measurements at $\pm$10V that the values of L_{eq} and hence the σ_W are recovered shown in figure 8.9 which proves again the reversibility of the electric field effect.as

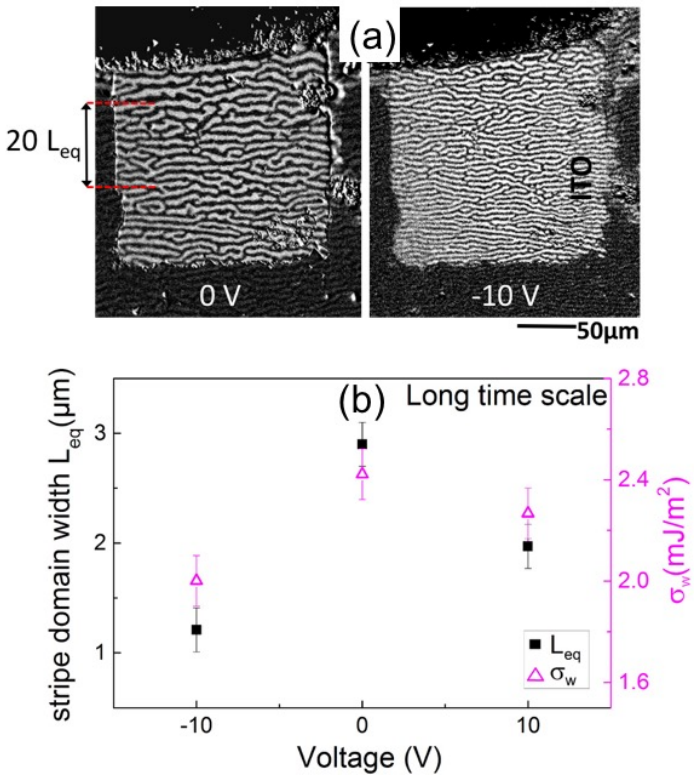

Figure 8.8 – (a) P-MOKE images at short time scales in the region of $150 \times 300\mu m$ ITO electrode in the absence of magnetic field at 0V (left) and -20V(right) applied voltage. The equilibrium stripe domain width L_{eq} reduces drastically in size on applying -10V. (b) Measured variation of stripe domain width L_{eq} (squares) and deduced domain wall energy σ_W (triangles) as a function of applied voltage for long time scales (4-15h)

Extraction of A and estimation of A × K variation

The domain wall energy in the presence of an interfacial DMI is given by[64, 126]

$$\sigma_W = 4\sqrt{AK_{eff}} - \pi \mid D \mid \tag{8.4}$$

with K_{eff} the effective anisotropy ($K_{eff} = K_s/t - 0.5\mu_0 M_s^2$ where K_s is the surface anisotropy) and A the exchange stiffness. By combining BLS and p-MOKE results on DMI and σ_W respectively, we deduce that $\sqrt{AK_{eff}}$ at these long time scales varies by less than 10% in this voltage range. From the values of M_s and H_k at 0V determined using SQUID, we extract the value of $A = 12pJ/m$ using the expression8.4.

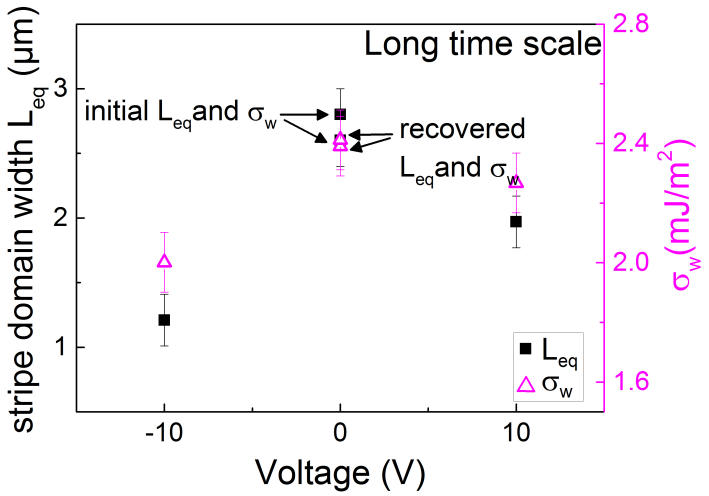

Figure 8.9 – Measured variation of equilibrium stripe domain width L_{eq} p-MOKE and deduced domain wall σ_W energy as a function of applied voltage. The recovery of the values at 0V after long time scale measurements at -10V and 10V (the sequence of measurements being (i) 0V, (ii) -10V, (iii) +10V, (iv) 0V) further confirms the reversibility of the voltage effect.

8.C.2 Short Time Scale effects

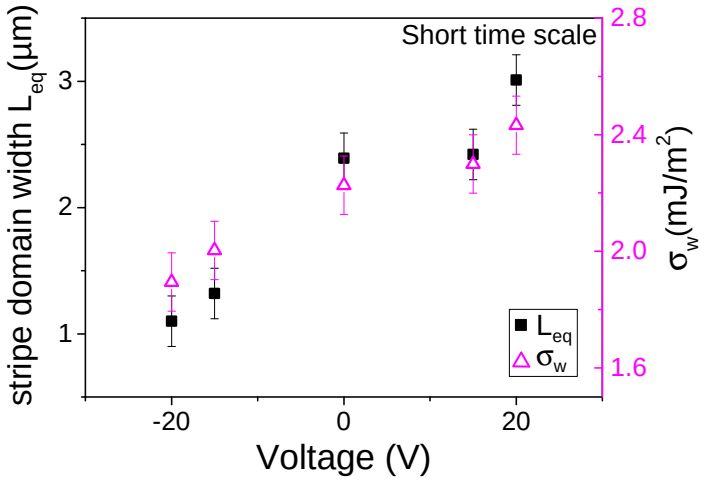

Figure 8.10 – Measured variation of stripe domain width L_{eq} (squares) and deduced domain wall energy σ_W (triangles) as a function of applied voltage for short time scales (few mins). As the measurements for the two time scales are performed on two different electrodes, the values at 0V differ slightly for the two measurements at long and short time scales.

We also verified the reversibility of the short time scale p-MOKE measurements of the stripe domain width under voltage. We observed that the values are recovered at 0V after measurements at ±20V as shown in figure 8.11.

From the point of view of applications, it is also crucial to study the dynamic change of interfacial DMI with voltage at shorter time scales. It would in turn also highlight the difference in the electric field effect mechanism at these time scales. We hence performed p-MOKE microscopy by applying voltages for a few minutes.

Measurement of L_{eq} *and extraction of* σ_W

Again by recording p-MOKE images at different voltages but this time for a duration of a minute each, L_{eq} was extracted by fast Fourier transform. At these durations, contrary to long time scale observations, L_{eq} and σ_W vary monotonically with voltage, as represented in figure 8.10. This brings out the difference in the electric field effect mechanisms for the two time scales. A monotonic trend was qualitatively observed for short time scales on all electrodes that we measured on this sample and also on an equivalent one from another wafer.

Evolution of M_s *and* H_K *with gate voltage*

In order to extract DMI variation under voltage at short time scales we measured the variations of H_k and M_s with p-MOKE in the range of ± 20V. They both decrease (increase) with negative (positive) voltages which is in agreement with other studies [107]. We measured M_s evolution by the amplitude of the Kerr signal change when the magnetization is reversed, as represented by the arrow in the inset of figure 8.12b. As only voltage changes, the Kerr signal is proportional to M_s (other optical parameters are constant during these measurements performed in the

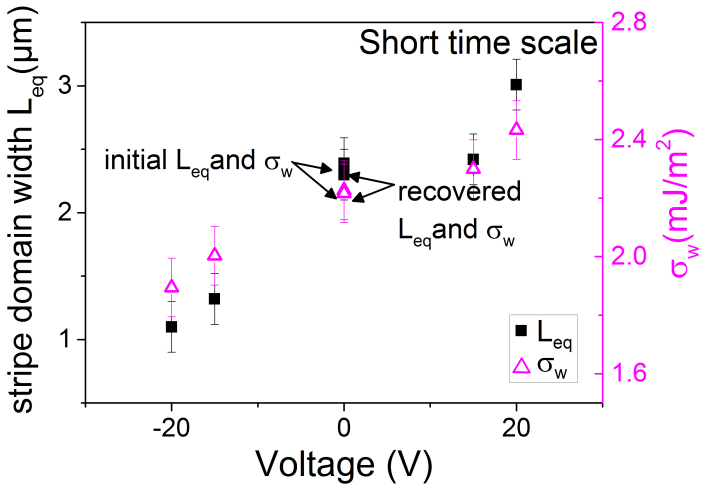

Figure 8.11 – Measured variation of equilibrium stripe domain width L_{eq} using p-MOKE and deduced domain wall energy σ_W as a function of applied voltage. The recovery of the values at 0V after long time scale measurements at -20V and 20V (the sequence of measurements being (i) 0V, (ii) -15V, (iii) -20V, (iv) 15V (v) 20V (vi) 0V) further confirms the reversibility of the voltage effect.

same condition). Its variation under voltage is presented in figure 8.12a. M_s variation in the range of $\pm 20V$ is found to be 6%.

The measurements of the anisotropy field H_k were not straightforward under applied electric and magnetic field. Hard axis measurement could not be performed using VSM or SQUID under applied electric field. We had to therefore use the same p-MOKE setup to measure it. To measure H_k, we applied an in-plane magnetic field and measured the Kerr signal as shown in figure 8.13a. With this setup there is always a small angle between the sample plane and the horizontal such that the applied in-plane magnetic field is not perfectly along the sample plane. Hence, the obtained hard-axis curves are fitted using Stoner Wohlfarth model (described in the thesis of Marine Schott) to extract the anisotropy field as a function of applied voltage (see fig 8.13b). These measurements were made only on short time scales owing to the limitations of experimental setup. 6% variation of H_k is observed in the range of $\pm 10V$ which on extrapolation to $\pm 20V$ gives a variation of 11% for short time scales.

Extraction of DMI

The DMI variation with voltage at short time scale is then extracted taking into account the variations of M_s and H_k with voltage. Since we show that the variation of M_s is small, we consider exchange stiffness A to be constant in this voltage range. DMI change as function of voltage is plotted in figure 8.14. It can be seen from the plot that the DMI varies linearly with voltage at short time scales hinting at a sign reversal on extrapolation to higher voltages.

In table 8.1, we have reported all experimental parameters used in the main text. They are given, when relevant, for the different applied voltages and at the two time scales, together with the measurement or extraction method.

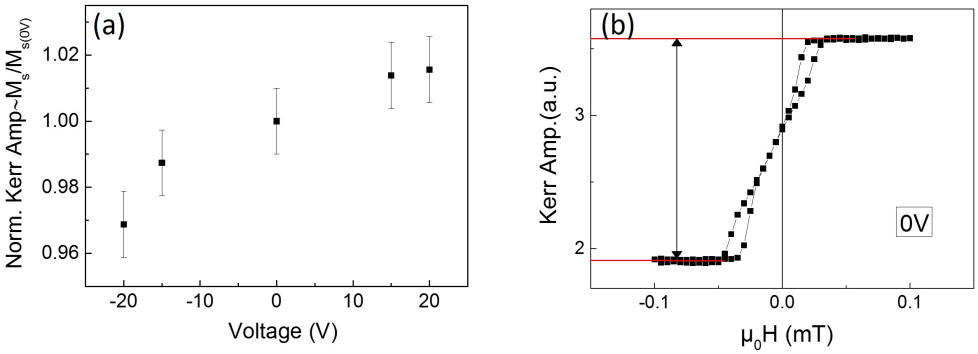

Figure 8.12 – (a) Variation under gate voltage of the amplitude of Kerr signal step at short time scales (as represented by the arrow in inset) normalized by its value at 0V. It is proportional to saturation magnetization M_s. (b) Corresponding loop measured at 0V with out-of-plane field.

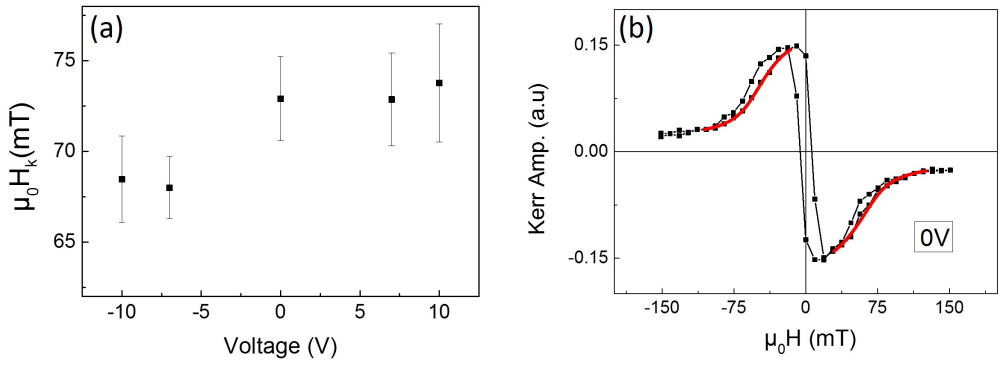

Figure 8.13 – (a) Variation under gate voltage of anisotropy field H_k at short time scales. (b) Kerr signal loop for 0V with in-plane applied magnetic field.

Discussion

The electric field efficiency at negatives voltages is four times larger for long ($\beta^L_{DMI} = 600 fJ/Vm$) as compared to short ($\beta^S_{DMI} = 157 fJ/Vm$) time scales. Both are however much larger than theoretical prediction[43] ($\beta_{DMI} = 26 fJ/Vm$) and the previous experimental demonstration in thick film[117] ($\beta_{DMI} = 3 fJ/Vm$). The qualitative difference between short and long time scale results could be ascribed to the different physical mechanisms involved. We have also evaluated β_{K_s} and we obtain values around 80 (short-time scale) and $200 fJ/Vm$ (long time scale), which are a bit smaller but of the same order of magnitude as β_{DMI}. This is expected as both Rashba-DMI and surface anisotropy find their origin in spin-orbit coupling. In fact the 11% variation of anisotropy field corresponds to a similar variation of K_s in absolute values as compared to the variation of DMI; but these variations presented in relative values are very different since the absolute value of K_s is high whereas the absolute value of DMI is low.

This behavior could be explained as following. For short time measurements, negative

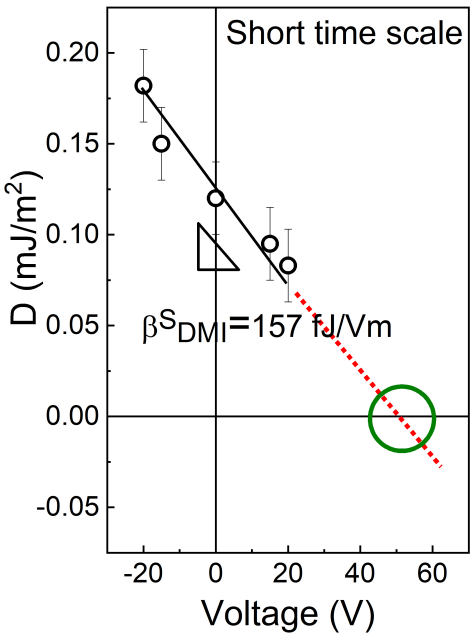

Figure 8.14 – Variation of interfacial DMI as a function of applied voltage for short time scales inferred for short time scales. A linear extrapolation (red dashed line) to higher positive voltages shows that D can be reduced to zero and could even reverse sign (marked by green circle).

electric field would add up to the Rashba field (thus increasing the DMI) as explained in figure 8.15, while a positive one would partially compensate it[134]. Therefore we propose that the large DMI sensitivity to gate voltage can be explained by the Rashba-DMI contribution originating from the FeCoB/TaOx interface. We further suggest that the stronger amplification of DMI at negative voltage for long time scale is related to the additional effect of oxygen migration towards the FeCoB/TaOx interface. Since the FM/I interface is slightly underoxidized, this ion migration results in a more optimally oxidized interface reinforcing the Rashba-field. However, for positive voltages, the DMI evolution at long time scale is more complex to analyze. The shift of the oxidation front away from the FM film, may strongly alter both the Rashba field and any charge effect via changes in crystalline and orbital structures. Similarly, the voltage induced variation of anisotropy due to ion migration was observed to be asymmetric in other systems and strongly dependent on the location of the oxygen front (described in the supplementary material of Bauer et al.[109]). As both the anisotropy and DMI stem from spin orbit coupling at this interface, this scenario could explain a similar behavior versus voltage for DMI in our system.

Parameters	Voltage	4h duration	Voltage	Few min duration	Method
Δf (GHz)	0V -10V 10V	0.18 ±0.04 0.43± 0.07 0.23± 0.07			BLS
$M_s(0V)$ (MA/m)	1.05				SQUID
$M_s(V)/M_s(0V)$	0V -10V +10V	1 0.94 ±0.01 0.94 ±0.01	0V -20V +20V	1 0.96 ±0.01 1.02 ±0.01	p-MOKE
$\mu_0 H_k(0V)$ (mT)	73.0				SQUID
$\mu_0 H_k(V)/\mu_0 H_k(0V)$			0V -10V +10V	1 0.95 ±0.05 1.06 ±0.05	p-MOKE
σ_W (mJ/m^2)	0V -10V +10V	2.37±0.3 1.84 ±0.3 2.21 ±0.3	0V -20V +20V	2.21±0.2 1.84 ±0.2 2.41 ±0.2	p-MOKE
D (mJ/m^2)	0V -10V +10V	0.08±0.016 0.18 ±0.035 0.13 ±0.035	0V -20V +20V	0.12±0.02 0.185 ±0.02 0.08 ±0.02	BLS, p-MOKE

Table 8.1 – Summary of experimental parameters, with their measurement method, voltage and time scale

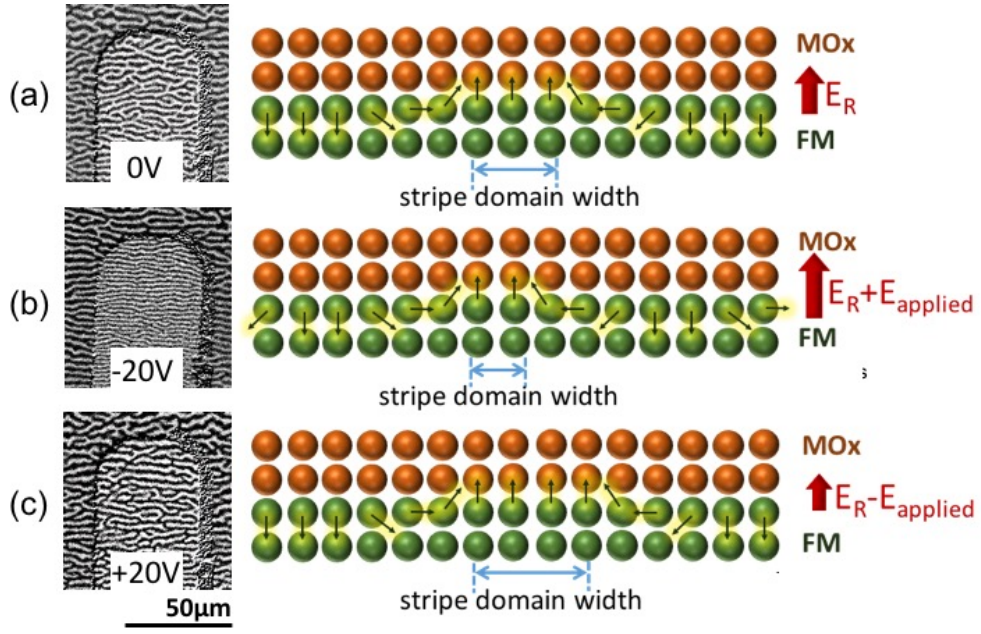

Figure 8.15 – P-MOKE images on the left and schematics of the interface between ferromagnet (FM) and metal oxide (MOx) representing the effect of applied electric field on the stripe domain width. (b) Rashba internal electric field E_R at the interface is enhanced on the application of voltage $E_{applied}$ along it leading to an increase of Rashba-DMI. It therefore leads to the reduction of the stripe domain width as the overall domain wall energy σ_W reduces.(c) The opposite voltage leads to an increase in the stripe domain width owing to the compensation of internal electric field at the interface and hence Rashba-DMI.

8.D Electric field effect as a function of the position on the wedge

We saw in chapter 6 and 7 that the magnetic properties like M_s and K_s vary as a function of the Ta and FeCoB wedge. Specially in the transition from out-of-plane magnetized zone to the paramagnetic zone, where we have the stripe like demagnetized domains, the properties change rapidly. We therefore studied the electric field effect as a function of the position on the sample, over 200µm, close to the electrode on which we had carried our previous studies by using p-MOKE. Here the Ta thickness varies by less than 0.02%. It leads to a similar variation of the magnetically dead layer and hence of the FeCoB thickness. We therefore measure the variation of M_s and H_k along this thickness range by using p-MOKE. Figure 8.17 shows the profile.

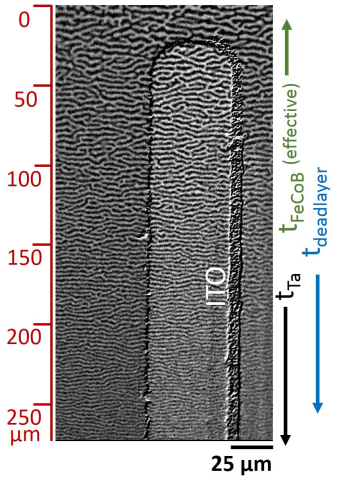

Figure 8.16 – P-MOKE image of an electrode indication the direction of the wedge of top Ta. Towards the increasing Ta thickness, underoxidized Ta results in magnetic dead layers which leads to the decreases of the effective thickness of FeCoB.

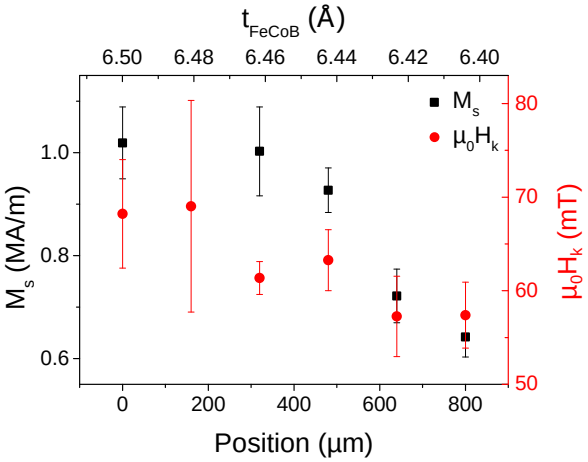

Figure 8.17 – Variation of saturation magnetization M_s and anisotropy field H_k as a function of position on the wedge indicated in figure 8.16 and the corresponding effective FeCoB thickness.

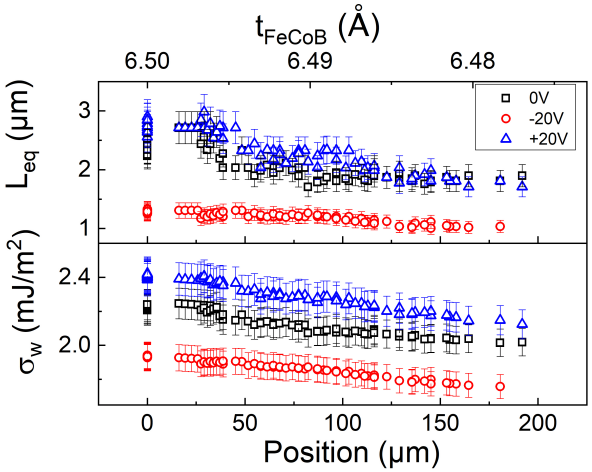

Figure 8.18 – Measured variation of stripe domain width L_{eq} and deduced domain wall energy σ_W as a function of position on the wedge and the corresponding effective FeCoB thickness for different applied voltage for short time scales (few mins).

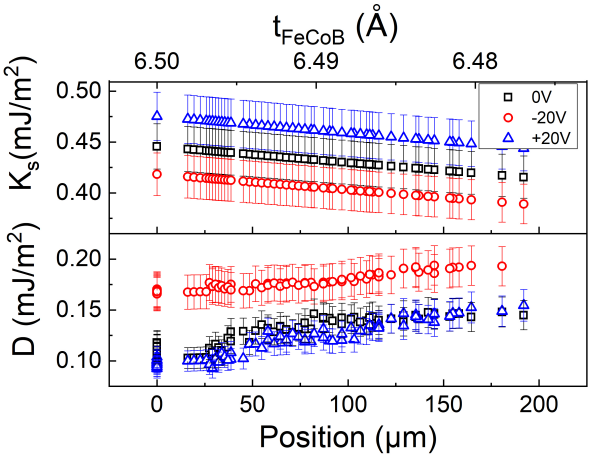

Figure 8.19 – Extracted variation of surface anisotropy K_s and deduced DMI coefficient D as a function of position on the wedge and the corresponding effective FeCoB thickness for different applied voltage for short time scales (few mins).

For M_s as a function of the wedge, the values obtained from p-MOKE in terms of Kerr amplitude were normalized by the values of M_s obtained from SQUID/VSM. We then measured L_{eq} along the wedge at 0V, -20V and +20V using p-MOKE microscopy. Using the values of M_s and H_k obtained above as a function of thickness and their corresponding variations with voltage for short time scales, we calculate the variation of σ_W along this wedge as a function of applied voltage. We see in the figure 8.18 that the $\sigma_W(V)$ variation along the wedge is larger for thicker FeCoB. We extract the variation of the surface anisotropy K_s and DMI coefficient D for the same as shown in figure 8.19. We infer that while $\delta K_s(V)$ stays constant along the wedge, $\delta D(V)$ can be seen to be larger for thicker FeCoB. The electric field efficiency for surface anisotropy β_{K_s} and DMI β_{DMI} are also calculated and plot as a function of the wedge in figure 8.20. We see that the efficiencies are slightly higher for thicker FeCoB, however considering the error bars we can say that it does not vary much within this thickness range .

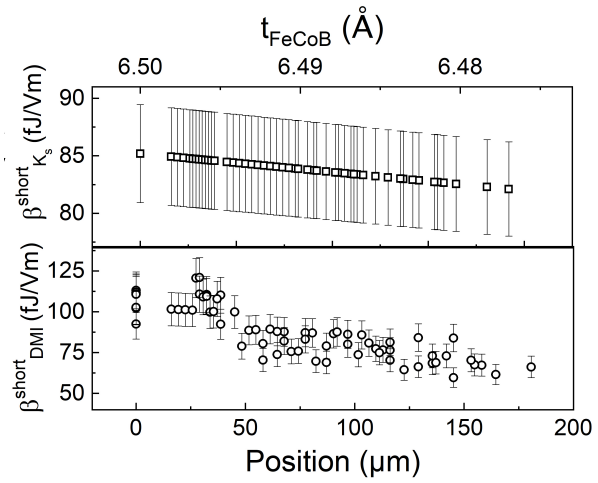

Figure 8.20 – Extracted variation of electric field efficiency for surface anisotropy β_{K_s} and DMI β_{DMI} as a function of position on the wedge and the corresponding effective FeCoB thickness for different applied voltage for short time scales (few mins).

Discussion

We observe from the above graphs that the surface anisotropy decreases as we move towards paramagnetic zone (higher Ta thickness: more magnetically dead layer: lesser effective FeCoB layer thickness). This is expected as interface starts getting less uniform. On the contrary the DMI coefficient D increases which can be attributed to the decrease of M_s.

8.E Electric Field effect on Skyrmions

To study the effect of voltage tuning of DMI on skyrmionic bubble size and density for short time scales, we use p-MOKE (figure 8.21): for negative voltages (-20V) the skyrmionic bubbles under the electrode show a higher density and a 50% smaller size as compared to 0V. These observations follow the evolution of the stripe domain width at short time scale (figure 8.10). Such a behavior was previously shown in Pt/Co/AlOx system[69]. However, in the latter case, a strong variation of anisotropy and saturation magnetization with electric field was fundamentally responsible for the change in size of skyrmionic bubbles. By contrast, in the present case of Ta/FeCoB/TaOx, the primary cause of this effect is a huge voltage induced DMI variation whereas M_s and H_k vary in smaller proportion.

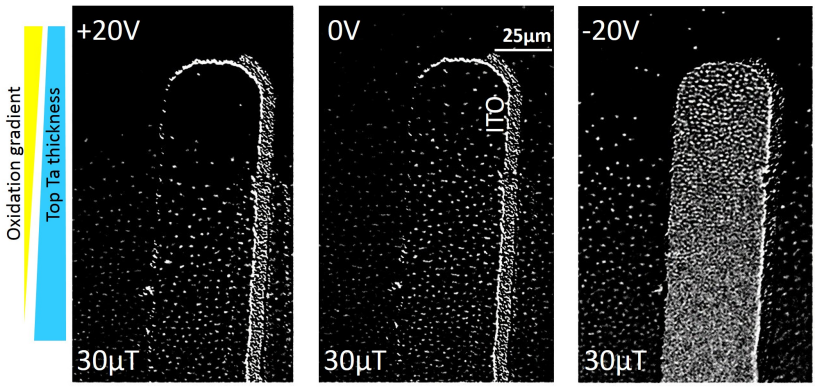

Figure 8.21 – P-MOKE images showing the evolution of skyrmionic bubble size and density at different applied voltages. The skyrmionic bubbles undergo a strong reduction in size and increase in their density at -20V. On the contrary at +20V, we observe an increase in their size and decrease in their density.

8.E.1 Chirality Switch?

In order to further explore the effect of DMI tuning in wider voltage range on skyrmionic bubbles, we extrapolate to higher positive voltages the monotonic variation of D obtained for short time scale: we expect a complete cancellation or even a sign reversal of D at around +40V. It corresponds to 670 MV/m and is below the typical breakdown voltage of oxides in spintronic devices (typically 600-900 MV/m for HfO_2 [135] or 1000-1500 MV/m for MgO[136]). Theoretical studies shows that DMI sign reversal is possible by playing on the oxygen coverage of the interface[116]. Additionally, an approach through Ar^+ irradiation has also been employed to locally control the sign of DMI[115]. Here we put forward the possibility of controlling the DMI sign both locally and dynamically through voltage gating.

To investigate the effect of this DMI sign reversal on skyrmions, we performed both analytical calculations and micromagnetic simulations. The analytical model used, was developed in ref[69]. It is used to explore the stable energy minima for an isolated bubble with the experimentally obtained magnetic parameters at different voltages. Micromagnetic simulations using the same parameters further reveal the internal structure of these isolated bubbles at the corresponding voltages. Using the experimental parameters, the evolution with voltage for the saturation

magnetization M_s, the uniaxial anisotropy constant $K_u = K_s/t$ and DMI energy D have been fitted in the -20/+20V range:

$$M_s(V) = \eta_{M_s} V + M_s(0V); \eta_{M_s} = 1.575 \times 10^3 A/V/m, M_s(0V) = 1.02 \times 10^6 A/m \quad (8.5)$$

$$K_u(V) = \eta_K V + K_u(0V); \eta_K = 2.1 \times 10^3 J.m^{-3}V^{-1}, K_u(0V) = 6.58 \times 10^5 J.m^{-3} \quad (8.6)$$

$$D(V) = \eta_D V + D_0; \eta_D = -0.0031 mJ.m^{-2}V^{-1}, D_0 = 0.11 mJ.m^{-2} \quad (8.7)$$

Analytical model

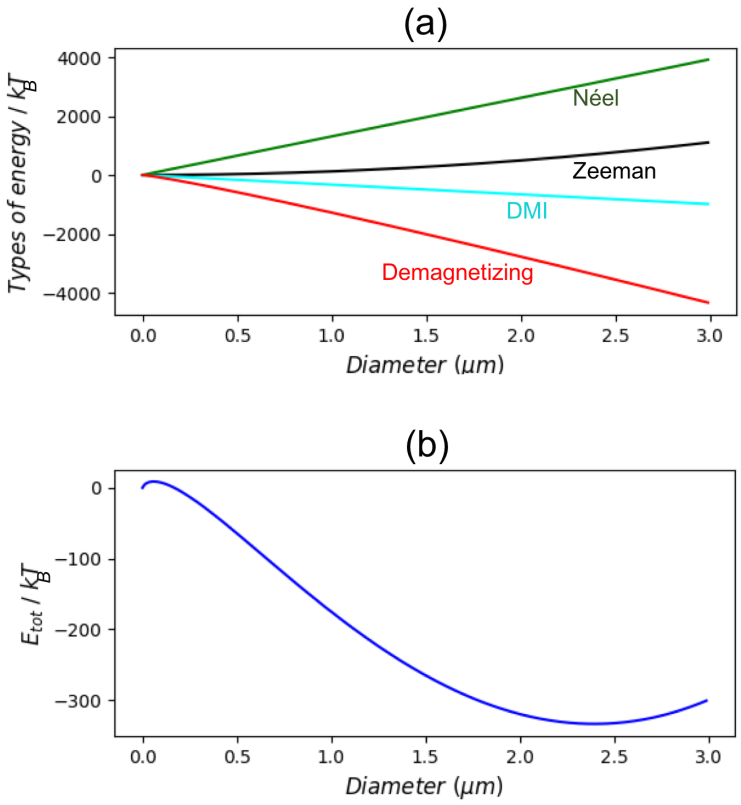

Figure 8.22 – Analytical model:(a) Variation of the different energy contributions as a function of the bubble diameter taking into account Dipolar, Anisotropy, Exchange, Zeeman and DMI energies. (b) Total energy difference between the bubble state and the saturated state as a function of the bubble diameter.

We use the analytical model of isolated bubble developed in ref Schott et al.[69] to calculate its energy relative to the saturated state as described in the chapter 7. This model incorporates the contributions from: dipolar, exchange, anisotropy, Zeeman and DMI energies as a function of the bubble diameter shown in figure 8.22(a) and calculates the total energy of an individual bubble relative to the saturated state represented in figure 8.22(b) . This energy can be written as:

$$\Delta E_{sb}(R, t, M_s, \sigma_W) = \sigma_W t 2\pi R + 2\mu_0 M_s H t \pi R^2 - \mu_0 M_s^2 \pi t^3 I(d) \quad (8.8)$$

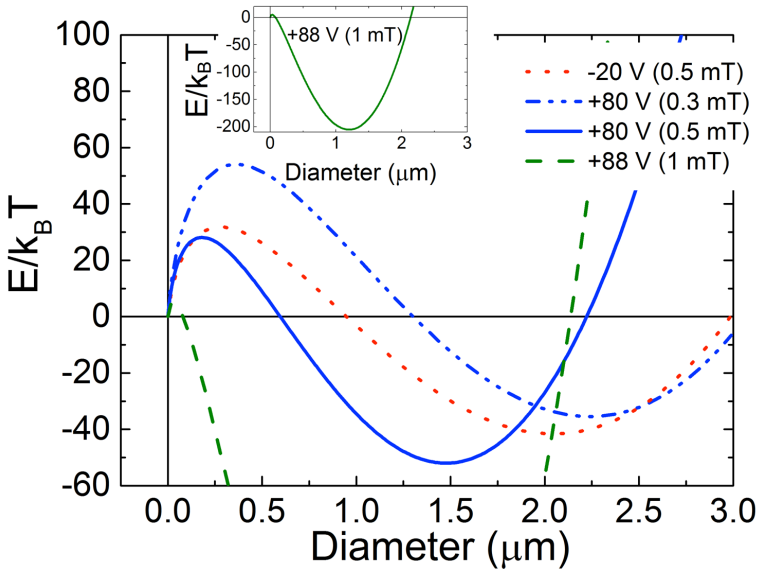

Figure 8.23 – Analytical model: variation of the energy difference between the bubble state and the saturated state as a function of the bubble diameter. The magnetic parameters are close to the ones measured previously for the -20V (short time) and extrapolated from the voltage variation of these parameters for the +80V and +88V. This latter voltages correspond to negative DMI. In all cases, a stable bubble is obtained. For the +88V we had to apply a larger magnetic field to stabilize a bubble with similar size. In inset is represented the full curve for +88V.

where σ_W is the domain wall energy, t is the layer thickness, R is the bubble radius, M_s is the saturation magnetization, $\mu_0 H$ is the applied magnetic field, and I(d) is the stray field energy gain where d = 2R/t (details in ref Schott et al.). Here the DMI is included inside the domain wall energy. Any inhomogeneities in domain wall structure or any non circular shape domain is thus not taken into account. Here the objective is to investigate whether a stable energy minima for the bubble state exists for the set of experimentally obtained parameters at different voltages for short time scale. Specially to check what we obtain at higher voltages where we expect a sign reversal of DMI and hence a change of chirality.

We therefore calculate bubble energy at -20V using the experimentally obtained values of the above mentioned parameters and at -80V by their linear extrapolation. This is compared with the thermal energy ($k_B T$) to estimate their thermal activation barrier. In the -20V case, D is equal to 0.18 mJ/m^2. For the +80V case, the extrapolation of DMI as a function of voltage for short time scale (fig 8.14) leads to a negative value of D (D= -0.13 mJ/m^2). We show that for the two sets of parameters corresponding to -20V and +80V, ie. to D=+0.18 and -0.13 mJ/m^2 respectively, stable skyrmionic bubbles of micrometer size can be obtained. To go further, we also investigated the case at +88V where the DMI is larger and leads to a negative domain wall energy. This means that the system enters into a stable spin spiral state. Hence in this case the magnetic field required to stabilize a bubble is higher (1mT) as compared to the two previous cases (0.5mT). The corresponding plots are shown in figure 8.23.

Micromagnetic Simulations

The analytical model gives a picture of the stable energy minima as a function of the bubble radius for different applied voltages. Consequently, in order to access the internal domain wall structure and the exact domain shape, micromagnetic simulations were performed using Mumax3 [137] with similar magnetic parameters (figure 8.24b,c). The Mumax3 code [137] integrates numerically the Landau-Lifshitz-Gilbert equation.The Gilbert damping is set to α=1 to decrease the relaxation time and temperature is 0K for simplicity. The geometry considered is a 6-µm-diameter disk with 5 nm x 5 nm cells. Initially, the disk is uniformly magnetized ($m_z > 0$) and a 2-µm-diameter bubble with opposite magnetization ($m_z < 0$) is generated in its center. The simulation relaxes the magnetic configuration to its lowest energy.

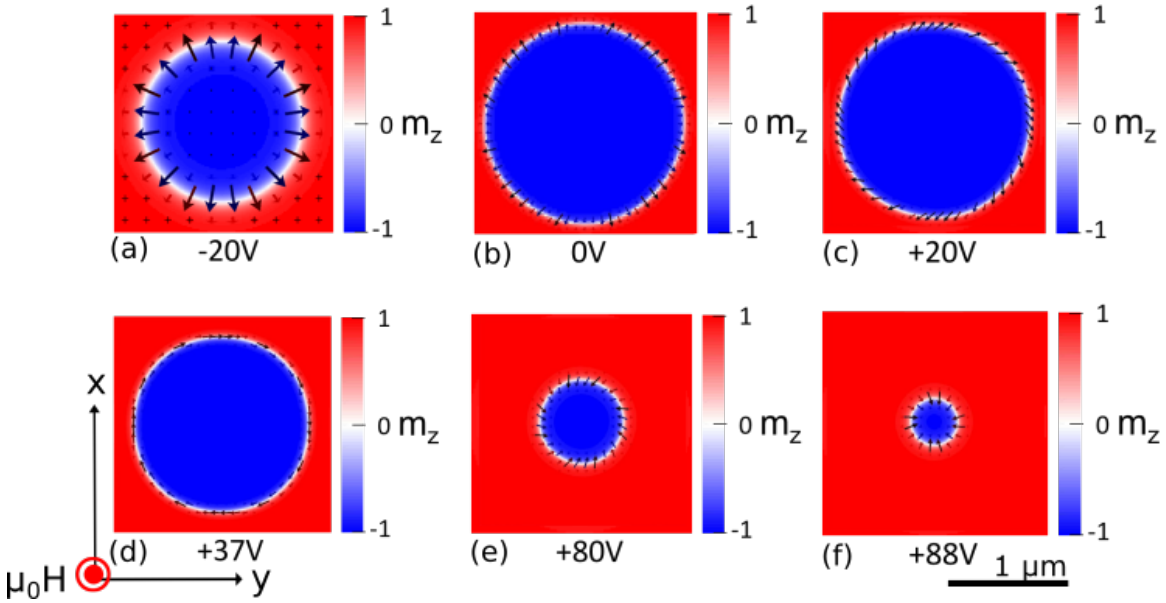

Figure 8.24 – Micromagnetic simulations (courtesy Roméo Juge) : magnetization configuration of skyrmionic bubbles obtained in a 6 µm dot at different voltages. The magnetic parameters for each voltage, are extracted from $M_s(V)$, $H_k(V)$, D(V) as functions of voltage experimentally obtained and extrapolated for higher voltages. In the case of -20V (a), the spins point outwards (left-handed chirality) while in the +80V(e) case, with opposite DMI sign, an opposite chirality (right-handed chirality) is stabilized. In this latter case however, the domain walls are not completely Néel type. For +88V(f) a perfect right handed Néel type skyrmion is obtained. We also show that at intermediate voltage: +37V (d), where the magnetization configuration of the skyrmion becomes Bloch-like with no preferred chirality as DMI is close to zero at this voltage. The magnetic parameters

For the -20V state, a circular skyrmionic bubble of 1.1 µm diameter with outward spins within the domain wall is stabilized (left-handed chiral Néel domain wall) as shown in figure 8.24(a). The obtained size is very close to experimental values. For the +80V state, a circular skyrmionic bubble state is also obtained but with opposite chirality, *i.e.* the spins point inward (right-handed) (figure 8.24(e)). The diameter in this latter case is slightly increased, consistent with the analytical calculations. The bubble diameter is 1.4 µm and the domain wall is not exactly Néel type: in fact the magnetization at the center of the domain wall presents a constant angle of 26° with respect to the radial direction. Hence, it is rather a Dzyaloshinskii domain

wall[29]. This is probably due to the fact that the DMI amplitude is close to the critical DMI necessary to obtain pure Néel walls. We obtain similarly a left-handed Dzyaloshinskii domain wall for the parameters at +20V (figure 8.24(c)) as the DMI is below the critical D. Therefore we did further simulations at +88V corresponding to $D = -0.16 mJ/m^2$. It gives a negative domain wall energy and thus leads to spin spiral state. We see that in this case a right-handed chiral bubble is stable with an applied magnetic field, shown in figure 8.24(f). Here the obtained domain wall is purely Néel, which is consistent with the increased absolute value of DMI. Simulation was also done using the magnetic parameters at +37V (figure 8.24(d)), where we expect the DMI to be almost zero. It results in a magnetic bubble surrounded by Bloch wall with no preferred chirality instead of Néel wall.

We note here that the value of the magnetic field used is higher in our analytical calculation and micromagnetic simulation (0.3 to 1mT as compared to 30μT for experiments) than the experiments. This difference could be ascribed to the fact that in the model and the simulation the presence of other bubbles and their mutual interaction which is what happens in the experimental case, is not taken into account. As the analytical model is based on a single isolated bubble case. The analytical calculation with 30μT leads to a very large single bubble (20μm diameter). Such an increase of diameter is not likely to occur in reality, but rather a distortion of the bubble or its division into many bubbles is more plausible. A lower energy state is thus possible with several bubbles with smaller diameter. The micromagnetic simulations are done on a 6 μm dot in order to have reasonable calculation time. In this case, due to the edge effect, the presence of other bubbles will be less likely than in an infinite thin film. In the presence of other bubbles in the film, their mutual repulsion/stray field interaction would result in a reduced size for a given magnetic field. Therefore we had to use increased magnetic fields to compensate for these interactions.

Below is the list of the parameters used for analytical calculations and micromagnetic simulations.

voltage (V)	M_s (MA/m)	K_s (mJ/m^2)	D_s (pJ/m)	A (pJ/m)	t (nm)	$\mu_0 H$ (mT)
Analytical model						
-20	0.987	0.436	+120.25	12	0.675	0.3
+80	1.1447	0.575	-91.2	12	0.675	0.3
+80	1.1447	0.575	-91.2	12	0.675	0.5
+88	1.159	0.592	-110	12	0.675	1
Micromagnetic simulations						
-20	0.987	0.418	+120.5	12	0.68	0.3
+80	1.1445	0.561	-91	12	0.68	0.3
+80	1.1445	0.561	-91	12	0.68	0.5
+88	1.157	0.572	-108	12	0.68	1

Table 8.2 – Parameters used for analytical model and for micromagnetic simulations

These simulations, combined with the analytical model results, show that a chirality switch controlled by gate voltage can be designed in this type of system. However, experimentally it still remains under speculation, how a skyrmion would dynamically switch between two types of chirality when the voltage is continuously ramped from negative to positive. From

the simulations, it seems that a LH-skyrmion with perfect Néel-type domain walls at negative voltage would transform to a LH-skyrmion with Dzyaloshinkii-type domain walls on increasing the voltage towards positive. It would become a non-chiral magnetic bubble with Bloch-type domain walls at the voltage which corresponds to zero DMI and further on increasing to positive voltages, it would transform into a RH-skyrmion with Dzyaloshinkii-type domain walls and finally to RH-skyrmion with perfect Néel-type domain walls. The simulations however represent the case when the change in the applied voltage is instantaneous. This type of transition however will depend on the time interval of the voltage ramp. The dynamics could differ if the frequency of the voltage ramp is higher or lower.

For applications, a change in chirality due to the change in the DMI sign would mean that individual skyrmions could selectively be moved in different directions under applied current. This is due to the fact that the direction of skyrmion motion depends on the chirality of the skyrmion and the sign of the spin hall angle of the heavy metal (described in detail in chapter 3). Since the latter remains constant, the change of the former would reverse the direction of motion of the skyrmion under the same applied current. This can be channelized for building intricate logic devices. Further material engineering to adjust DMI, M_s and K_s variations under voltage and also Rashba-DMI contribution would be necessary to optimize this behavior for applications.

8.F Conclusion

To conclude, we have measured a 130% variation in the DMI coefficient under voltage using Brillouin light spectroscopy in a Ta/FeCoB/TaOx trilayer. A monotonic variation of DMI with voltage is further observed at shorter time scales by p-MOKE microscopy. The huge electric-field effect on DMI might be explained by considering the fact that the main contribution to DMI stems from the interface with the oxide layer (Rashba DMI) and is therefore directly sensitive to the gate voltage. We further anticipate using micromagnetic simulations, a sign reversal of DMI at higher voltages, enabling a chirality switch. This result may ultimately lead to a dynamic control of the skyrmion properties for electrically programmable skyrmion-based memory and logic devices.

9

Conclusion

Here is a brief reminder of the some of the important concepts and results of the thesis.

We see that thin film systems consisting of Heavy Metal (HM)/Ferromagnet (FM)/Metal Oxide (MOx) provide the platform for the existence of chiral magnetic textures called skyrmions or skyrmionic bubbles. The implementation of skyrmions in memory or logic devices requires engineering of all the interfaces in the above mentioned trilayer systems. Several magnetic interactions govern the formation, stability and motion of these skyrmions of which Dzyaloshinkii-Moriya Interaction (DMI) and Perpendicular Magnetic Anisotropy (PMA) are of utmost importance. DMI in particular determines the chirality of the skyrmion depending on its sign. Several methods have been employed to control skyrmions via tuning the magnetic anisotropy and saturation magnetization. Electric field effect is one of the dynamic and low power consuming methods to achieve modulation of interfacial magnetic properties. The application of voltage to tune DMI and magnetic anisotropy in order to control skyrmions has been the major motivation for this thesis.

This thesis has described in detail the challenges associated in optimizing the trilayer system for achieving a stable energy landscape for skyrmions. A double wedged system *i.e.* a gradient of FM layer thickness and a gradient of MOx layer thickness perpendicular to the former, is deposited by sputtering. Such a system provides different thickness combinations of both FM and MOx layers on a single wafer to find the optimum for skyrmion stability. A simple model has been developed to examine the evolution of the magnetic properties as a function of the two wedges. A qualitative explanation of the variation of dead layer profile and interface anisotropy has been stated. We have further compared several systems on the basis of the top metal oxide layer in terms of anisotropy and dead layer profile variations. This method provides a way to study in detail all the magnetic parameters and their mutual dependence for several systems.

We chose Ta/FeCoB/TaOx system to be observed in detail as a function of the FeCoB and the top Ta layer thicknesses. We evaluated the system with the help of the simple model. We observe (i) out-of-plane (OP) anisotropy, (ii) in-plane (IP) anisotropy and (iii) paramagnetic (PM) (zones not magnetic at room temperature) zones as a function of FeCoB and top Ta thicknesses and the interface oxidation state. The transitions between these respective zones is where the effective anisotropy is low leading to low domain wall energy. We observed the low domain wall energy (transition) zones by using Polar Magneto-Optic Kerr Effect (p-MOKE) microscope where we see thermally demagnetized domain configuration. They transform into skyrmionic bubbles on the application of a small out-of-plane magnetic field ($\sim 30\mu$T). Further we notice that there are two distinct regions where skyrmionic bubbles are formed (i) near the OP anisotropy to PM transition and (ii) near OP to IP anisotropy transition. The motion of the bubbles in the first zone is uniform along the current direction confirming their homochirality whereas those in the second zone display inhomogeneous behavior. Then the change in the

interfacial magnetic properties and hence in the properties of skyrmions in the OP anisotropy to PM transition zone (which are found homochiral) as a function of applied electric field has been explored. We measured a0 130% variation in the DMI coefficient under voltage using Brillouin Light Spectroscopy. A monotonic variation of DMI with voltage is further observed at shorter time scales by p-MOKE microscopy. The huge electric-field effect on DMI might be explained by considering the fact that the main contribution to DMI stems from the interface with the oxide layer (Rashba DMI) and is therefore directly sensitive to the gate voltage. We further anticipate using micromagnetic simulations, a sign reversal of DMI at higher voltages, enabling a chirality switch. This result may ultimately lead to a dynamic control of the skyrmion properties for electrically programmable skyrmion-based memory, logic or neuromorphic devices.

10

Perspectives and Offshoots

10.A Introduction

In this chapter I first present some of the direct perspectives of my work and then other studies in which I took part during my PhD.

For the offshoots, The first section describes the generation of skyrmion bubbles and skyrmion bubble lattices from a ferromagnetic state at room temperature in Ta/FeCoB/TaOx sample by a controlled by single ultrafast (35-fs) laser pulse. The skyrmion bubble density is seen to increase with the laser fluence, and later attains saturation, forming disordered hexagonal lattices which enhances their topological stability. This study is promising for skyrmion based synaptic devices.

In this work, I participated in preparing the samples for the laser experiment. I worked on optimizing the thicknesses of the FeCoB and TaOx layer for deposition on glass, to obtain the desired energy landscape for skyrmions.

The second section describes another study which was conducted on our sample consisting of Ta/FeCoB/TaOx. It is related to the study of the response of the skyrmions to thermal agitation hence their brownian motion.

This study was conducted in Japan. I took part in preparing and optimizing the sample before sending it for their thermal study.

10.B Perspectives

For the material study we have conducted using a simple model, it has to be pursued further to formulate quantitative results. We need to optimize the fitting of the dead layer by choosing a Gaussian function which makes the fit smoother. We also need to clearly distinguish between the extrapolated and apparent dead layers and the variation of M_s and k_s along them to present more realistic systems. The appropriate value of the M_s needs to be used for each HM/FM/MOx system which would enable us to extract the corresponding values of K_s and K_{eff}. Furthermore, we plan to add the DMI energy and the calculation of domain wall energy to the model. The

aim is to be able to visualize the areas of low domain wall energy on the reconstructed map of effective anisotropy which would hint at the possible skyrmionic zones (skyrmions can be nucleated in low domain wall energy zones).

With the DMI control with voltage, experimentally it still remains under speculation, how a skyrmion would dynamically switch between two types of chirality when the voltage is continuously ramped from negative to positive. We need to design experiments to be able to apply higher voltages in order to observe a sign change of DMI and hence a witch of skyrmion chirality. One of the ideas is to observe skyrmion motion with current under applied electric field. A reversal in the direction of skyrmion motion at a certain voltage would indicate the DMI sign change.

10.C Offshoots

10.C.1 Ultrafast laser induced generation of skyrmion bubble lattices

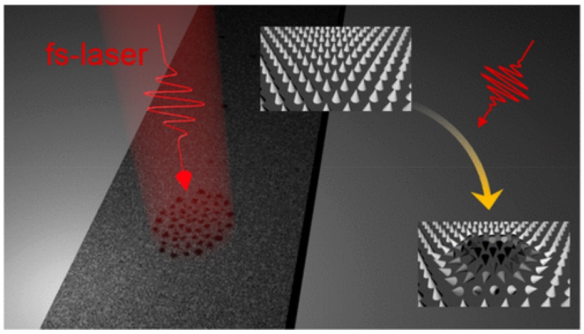

Figure 10.1 – Ultra fast laser induced generation of skyrmionic bubbles.

Here an ultrafast laser-induced generation of skyrmion bubbles and skyrmion bubble lattices is reported in Ta(30 Å)/ $Fe_{72}Co_8B_{20}$ (wedge, 7.5 Åto 10.3 Å)/TaOx (12 Å, naturally oxidized) trilayer film grown on a glass substrate. An ensemble of skyrmion bubbles is created from a ferromagnetic state by a 35-fs single laser pulse with low fluences. With the increasing laser fluence, the transition from an isolated skyrmion bubble state to a skyrmion bubble lattice state with controllable bubble density is observed. The laser heating-induced skyrmion bubble lattice formation is explained in the framework of the analytic bubble and bubble lattice models and micromagnetic simulations. Our results highlight the role of thermal effect in the creation of the skyrmion bubble lattice. It also offers an alternative way of ultrafast excitation and massive writing of clusters of skyrmions that decouples the writing operation from the skyrmion driving operation in the skyrmion-based shift register and that could be used in the emerging skyrmion-based synaptic devices. This result has been published : Je et al. [138]

10.C.2 Brownian motion of skyrmionic bubbles

We have witnessed already how all the different magnetic parameters like anisotropy, exchange and DMI participate in creating skyrmions at room temperature. Since the energy balance is delicate, any thermal perturbation can lead to their random motion *i.e.* Brownian motion.

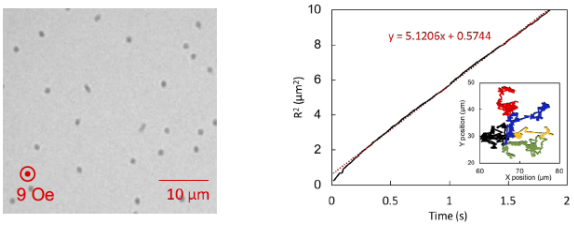

Figure 10.2 – (Left) Kerr image of skyrmionic bubbles under perpendicular magnetic field. (Right) Plot of mean square displacement of skyrmions as a function of time.

In this study, the diffusion coefficient of skyrmions was calculated. The film stack was Ta(3 nm)/$Fe_{72}Co_8B_{20}$(0.9-1.3 nm)/TaOx(0.5-0.9 nm)/Al(0.5 nm) deposited on SiO2 substrate by sputtering methods. Figure 1 (left) shows the picture of skyrmions (black dots) under perpendicular magnetic field taken by Kerr microscope. The observed skyrmion size, which depends on Fe72Co8B20 and TaOx oxidation state, is about 0.5 to 1.5 µ m. Figure 1 (right) is the mean-squared displacement (R2) of two dimensional skyrmions motion as a function of time. The inset shows trajectories of selected skyrmions at room temperature. The mean-squared displacement is fitted by a linear function (red dots line) to evaluate the diffusion coefficient. Diffusion coefficient of one dimensional motion of skyrmions on a wire was evaluated. Further difference between one and two dimensional Brownian motions is also highlighted. This would eventually help in designing Brownian computing.

List of Tables

List of Figures

Glosssary and List of Acronyms

A Micro-magnetic Exchange constant : in pJ/m.

D_s Micro-magnetic surface DMI constant : in pJ/m.

H_k Anisotropy field : in mT.

K_d Dipolar energy constant : in J/m^3.

K_s Surface anisotropy constant : in mJ/m^2.

K_u Magneto-crystalline uniaxial anisotropy constant : in mJ/m^2.

M_s Saturation Magnetization : in A/m.

T_c Curie temperature.

β_{DMI} Electric field efficiency coefficient for DMI $\frac{\Delta D}{V} t_{FM}$ in fJ/Vm.

β_{K_s} Electric field efficiency coefficient for surface anisotropy $\frac{\Delta D}{V} t_{FM}$ in fJ/Vm.

σ_W Domain wall energy : in mJ/m^2.

ACW Anti-Clockwise.

BLS Brillouin Light Spectroscopy.

CW Clockwise.

DMI Dzyaloshinskii-Moriya Interaction.

DW Domain wall.

FM Ferromagnet.

FMR Ferromagnetic Resonance.

GMR Giant Magneto-Resistance.

HDD Hard Disk Drive.

HM Heavy Metal.

IP In-Plane.

$\mathbf{K_{eff}}$ Effective anisotropy constant : in MJ/m^3.

$\mathbf{L_{eq}}$ Equilibrium stripe domain width.

MOKE Magneto-Optic Kerr Effect.

MOx Metal Oxide.

MRAM Magnetic Tunnel Junction.

MTJ Magnetic Random Access Memory.

OP Out-of-Plane.

PM Paramagnetic.

PMA Perpendicular magnetic anisotropy.

RAM Random Access Memory.

SHE Spin Hall Effect.

SOC Spin-Orbit Coupling.

SOT Spin-Orbit Torque.

SQUID Superconducting Quantum Interference Device.

$\mathbf{t_{DL}}$ thickness of dead layer(with no net magnetization) for a given ferromagnetic layer thickness.

$\mathbf{t_{FM}}$ Thickness of ferromagnet.

TMR Tunnel Magneto-Resistance.

VSM Vibrating Sample Magnetometer.

Bibliography

[1] M. N. Baibich, J. M. Broto, A. Fert, F. Nguyen Van Dau, F. Petroff, P. Etienne, G. Creuzet, A. Friederich, and J. Chazelas. Giant magnetoresistance of (001)fe/(001)cr magnetic superlattices. *Phys. Rev. Lett.*, 61:2472–2475, Nov 1988. doi: 10.1103/PhysRevLett.61.2472. URL https://link.aps.org/doi/10.1103/PhysRevLett.61.2472. 1

[2] G. Binasch, P. Grünberg, F. Saurenbach, and W. Zinn. Enhanced magnetoresistance in layered magnetic structures with antiferromagnetic interlayer exchange. *Phys. Rev. B*, 39:4828–4830, Mar 1989. doi: 10.1103/PhysRevB.39.4828. URL https://link.aps.org/doi/10.1103/PhysRevB.39.4828. 1

[3] Shinji Yuasa, Taro Nagahama, Akio Fukushima, Yoshishige Suzuki, and Koji Ando. Giant room-temperature magnetoresistance in single-crystal fe/mgo/fe magnetic tunnel junctions. *Nature materials*, 3:868–71, 01 2005. doi: 10.1038/nmat1257. 1

[4] Stuart Parkin, Christian Kaiser, Alex Panchula, Philip Rice, Brian Hughes, Mahesh Samant, and See-Hun Yang. Giant tunneling magnetoresistance at room temperature with mgo(100) tunnel barriers. *Nature materials*, 3:862–7, 01 2005. doi: 10.1038/nmat1256. 1

[5] M Julliere. Tunneling between ferromagnetic films. *Physics Letters A*, 54:225–226, 09 1975. doi: 10.1016/0375-9601(75)90174-7. 1

[6] J. S. Moodera, Lisa R. Kinder, Terrilyn M. Wong, and R. Meservey. Large magnetoresistance at room temperature in ferromagnetic thin film tunnel junctions. *Phys. Rev. Lett.*, 74:3273–3276, Apr 1995. doi: 10.1103/PhysRevLett.74.3273. URL https://link.aps.org/doi/10.1103/PhysRevLett.74.3273. 1

[7] Stuart S. P. Parkin, Masamitsu Hayashi, and Luc Thomas. Magnetic domain-wall racetrack memory. *Science*, 320(5873):190–194, 2008. doi: 10.1126/science.1145799. URL http://science.sciencemag.org/content/320/5873/190. 2, 32

[8] Albert Fert, Nicolas Reyren, and Vincent Cros. Magnetic skyrmions: advances in physics and potential applications. *Nature Reviews Materials*, 2(7):17031, 2017. doi: 10.1038/natrevmats.2017.31. URL https://www.nature.com/articles/natrevmats201731. 2

[9] Albert Fert, Vincent Cros, and João Sampaio. Skyrmions on the track. *Nature Nanotechnology*, 8(3):152–156, 2013. doi: 10.1038/nnano.2013.29. URL http://www.nature.com/articles/nnano.2013.29. 2, 32

[10] P. Bruno. Theory of interlayer exchange interactions in magnetic multilayers. *Journal of Physics: Condensed Matter*, 11(48):9403, 1999. doi: 10.1088/0953-8984/11/48/305. URL http://stacks.iop.org/0953-8984/11/i=48/a=305. 12

[11] J. Faure-Vincent, C. Tiusan, C. Bellouard, E. Popova, M. Hehn, F. Montaigne, and A. Schuhl. Interlayer magnetic coupling interactions of two ferromagnetic layers by spin polarized tunneling. *Physical Review Letters*, 89(10):107206, 2002-08-20. doi: 10.1103/PhysRevLett.89.107206. URL https://link.aps.org/doi/10.1103/PhysRevLett.89.107206. 12

[12] Stephen Blundell. *Magnetism in Condensed Matter*. OUP Oxford, 2001-10-04. ISBN 978-0-19-850591-4. Google-Books-ID: OGhGmgEACAAJ. 12

[13] J. M. D. Coey. Magnetism and magnetic materials by j. m. d. coey, 2010-03. URL /core/books/magnetism-and-magnetic-materials/AD3557E2D4538CAA8488A8C1057313BC.

[14] Alex Hubert and Rudolf Schäfer. *Magnetic Domains: The Analysis of Magnetic Microstructures*. Springer-Verlag, 1998. ISBN 978-3-540-64108-7. URL //www.springer.com/fr/book/9783540641087.

[15] Olivier Fruchart. *Lecture notes on Nanomagnetism*. URL http://archive.org/details/Olivier_Fruchart___Lecture_notes_on_Nanomagnetism. 12

[16] Louis Néel. Anisotropie magnétique superficielle et surstructures d'orientation. *Journal de Physique et le Radium*, 15(4):225–239, 1954. doi: 10.1051/jphysrad:01954001504022500. URL http://dx.doi.org/10.1051/jphysrad:01954001504022500. 14, 24

[17] A V Khvalkovskiy, D Apalkov, S Watts, R Chepulskii, R S Beach, A Ong, X Tang, A Driskill-Smith, W H Butler, P B Visscher, D Lottis, E Chen, V Nikitin, and M Krounbi. Basic principles of stt-mram cell operation in memory arrays. *Journal of Physics D: Applied Physics*, 46(7):074001, 2013. URL http://stacks.iop.org/0022-3727/46/i=7/a=074001. 14, 15, 129

[18] M. T. Johnson, P. J. H. Bloemen, F. J. A. den Broeder, and J. J. de Vries. Magnetic anisotropy in metallic multilayers. *Reports on Progress in Physics*, 59(11):1409, 1996. doi: 10.1088/0034-4885/59/11/002. URL http://stacks.iop.org/0034-4885/59/i=11/a=002. 14, 61, 69

[19] P. Bruno and J. P. Renard. Magnetic surface anisotropy of transition metal ultrathin films. *Applied Physics A Solids and Surfaces*, 49(5):499–506, 1989. doi: 10.1007/BF00617016. URL http://link.springer.com/10.1007/BF00617016. 14, 36, 69, 130

[20] Ie Dzialoshinskii. Thermodynamic theory of weak ferromagnetism in antiferromagnetic substances. *Soviet Physics Jetp-Ussr*, 5(6):1259–1272, 1957. ISSN 0038-5646. WOS:A1957WN04300035. 17

[21] Tôru Moriya. Anisotropic superexchange interaction and weak ferromagnetism. *Physical Review*, 120(1):91–98, 1960. doi: 10.1103/PhysRev.120.91. URL https://link.aps.org/doi/10.1103/PhysRev.120.91. 17

[22] Stefan Heinze, Kirsten von Bergmann, Matthias Menzel, Jens Brede, André Kubetzka, Roland Wiesendanger, Gustav Bihlmayer, and Stefan Blügel. Spontaneous atomic-scale magnetic skyrmion lattice in two dimensions. *Nature Physics*, 7(9):713–718, 2011. doi: 10.1038/nphys2045. URL https://www.nature.com/articles/nphys2045. 17, 26, 27

[23] M. Bode, M. Heide, K. von Bergmann, P. Ferriani, S. Heinze, G. Bihlmayer, A. Kubetzka, O. Pietzsch, S. Blügel, and R. Wiesendanger. Chiral magnetic order at surfaces driven by inversion asymmetry. *Nature*, 447(7141):190–193, 2007. doi: 10.1038/nature05802. URL https://www.nature.com/articles/nature05802. 17, 26

[24] A. Fert and Peter M. Levy. Role of anisotropic exchange interactions in determining the properties of spin-glasses. *Physical Review Letters*, 44(23):1538–1541, 1980. doi: 10.1103/PhysRevLett.44.1538. URL https://link.aps.org/doi/10.1103/PhysRevLett.44.1538. 17, 26, 43

[25] A. R. Fert. Magnetic and transport properties of metallic multilayers, 1990. URL https://www.scientific.net/MSF.59-60.439. 17

[26] A. Crépieux and C. Lacroix. Dzyaloshinskyâmoriya interactions induced by symmetry breaking at a surface. *Journal of Magnetism and Magnetic Materials*, 182(3):341–349, 1998. doi: 10.1016/S0304-8853(97)01044-5. URL http://www.sciencedirect.com/science/article/pii/S0304885397010445. 17

[27] Kyoung-Whan Kim, Hyun-Woo Lee, Kyung-Jin Lee, and M. D. Stiles. Chirality from interfacial spin-orbit coupling effects in magnetic bilayers. *Physical Review Letters*, 111 (21), 2013. doi: 10.1103/PhysRevLett.111.216601. URL https://link.aps.org/doi/10.1103/PhysRevLett.111.216601. 17, 19, 26, 43, 102

[28] K. V. Shanavas, Z. S. Popovi, and S. Satpathy. Theoretical model for rashba spin-orbit interaction in d electrons. *Physical Review B*, 90(16), 2014-. doi: 10.1103/PhysRevB.90.165108. URL https://link.aps.org/doi/10.1103/PhysRevB.90.165108. 17, 19

[29] André Thiaville, Stanislas Rohart, Émilie Jué, Vincent Cros, and Albert Fert. Dynamics of dzyaloshinskii domain walls in ultrathin magnetic films. *EPL (Europhysics Letters)*, 100(5):57002, 2012. doi: 10.1209/0295-5075/100/57002. URL http://stacks.iop.org/0295-5075/100/i=5/a=57002?key=crossref.2efecb4b4825b9f99211cd2da9f0957b. 17, 26, 119

[30] J. Sampaio, V. Cros, S. Rohart, A. Thiaville, and A. Fert. Nucleation, stability and current-induced motion of isolated magnetic skyrmions in nanostructures. *Nature Nanotechnology*, 8(11):839–844, 2013. doi: 10.1038/nnano.2013.210. URL https://www.nature.com/articles/nnano.2013.210. 32

[31] Marcus Heide, Gustav Bihlmayer, and Stefan Blügel. Non-planar dzyaloshinskii spirals and magnetic domain walls in non-centrosymmetric systems with orthorhombic anisotropy. *Journal of Nanoscience and Nanotechnology*, 11(4):3005–3015, 2011. 17

[32] A N Bogdanov and D A Yablonskii. Thermodynamicallystable "vortices" in magnetically-ordered crystals.the mixed state of magnets. page 3. 18

[33] A. Bogdanov and A. Hubert. Thermodynamically stable magnetic vortex states in magnetic crystals. *Journal of Magnetism and Magnetic Materials*, 138(3):255–269, 1994. doi: 10.1016/0304-8853(94)90046-9. URL http://www.sciencedirect.com/science/article/pii/0304885394900469.

[34] S. Rohart and A. Thiaville. Skyrmion confinement in ultrathin film nanostructures in the presence of dzyaloshinskii-moriya interaction. *Physical Review B*, 88(18), 2013. doi: 10.1103/PhysRevB.88.184422. URL https://link.aps.org/doi/10.1103/PhysRevB.88.184422. 18, 24

[35] Marco Perini, Sebastian Meyer, Bertrand Dupé, Stephan von Malottki, André Kubetzka, Kirsten von Bergmann, Roland Wiesendanger, and Stefan Heinze. Domain walls and dzyaloshinskii-moriya interaction in epitaxial co/ir(111) and pt/co/ir(111). *Physical Review B*, 97:184425, 05 2018. doi: 10.1103/PhysRevB.97.184425. 18

[36] Bertrand Dupé, Markus Hoffmann, Charles Paillard, and Stefan Heinze. Tailoring magnetic skyrmions in ultra-thin transition metal films. *Nature Communications*, 5:4030, 2014. doi: 10.1038/ncomms5030. URL https://www.nature.com/articles/ncomms5030. 18, 42

[37] Hongxin Yang, André Thiaville, Stanislas Rohart, Albert Fert, and Mairbek Chshiev. Anatomy of dzyaloshinskii-moriya interaction at Co/Pt interfaces. *Physical Review Letters*, 115(26):267210, 2015. doi: 10.1103/PhysRevLett.115.267210. URL https://link.aps.org/doi/10.1103/PhysRevLett.115.267210. 42

[38] C. Moreau-Luchaire, C. Moutaïs, N. Reyren, J. Sampaio, C. a. F. Vaz, N. Van Horne, K. Bouzehouane, K. Garcia, C. Deranlot, P. Warnicke, P. Wohlhüter, J.-M. George, M. Weigand, J. Raabe, V. Cros, and A. Fert. Additive interfacial chiral interaction in multilayers for stabilization of small individual skyrmions at room temperature. *Nature Nanotechnology*, 11(5):444–448, 2016. doi: 10.1038/nnano.2015.313. URL http://www.nature.com/nnano/journal/v11/n5/full/nnano.2015.313.html. 18, 28, 43

[39] A. Hrabec, N. A. Porter, A. Wells, M.J. Benitez, G. Burnell, S. McVitie, D. McGrouther, T. A. Moore, and C. H. Marrows. Measuring and tailoring the dzyaloshinskii-moriya interaction in perpendicularly magnetized thin ïlms. *Physical Review B*, 90:020402, 07 2014. 18

[40] Yu. A. Bychkov and E. I. Rashba. Properties of a 2d electron gas with lifted spectral degeneracy. *Soviet Journal of Experimental and Theoretical Physics Letters*, 39:78, 1984. URL http://adsabs.harvard.edu/abs/1984JETPL..39...78B. 19

[41] Yu. A. Bychkov and E. I. Rashba. Oscillatory effects and the magnetic susceptibility of carriers in inversion layers. *Journal of Physics C: Solid State Physics*, 17(33):6039, 1984.

doi: 10.1088/0022-3719/17/33/015. URL http://stacks.iop.org/0022-3719/17/i=33/a=015. 19

[42] A. Manchon, H. C. Koo, J. Nitta, S. M. Frolov, and R. A. Duine. New perspectives for rashba spinâorbit coupling. *Nature Materials*, 14(9):871–882, 2015. doi: 10.1038/nmat4360. URL http://www.nature.com/articles/nmat4360. 19

[43] Hongxin Yang, Olivier Boulle, Vincent Cros, Albert Fert, and Mairbek Chshiev. Controlling dzyaloshinskii-moriya interaction via chirality dependent layer stacking, insulator capping and electric field. *Scientific Reports*, 8(12356). URL https://www.nature.com/articles/s41598-018-30063-y. 19, 44, 109

[44] Pietro Gambardella and Ioan Mihai Miron. Current-induced spin-orbit torques. *Philosophical Transactions of the Royal Society of London A: Mathematical, Physical and Engineering Sciences*, 369(1948):3175–3197, 2011. doi: 10.1098/rsta.2010.0336. URL http://rsta.royalsocietypublishing.org/content/369/1948/3175. 20

[45] A. Hoffmann. Spin hall effects in metals. *IEEE Transactions on Magnetics*, 49(10): 5172–5193, 2013. doi: 10.1109/TMAG.2013.2262947. 20

[46] Jairo Sinova, Sergio O. Valenzuela, J. Wunderlich, C. H. Back, and T. Jungwirth. Spin hall effects. *Reviews of Modern Physics*, 87(4):1213–1260, 2015. doi: 10.1103/RevModPhys.87.1213. URL https://link.aps.org/doi/10.1103/RevModPhys.87.1213. 20

[47] V. M. Edelstein. Spin polarization of conduction electrons induced by electric current in two-dimensional asymmetric electron systems. *Solid State Communications*, 73(3):233–235, 1990. doi: 10.1016/0038-1098(90)90963-C. URL http://www.sciencedirect.com/science/article/pii/003810989090963C. 21

[48] A. V. Chaplik, M. V. Entin, and L. I. Magarill. Spin orientation of electrons by lateral electric field in 2d system without inversion symmetry. *Physica E: Low-dimensional Systems and Nanostructures*, 13(2):744–747, 2002. doi: 10.1016/S1386-9477(02)00273-4. URL http://www.sciencedirect.com/science/article/pii/S1386947702002734. 21

[49] F. Bloch. Zur theorie des austauschproblems und der remanenzerscheinung der ferromagnetika. *Zeitschrift für Physik*, 74(5):295–335, 1932. doi: 10.1007/BF01337791. URL https://doi.org/10.1007/BF01337791. 24

[50] L Landau and E Lifshits. ON THE THEORY OF THE DISPERSION OF MAGNETIC PERMEABILITY IN FERROMAGNETIC BODIES. 53:9. 24

[51] Soon-Wook Jung, Woojin Kim, Taek-Dong Lee, Kyung-Jin Lee, and Hyun-Woo Lee. Current-induced domain wall motion in a nanowire with perpendicular magnetic anisotropy. *Applied Physics Letters*, 92(20):202508, 2008. doi: 10.1063/1.2926664. URL https://aip.scitation.org/doi/10.1063/1.2926664. 25

[52] S. V. Tarasenko, A. Stankiewicz, V. V. Tarasenko, and J. Ferré. Bloch wall dynamics in ultrathin ferromagnetic films. *Journal of Magnetism and Magnetic Materials*, 189:19–24, 1998. doi: 10.1016/S0304-8853(98)00230-3. URL http://adsabs.harvard.edu/abs/1998JMMM..189...19T. 25

[53] M. Heide, G. Bihlmayer, and S. Blügel. Dzyaloshinskii-moriya interaction accounting for the orientation of magnetic domains in ultrathin films: Fe/w(110). *Physical Review B*, 78(14):140403, 2008. doi: 10.1103/PhysRevB.78.140403. URL https://link.aps.org/doi/10.1103/PhysRevB.78.140403. 26

[54] T.H.R. Skyrme. A unified field theory of mesons and baryons. *Nuclear Physics*, 31: 556–569, 1962. doi: 10.1016/0029-5582(62)90775-7. URL http://linkinghub.elsevier.com/retrieve/pii/0029558262907757. 26

[55] A. Bocdanov and A. Hubert. The properties of isolated magnetic vortices. *physica status solidi (b)*, 186(2):527–543, 1994. doi: 10.1002/pssb.2221860223. URL http://onlinelibrary.wiley.com/doi/10.1002/pssb.2221860223/abstract. 26

[56] B. A. Ivanov, V. A. Stephanovich, and A. A. Zhmudskii. Magnetic vortices îÿ the microscopic analogs of magnetic bubbles. *Journal of Magnetism and Magnetic Materials*, 88(1):116–120, 1990. doi: 10.1016/S0304-8853(97)90021-4. URL http://www.sciencedirect.com/science/article/pii/S0304885397900214. 26

[57] Naoto Nagaosa and Yoshinori Tokura. Topological properties and dynamics of magnetic skyrmions. *Nature Nanotechnology*, 8(12):899–911, 2013. doi: 10.1038/nnano.2013.243. URL https://www.nature.com/articles/nnano.2013.243. 26

[58] Hans-Benjamin Braun. Topological effects in nanomagnetism: from superparamagnetism to chiral quantum solitons. *Advances in Physics*, 61(1):1–116, 2012. doi: 10.1080/00018732.2012.663070. URL http://www.tandfonline.com/doi/abs/10.1080/00018732.2012.663070. 26

[59] S. Muhlbauer, B. Binz, F. Jonietz, C. Pfleiderer, A. Rosch, A. Neubauer, R. Georgii, and P. Boni. Skyrmion lattice in a chiral magnet. *Science*, 323(5916):915–919, 2009. doi: 10.1126/science.1166767. URL http://www.sciencemag.org/cgi/doi/10.1126/science.1166767. 27, 87, 97

[60] X. Z. Yu, Y. Onose, N. Kanazawa, J. H. Park, J. H. Han, Y. Matsui, N. Nagaosa, and Y. Tokura. Real-space observation of a two-dimensional skyrmion crystal. *Nature*, 465 (7300):901–904, 2010. doi: 10.1038/nature09124. URL https://www.nature.com/articles/nature09124. 27, 87, 97

[61] X. Z. Yu, N. Kanazawa, Y. Onose, K. Kimoto, W. Z. Zhang, S. Ishiwata, Y. Matsui, and Y. Tokura. Near room-temperature formation of a skyrmion crystal in thin-films of the helimagnet FeGe. *Nature Materials*, 10(2):106–109, 2011. doi: 10.1038/nmat2916. URL https://www.nature.com/articles/nmat2916. 27

[62] Niklas Romming, Christian Hanneken, Matthias Menzel, Jessica E. Bickel, Boris Wolter, Kirsten von Bergmann, André Kubetzka, and Roland Wiesendanger. Writing and deleting single magnetic skyrmions. *Science*, 341(6146):636–639, 2013. doi: 10.1126/science.1240573. URL http://science.sciencemag.org/content/341/6146/636. 27

[63] W. Jiang, P. Upadhyaya, W. Zhang, G. Yu, M. B. Jungfleisch, F. Y. Fradin, J. E. Pearson, Y. Tserkovnyak, K. L. Wang, O. Heinonen, S. G. E. te Velthuis, and A. Hoffmann. Blowing magnetic skyrmion bubbles. *Science*, 349(6245):283–286, 2015. doi: 10.1126/science.aaa1442. URL http://www.sciencemag.org/cgi/doi/10.1126/science.aaa1442. 28, 30, 79, 87, 88, 92, 93

[64] Seonghoon Woo, Kai Litzius, Benjamin Krüger, Mi-Young Im, Lucas Caretta, Kornel Richter, Maxwell Mann, Andrea Krone, Robert M. Reeve, Markus Weigand, Parnika Agrawal, Ivan Lemesh, Mohamad-Assaad Mawass, Peter Fischer, Mathias KlÃui, and Geoffrey S. D. Beach. Observation of room-temperature magnetic skyrmions and their current-driven dynamics in ultrathin metallic ferromagnets. *Nature Materials*, 15(5):501–506, 2016. doi: 10.1038/nmat4593. URL https://www.nature.com/articles/nmat4593. 28, 30, 87, 88, 105

[65] Olivier Boulle, Jan Vogel, Hongxin Yang, Stefania Pizzini, Dayane de Souza Chaves, Andrea Locatelli, Tevfik Onur MenteÅ§, Alessandro Sala, Liliana D. Buda-Prejbeanu, Olivier Klein, Mohamed Belmeguenai, Yves Roussigné, Andrey Stashkevich, Salim Mourad Chérif, Lucia Aballe, Michael Foerster, Mairbek Chshiev, Stéphane Auffret, Ioan Mihai Miron, and Gilles Gaudin. Room-temperature chiral magnetic skyrmions in ultrathin magnetic nanostructures. *Nature Nanotechnology*, 11(5):449–454, 2016. doi: 10.1038/nnano.2015.315. URL http://www.nature.com/articles/nnano.2015.315. 28, 43, 85, 87

[66] Guoqiang Yu, Pramey Upadhyaya, Xiang Li, Wenyuan Li, Se Kwon Kim, Yabin Fan, Kin L. Wong, Yaroslav Tserkovnyak, Pedram Khalili Amiri, and Kang L. Wang. Room-temperature creation and spinâorbit torque manipulation of skyrmions in thin films with engineered asymmetry. *Nano Letters*, 16(3):1981–1988, 2016. doi: 10.1021/acs.nanolett.5b05257. URL https://doi.org/10.1021/acs.nanolett.5b05257. 28, 88, 102

[67] Anne Bernand-Mantel, Lorenzo Camosi, Alexis Wartelle, Nicolas Rougemaille, MichaÃl Darques, and Laurent Ranno. The skyrmion-bubble transition in a ferromagnetic thin film. *SciPost Physics*, 4(5):027, 2018. doi: 10.21468/SciPostPhys.4.5.027. URL https://scipost.org/10.21468/SciPostPhys.4.5.027. 28

[68] Felix Büttner, Ivan Lemesh, and Geoffrey S. D. Beach. Theory of isolated magnetic skyrmions: From fundamentals to room temperature applications. *Scientific Reports*, 8(1):4464, 2018. doi: 10.1038/s41598-018-22242-8. URL https://www.nature.com/articles/s41598-018-22242-8. 28

[69] Marine Schott, Anne Bernand-Mantel, Laurent Ranno, Stefania Pizzini, Jan Vogel, Hélène Béa, Claire Baraduc, Stéphane Auffret, Gilles Gaudin, and Dominique Givord. The skyrmion switch: Turning magnetic skyrmion bubbles on and off with an electric field. *Nano Letters*, 17(5):3006–3012, 2017. doi: 10.1021/acs.nanolett.7b00328. URL http://pubs.acs.org/doi/10.1021/acs.nanolett.7b00328. 28, 40, 41, 89, 94, 95, 97, 104, 115, 116, 117, 131

[70] Titiksha Srivastava, Marine Schott, Roméo Juge, Viola Krizakova, Mohamed Belmeguenai, Yves Roussigné, Anne Bernand-Mantel, Laurent Ranno, Stefania Pizzini, Salim-Mourad Chérif, Andrey Stashkevich, Stéphane Auffret, Olivier Boulle, Gilles Gaudin, Mairbek Chshiev, Claire Baraduc, and Hélène Béa. Large-voltage tuning of dzyaloshinskiiâmoriya interactions: A route toward dynamic control of skyrmion chirality. *Nano Letters*, 18(8): 4871–4877, 2018. doi: 10.1021/acs.nanolett.8b01502. URL https://doi.org/10.1021/acs.nanolett.8b01502. 28

[71] Pin-Jui Hsu, André Kubetzka, Aurore Finco, Niklas Romming, Kirsten von Bergmann, and Roland Wiesendanger. Electric-field-driven switching of individual magnetic skyrmions. *Nature Nanotechnology*, 12(2):123–126, 2017. doi: 10.1038/nnano.2016.234. URL https://www.nature.com/articles/nnano.2016.234. 28, 39, 41, 97, 131

[72] R. Tolley, S. A. Montoya, and E. E. Fullerton. Room-temperature observation and current control of skyrmions in pt/co/os/pt thin films. *Physical Review Materials*, 2(4):044404, 2018. doi: 10.1103/PhysRevMaterials.2.044404. URL https://link.aps.org/doi/10.1103/PhysRevMaterials.2.044404. 28

[73] William Legrand, Davide Maccariello, Nicolas Reyren, Karin Garcia, Christoforos Moutafis, Constance Moreau-Luchaire, Sophie Collin, Karim Bouzehouane, Vincent Cros, and Albert Fert. Room-temperature current-induced generation and motion of sub-100 nm skyrmions. *Nano Letters*, 17(4):2703–2712, 2017. doi: 10.1021/acs.nanolett.7b00649. URL http://dx.doi.org/10.1021/acs.nanolett.7b00649. 28

[74] Anjan Soumyanarayanan, M. Raju, A. L. Gonzalez Oyarce, Anthony K. C. Tan, Mi-Young Im, A. P. Petrovi, Pin Ho, K. H. Khoo, M. Tran, C. K. Gan, F. Ernult, and C. Panagopoulos. Tunable room-temperature magnetic skyrmions in ir/fe/co/pt multilayers. *Nature Materials*, 16(9):898–904, 2017. doi: 10.1038/nmat4934. URL https://www.nature.com/articles/nmat4934. 28

[75] Roméo Juge, Soong-Geun Je, Dayane de Souza Chaves, Stefania Pizzini, Liliana D. Buda-Prejbeanu, Lucia Aballe, Michael Foerster, Andrea Locatelli, Tevfik Onur Mentes, Alessandro Sala, Francesco Maccherozzi, Sarnjeet S. Dhesi, Stéphane Auffret, Eric Gautier, Gilles Gaudin, Jan Vogel, and Olivier Boulle. Magnetic skyrmions in confined geometries: Effect of the magnetic field and the disorder. *Journal of Magnetism and Magnetic Materials*, 455:3–8, 2018. doi: 10.1016/j.jmmm.2017.10.030. URL http://www.sciencedirect.com/science/article/pii/S0304885317317110. 28

[76] Christian Hanneken, Fabian Otte, André Kubetzka, Bertrand Dupé, Niklas Romming, Kirsten von Bergmann, Roland Wiesendanger, and Stefan Heinze. Electrical detection of

magnetic skyrmions by tunnelling non-collinear magnetoresistance. *Nature Nanotechnology*, 10(12):1039–1042, 2015. doi: 10.1038/nnano.2015.218. 29

[77] Davide Maccariello, William Legrand, Nicolas Reyren, Karin Garcia, Karim Bouzehouane, Sophie Collin, Vincent Cros, and Albert Fert. Electrical detection of single magnetic skyrmions in metallic multilayers at room temperature. *Nature Nanotechnology*, 13 (3):233–237, 2018. doi: 10.1038/s41565-017-0044-4. URL https://www.nature.com/articles/s41565-017-0044-4. 29

[78] A. A. Thiele. Steady-state motion of magnetic domains. *Physical Review Letters*, 30(6): 230–233, 1973. doi: 10.1103/PhysRevLett.30.230. URL http://link.aps.org/doi/10.1103/PhysRevLett.30.230. 29

[79] Wanjun Jiang, Xichao Zhang, Guoqiang Yu, Wei Zhang, Xiao Wang, M. Benjamin Jungfleisch, John E. Pearson, Xuemei Cheng, Olle Heinonen, Kang L. Wang, Yan Zhou, Axel Hoffmann, and Suzanne G. E. te Velthuis. Direct observation of the skyrmion hall effect. *Nature Physics*, 13(2):162–169, 2017. doi: 10.1038/nphys3883. URL http://www.nature.com/articles/nphys3883. 29, 30

[80] Satoru Emori, Uwe Bauer, Sung-Min Ahn, Eduardo Martinez, and Geoffrey S. D. Beach. Current-driven dynamics of chiral ferromagnetic domain walls. *Nature Materials*, 12 (7):611–616, 2013. doi: 10.1038/nmat3675. URL https://www.nature.com/articles/nmat3675. 30

[81] Minh-Hai Nguyen, D. C. Ralph, and R. A. Buhrman. Spin torque study of the spin hall conductivity and spin diffusion length in platinum thin films with varying resistivity. *Physical Review Letters*, 116(12):126601, 2016. doi: 10.1103/PhysRevLett.116.126601. URL https://link.aps.org/doi/10.1103/PhysRevLett.116.126601. 30

[82] A. Hrabec, J. Sampaio, M. Belmeguenai, I. Gross, R. Weil, S. M. Chérif, A. Stashkevich, V. Jacques, A. Thiaville, and S. Rohart. Current-induced skyrmion generation and dynamics in symmetric bilayers. *Nature Communications*, 8:ncomms15765, 2017. doi: 10.1038/ncomms15765. URL https://www.nature.com/articles/ncomms15765. 30

[83] Seonghoon Woo, Kyung Mee Song, Xichao Zhang, Yan Zhou, Motohiko Ezawa, Xiaoxi Liu, S. Finizio, J. Raabe, Nyun Jong Lee, Sang-Il Kim, Seung-Young Park, Younghak Kim, Jae-Young Kim, Dongjoon Lee, OukJae Lee, Jun Woo Choi, Byoung-Chul Min, Hyun Cheol Koo, and Joonyeon Chang. Current-driven dynamics and inhibition of the skyrmion hall effect of ferrimagnetic skyrmions in GdFeCo films. *Nature Communications*, 9(1):959, 2018. doi: 10.1038/s41467-018-03378-7. URL https://www.nature.com/articles/s41467-018-03378-7. 30

[84] Se Kwon Kim, Kyung-Jin Lee, and Yaroslav Tserkovnyak. Self-focusing skyrmion racetracks in ferrimagnets. *Physical Review B*, 95(14):140404, 2017. doi: 10.1103/PhysRevB.95.140404. URL https://link.aps.org/doi/10.1103/PhysRevB.95.140404.

[85] Lucas Caretta, Maxwell Mann, Felix Büttner, Kohei Ueda, Bastian Pfau, Christian M. Günther, Piet Hessing, Alexandra Churikova, Christopher Klose, Michael Schneider, Dieter Engel, Colin Marcus, David Bono, Kai Bagschik, Stefan Eisebitt, and Geoffrey S. D. Beach. Fast current-driven domain walls and small skyrmions in a compensated ferrimagnet. *Nature Nanotechnology*, 13:1154–1160, 2018. doi: 10.1038/s41565-018-0255-3. URL https://www.nature.com/articles/s41565-018-0255-3. 30

[86] Ajaya K. Nayak, Vivek Kumar, Tianping Ma, Peter Werner, Eckhard Pippel, Roshnee Sahoo, Franoise Damay, Ulrich K. RöBler, Claudia Felser, and Stuart S. P. Parkin. Magnetic antiskyrmions above room temperature in tetragonal heusler materials. *Nature*, 548 (7669):561–566, 2017. doi: 10.1038/nature23466. URL https://www.nature.com/articles/nature23466. 31

[87] Lorenzo Camosi, Nicolas Rougemaille, Olivier Fruchart, Jan Vogel, and Stanislas Rohart. Micromagnetics of antiskyrmions in ultrathin films. *Physical Review B*, 97(13):134404, 2018. doi: 10.1103/PhysRevB.97.134404. URL https://link.aps.org/doi/10.1103/PhysRevB.97.134404. 31

[88] Xichao Zhang, Jing Xia, Yan Zhou, Daowei Wang, Xiaoxi Liu, Weisheng Zhao, and Motohiko Ezawa. Control and manipulation of a magnetic skyrmionium in nanostructures. *Physical Review B*, 94(9):094420, 2016. doi: 10.1103/PhysRevB.94.094420. URL https://link.aps.org/doi/10.1103/PhysRevB.94.094420. 31, 32, 130

[89] Shilei Zhang, Florian Kronast, Gerrit van der Laan, and Thorsten Hesjedal. Real-space observation of skyrmionium in a ferromagnet-magnetic topological insulator heterostructure. *Nano Letters*, 18(2):1057–1063, 2018. doi: 10.1021/acs.nanolett.7b04537. URL https://doi.org/10.1021/acs.nanolett.7b04537. 31

[90] Alexander G. Kolesnikov, Maksim E. Stebliy, Alexander S. Samardak, and Alexey V. Ognev. Skyrmionium â high velocity without the skyrmion hall effect. *Scientific Reports*, 8(1): 16966, 2018. doi: 10.1038/s41598-018-34934-2. URL https://www.nature.com/articles/s41598-018-34934-2. 31

[91] Maokang Shen, Yue Zhang, Jun Ou-Yang, Xiaofei Yang, and Long You. Motion of a skyrmionium driven by spin wave. *Applied Physics Letters*, 112(6):062403, 2018. doi: 10.1063/1.5010605. URL https://aip.scitation.org/doi/10.1063/1.5010605. 31

[92] Stuart Parkin and See-Hun Yang. Memory on the racetrack. *Nature Nanotechnology*, 10:195–198, 2015. doi: 10.1038/nnano.2015.41. URL https://www.nature.com/articles/nnano.2015.41. 32

[93] Wang Kang, Yangqi Huang, Chentian Zheng, Weifeng Lv, Na Lei, Youguang Zhang, Xichao Zhang, Yan Zhou, and Weisheng Zhao. Voltage controlled magnetic skyrmion motion for racetrack memory. *Scientific Reports*, 6:23164, 2016. doi: 10.1038/srep23164. URL https://www.nature.com/articles/srep23164. 32

[94] Xichao Zhang, Yan Zhou, and Motohiko Ezawa. Magnetic bilayer-skyrmions without skyrmion hall effect. *Nature Communications*, 7:10293, 2016. doi: 10.1038/ncomms10293. URL https://www.nature.com/articles/ncomms10293. 32

[95] Xichao Zhang, Motohiko Ezawa, and Yan Zhou. Magnetic skyrmion logic gates: conversion, duplication and merging of skyrmions. *Scientific Reports*, 5:9400, 2015. doi: 10.1038/srep09400. URL https://www.nature.com/articles/srep09400. 33

[96] G. Finocchio, M. Ricci, R. Tomasello, A. Giordano, M. Lanuzza, V. Puliafito, P. Burrascano, B. Azzerboni, and M. Carpentieri. Skyrmion based microwave detectors and harvesting. *Applied Physics Letters*, 107(26):262401, 2015. doi: 10.1063/1.4938539. URL https://aip.scitation.org/doi/10.1063/1.4938539. 33

[97] Mario Carpentieri, Riccardo Tomasello, Roberto Zivieri, and Giovanni Finocchio. Topological, non-topological and instanton droplets driven by spin-transfer torque in materials with perpendicular magnetic anisotropy and dzyaloshinskiiâmoriya interaction. *Scientific Reports*, 5:16184, 2015. doi: 10.1038/srep16184. URL https://www.nature.com/articles/srep16184. 33

[98] F. Garcia-Sanchez, J. Sampaio, N. Reyren, V. Cros, and J.-V. Kim. A skyrmion-based spin-torque nano-oscillator. *New Journal of Physics*, 18(7):075011, 2016. doi: 10.1088/1367-2630/18/7/075011. URL http://stacks.iop.org/1367-2630/18/i=7/a=075011. 33

[99] Yangqi Huang, Wang Kang, Xichao Zhang, Yan Zhou, and Weisheng Zhao. Magnetic skyrmion-based synaptic devices. *Nanotechnology*, 28(8):08LT02, 2017. doi: 10.1088/1361-6528/aa5838. URL http://stacks.iop.org/0957-4484/28/i=8/a=08LT02. 33

[100] D. Pinna, F. Abreu Araujo, J.-V. Kim, V. Cros, D. Querlioz, P. Bessiere, J. Droulez, and J. Grollier. Skyrmion gas manipulation for probabilistic computing. *Physical Review Applied*, 9(6):064018, 2018-06-13. doi: 10.1103/PhysRevApplied.9.064018. URL https://link.aps.org/doi/10.1103/PhysRevApplied.9.064018. 33

[101] P. Winiowski, J. M. Almeida, S. Cardoso, N. P. Barradas, and P. P. Freitas. Effect of free layer thickness and shape anisotropy on the transfer curves of MgO magnetic tunnel junctions. *Journal of Applied Physics*, 103(7):07A910, 2008. doi: 10.1063/1.2838626. URL http://aip.scitation.org/doi/10.1063/1.2838626. 36

[102] T. Takenaga, C. Yoshida, Y. Yamazaki, A. Hatada, M. Nakabayashi, Y. Iba, A. Takahashi, H. Noshiro, K. Tsunoda, M. Aoki, T. Furukawa, H. Ohji, and T. Sugii. MgO based magnetic tunnel junctions with $Co_{20}Fe_{60}B_{20}$sensing layer for magnetic field sensors. *IEEE Transactions on Magnetics*, 49(7):3878–3881, 2013. doi: 10.1109/TMAG.2013.2240275. 36

[103] S. Miwa Y. Shiota K. Yakushiji H. Kubota T. Nozaki A. Fukushima S. Yuasa D. D Lam, F. Bonell and Y. Suzuki. Composition dependence of perpendicular magnetic anisotropy

in ta/coxfe80 xb20/mgo/ta multilayers. *Journal of Magnetics,*, 18:5–8, 2013. 36, 37, 130

[104] S. Monso, B. Rodmacq, S. Auffret, G. Casali, F. Fettar, B. Gilles, B. Dieny, and P. Boyer. Crossover from in-plane to perpendicular anisotropy in pt/CoFe/AlOx sandwiches as a function of al oxidation: A very accurate control of the oxidation of tunnel barriers. *Applied Physics Letters*, 80(22):4157–4159, 2002. doi: 10.1063/1.1483122. URL http://scitation.aip.org/content/aip/journal/apl/80/22/10.1063/1.1483122. 36

[105] Juan G. Alzate, Pedram Khalili Amiri, Guoqiang Yu, Pramey Upadhyaya, Jordan A. Katine, Juergen Langer, Berthold Ocker, Ilya N. Krivorotov, and Kang L. Wang. Temperature dependence of the voltage-controlled perpendicular anisotropy in nanoscale MgO / CoFeB / Ta magnetic tunnel junctions. *Applied Physics Letters*, 104(11), 2014. doi: http://dx.doi.org/10.1063/1.4869152. URL http://scitation.aip.org/content/aip/journal/apl/104/11/10.1063/1.4869152. 37, 130

[106] Evgeny Y. Tsymbal. Spintronics: Electric toggling of magnets. *Nature Materials*, 11(1):12–13, 2012. doi: 10.1038/nmat3205. URL https://www.nature.com/articles/nmat3205. 38, 97, 100

[107] Fumihiro Matsukura, Yoshinori Tokura, and Hideo Ohno. Control of magnetism by electric fields. *Nature Nanotechnology*, 10(3):209–220, 2015. doi: 10.1038/nnano.2015.22. URL https://www.nature.com/articles/nnano.2015.22. 38, 97, 107

[108] Martin Weisheit, Sebastian FÃhler, Alain Marty, Yves Souche, Christiane Poinsignon, and Dominique Givord. Electric field-induced modification of magnetism in thin-film ferromagnets. *Science*, 315(5810):349–351, 2007. doi: 10.1126/science.1136629. URL http://science.sciencemag.org/content/315/5810/349. 38

[109] Uwe Bauer, Lide Yao, Aik Jun Tan, Parnika Agrawal, Satoru Emori, Harry L. Tuller, Sebastiaan van Dijken, and Geoffrey S. D. Beach. Magneto-ionic control of interfacial magnetism. *Nature Materials*, 14(2):174–181, 2015. doi: 10.1038/nmat4134. URL https://www.nature.com/articles/nmat4134. 38, 100, 110

[110] Yoichi Shiota, Takuto Maruyama, Takayuki Nozaki, Teruya Shinjo, Masashi Shiraishi, and Yoshishige Suzuki. Voltage-assisted magnetization switching in ultrathin fe80co20 alloy layers. *Applied Physics Express*, 2(6):063001, 2009. doi: 10.1143/APEX.2.063001. URL http://iopscience.iop.org/article/10.1143/APEX.2.063001/meta. 39, 40, 131

[111] T. Nozaki, Y. Shiota, M. Shiraishi, T. Shinjo, and Y. Suzuki. Voltage-induced perpendicular magnetic anisotropy change in magnetic tunnel junctions. *Applied Physics Letters*, 96(2):022506, 2010. doi: 10.1063/1.3279157. URL https://aip.scitation.org/doi/full/10.1063/1.3279157. 39

[112] M. Endo, S. Kanai, S. Ikeda, F. Matsukura, and H. Ohno. Electric-field effects on thickness dependent magnetic anisotropy of sputtered MgO/co40fe40b20/ta structures.

Applied Physics Letters, 96(21):212503, 2010. doi: 10.1063/1.3429592. URL https://aip.scitation.org/doi/full/10.1063/1.3429592. 39, 40, 131

[113] Jacob Torrejon, Junyeon Kim, Jaivardhan Sinha, Seiji Mitani, Masamitsu Hayashi, Michihiko Yamanouchi, and Hideo Ohno. Interface control of the magnetic chirality in CoFeB/MgO heterostructures with heavy-metal underlayers. *Nature Communications*, 5:4655, 2014. doi: 10.1038/ncomms5655. URL https://www.nature.com/articles/ncomms5655. 41, 102

[114] Xin Ma, Guoqiang Yu, Xiang Li, Tao Wang, Di Wu, Kevin S. Olsson, Zhaodong Chu, Kyongmo An, John Q. Xiao, Kang L. Wang, and Xiaoqin Li. Interfacial control of dzyaloshinskii-moriya interaction in heavy metal/ferromagnetic metal thin film heterostructures. *Physical Review B*, 94(18), 2016. doi: 10.1103/PhysRevB.94.180408. URL https://link.aps.org/doi/10.1103/PhysRevB.94.180408. 42, 58, 99, 131

[115] A. L. Balk, K-W. Kim, D. T. Pierce, M. D. Stiles, J. Unguris, and S. M. Stavis. Simultaneous control of the dzyaloshinskii-moriya interaction and magnetic anisotropy in nanomagnetic trilayers. *Physical Review Letters*, 119(7):077205, 2017. doi: 10.1103/PhysRevLett.119.077205. URL https://link.aps.org/doi/10.1103/PhysRevLett.119.077205. 43, 115, 131

[116] Abderrezak Belabbes, Gustav Bihlmayer, Stefan Blügel, and Aurélien Manchon. Oxygen-enabled control of dzyaloshinskii-moriya interaction in ultra-thin magnetic films. *Scientific Reports*, 6:24634, 2016. doi: 10.1038/srep24634. URL https://www.nature.com/articles/srep24634. 43, 88, 115

[117] Kohei Nawaoka, Shinji Miwa, Yoichi Shiota, Norikazu Mizuochi, and Yoshishige Suzuki. Voltage induction of interfacial dzyaloshinskiiâmoriya interaction in au/fe/MgO artificial multilayer. *Applied Physics Express*, 8(6):063004, 2015. doi: 10.7567/APEX.8.063004. URL http://stacks.iop.org/1882-0786/8/i=6/a=063004?key=crossref.d57e9ddd3b6d845c141bf8c60176d6d9. 44, 101, 109

[118] M. R. Parker. The kerr magneto-optic effect (1876â1976). *Physica B+C*, 86-88:1171–1176, 1977. doi: 10.1016/0378-4363(77)90836-1. URL http://www.sciencedirect.com/science/article/pii/0378436377908361. 53

[119] Hans T. Nembach, Justin M. Shaw, Mathias Weiler, Emilie Jué, and Thomas J. Silva. Linear relation between heisenberg exchange and interfacial dzyaloshinskiiâmoriya interaction in metal films. *Nature Physics*, 11(10):825–829, 2015. doi: 10.1038/nphys3418. URL https://www.nature.com/articles/nphys3418. 58, 59, 99, 133

[120] M. Belmeguenai, M. S. Gabor, Y. Roussigné, A. Stashkevich, S. M. Chérif, F. Zighem, and C. Tiusan. Brillouin light scattering investigation of the thickness dependence of dzyaloshinskii-moriya interaction in c o 0.5 f e 0.5 ultrathin films. *Physical Review B*, 93(17), 2016. doi: 10.1103/PhysRevB.93.174407. URL https://link.aps.org/doi/10.1103/PhysRevB.93.174407. 58, 99

[121] Mohamed Belmeguenai, Jean-Paul Adam, Yves Roussigné, Sylvain Eimer, Thibaut Devolder, Joo-Von Kim, Salim Mourad Cherif, Andrey Stashkevich, and André Thiaville. Interfacial dzyaloshinskii-moriya interaction in perpendicularly magnetized Pt/Co/AlOx ultrathin films measured by brillouin light spectroscopy. *Physical Review B*, 91(18), 2015. doi: 10.1103/PhysRevB.91.180405. URL https://link.aps.org/doi/10.1103/PhysRevB.91.180405. 58, 99, 102

[122] Kai Di, Vanessa Li Zhang, Hock Siah Lim, Ser Choon Ng, Meng Hau Kuok, Jiawei Yu, Jungbum Yoon, Xuepeng Qiu, and Hyunsoo Yang. Direct observation of the dzyaloshinskii-moriya interaction in a pt/co/ni film. *Physical Review Letters*, 114(4):047201, 2015. doi: 10.1103/PhysRevLett.114.047201. URL https://link.aps.org/doi/10.1103/PhysRevLett.114.047201. 58, 99

[123] T. Zhu, Q. Zhang, and R. Yu. Tuning perpendicular magnetic anisotropy in the MgO/-CoFeB/ta thin films. In *2015 IEEE International Magnetics Conference (INTERMAG)*, pages 1–1, 2015. doi: 10.1109/INTMAG.2015.7157631. 61, 78, 80

[124] A. Manchon, C. Ducruet, L. Lombard, S. Auffret, B. Rodmacq, B. Dieny, S. Pizzini, J. Vogel, V. Uhlír, M. Hochstrasser, and G. Panaccione. Analysis of oxygen induced anisotropy crossover in Pt/Co/MOx trilayers. *Journal of Applied Physics*, 104(4):043914, 2008. doi: 10.1063/1.2969711. URL https://aip.scitation.org/doi/10.1063/1.2969711. 84, 85

[125] B. Rodmacq, S. Auffret, B. Dieny, S. Monso, and P. Boyer. Crossovers from in-plane to perpendicular anisotropy in magnetic tunnel junctions as a function of the barrier degree of oxidation. *Journal of Applied Physics*, 93(10):7513–7515, 2003. doi: 10.1063/1.1555292. URL https://aip.scitation.org/doi/10.1063/1.1555292. 84, 85

[126] M. Heide, G. Bihlmayer, and S. Blügel. Dzyaloshinskii-moriya interaction accounting for the orientation of magnetic domains in ultrathin films: Fe/W(110). *Physical Review B*, 78(14), 2008. doi: 10.1103/PhysRevB.78.140403. URL https://link.aps.org/doi/10.1103/PhysRevB.78.140403. 88, 105

[127] U. K. RöBler, A. N. Bogdanov, and C. Pfleiderer. Spontaneous skyrmion ground states in magnetic metals. *Nature*, 442(7104):797–801, 2006. doi: 10.1038/nature05056. URL https://www.nature.com/articles/nature05056. 97

[128] H Bouloussa, J Yu, Y Roussigné, M Belmeguenai, A Stashkevitch, H Yang, and S M Chérif. Brillouin light scattering investigation of interfacial dzyaloshinski-iâmoriya interaction in ultrathin co/pt nanostripe arrays. *Journal of Physics D: Applied Physics*, 51(22):225005, 2018. doi: 10.1088/1361-6463/aab840. URL http://stacks.iop.org/0022-3727/51/i=22/a=225005?key=crossref.a698e2d098f3f74dd40c8655e38e0575. 98

[129] R. A. Khan, P. M. Shepley, A. Hrabec, A. W. J. Wells, B. Ocker, C. H. Marrows, and T. A. Moore. Effect of annealing on the interfacial dzyaloshinskii-moriya interaction in

Ta/CoFeB/MgO trilayers. *Applied Physics Letters*, 109(13):132404, 2016. doi: 10.1063/1.4963731. URL https://aip.scitation.org/doi/10.1063/1.4963731. 102

[130] I. Gross, L. J. Martínez, J.-P. Tetienne, T. Hingant, J.-F. Roch, K. Garcia, R. Soucaille, J. P. Adam, J.-V. Kim, S. Rohart, A. Thiaville, J. Torrejon, M. Hayashi, and V. Jacques. Direct measurement of interfacial dzyaloshinskii-moriya interaction in x | CoFeB | MgO heterostructures with a scanning NV magnetometer (x = Ta , TaN , and W). *Physical Review B*, 94(6), 2016. doi: 10.1103/PhysRevB.94.064413. URL https://link.aps.org/doi/10.1103/PhysRevB.94.064413. 102

[131] S. Pizzini, J. Vogel, S. Rohart, L.D. Buda-Prejbeanu, E. Jué, O. Boulle, I.M. Miron, C.K. Safeer, S. Auffret, G. Gaudin, and A. Thiaville. Chirality-induced asymmetric magnetic nucleation in Pt/Co/AlO ultrathin microstructures. *Physical Review Letters*, 113(4):047203, 2014. doi: 10.1103/PhysRevLett.113.047203. URL https://link.aps.org/doi/10.1103/PhysRevLett.113.047203. 102

[132] Guoqiang Yu, Pramey Upadhyaya, Qiming Shao, Hao Wu, Gen Yin, Xiang Li, Congli He, Wanjun Jiang, Xiufeng Han, Pedram Khalili Amiri, and Kang L. Wang. Room-temperature skyrmion shift device for memory application. *Nano Letters*, 17(1):261–268, 2017-01-11. ISSN 1530-6984. doi: 10.1021/acs.nanolett.6b04010. URL https://doi.org/10.1021/acs.nanolett.6b04010. 102

[133] B. Kaplan and G. A. Gehring. The domain structure in ultrathin magnetic films. *Journal of Magnetism and Magnetic Materials*, 128(1):111–116, 1993. doi: 10.1016/0304-8853(93)90863-W. URL http://www.sciencedirect.com/science/article/pii/030488539390863W. 104

[134] Stewart E. Barnes, Jun'ichi Ieda, and Sadamichi Maekawa. Rashba spin-orbit anisotropy and the electric field control of magnetism. *Scientific Reports*, 4:4105, 2014. doi: 10.1038/srep04105. URL https://www.nature.com/articles/srep04105. 110

[135] J. F. Conley, Y. Ono, R. Solanki, G. Stecker, and W. Zhuang. Electrical properties of HfO2 deposited via atomic layer deposition using hf(NO3)4 and h2o. *Applied Physics Letters*, 82(20):3508–3510, 2003. doi: 10.1063/1.1575934. URL https://aip.scitation.org/doi/10.1063/1.1575934. 115

[136] S. Amara-Dababi, R. C. Sousa, M. Chshiev, H. Béa, J. Alvarez-Hérault, L. Lombard, I. L. Prejbeanu, K. Mackay, and B. Dieny. Charge trapping-detrapping mechanism of barrier breakdown in MgO magnetic tunnel junctions. *Applied Physics Letters*, 99(8):083501, 2011. doi: 10.1063/1.3615654. URL https://aip.scitation.org/doi/10.1063/1.3615654. 115

[137] Arne Vansteenkiste, Jonathan Leliaert, Mykola Dvornik, Mathias Helsen, Felipe Garcia-Sanchez, and Bartel Van Waeyenberge. The design and verification of MuMax3. *AIP Advances*, 4(10):107133, 2014. doi: 10.1063/1.4899186. URL https://aip.scitation.org/doi/10.1063/1.4899186. 118

[138] Soong-Geun Je, Pierre Vallobra, Titiksha Srivastava, Juan-Carlos Rojas-Sánchez, Thai Ha Pham, Michel Hehn, Gregory Malinowski, Claire Baraduc, Stéphane Auffret, Gilles Gaudin, Stéphane Mangin, Hélène Béa, and Olivier Boulle. Creation of magnetic skyrmion bubble lattices by ultrafast laser in ultrathin films. *Nano Letters*, 18(11):7362–7371, 2018. doi: 10.1021/acs.nanolett.8b03653. URL https://doi.org/10.1021/acs.nanolett.8b03653. 124